UNIVERSITÀ
DEGLI STUDI
FIRENZE

DOTTORATO DI RICERCA IN

INTERNATIONAL DOCTORATE IN ATOMIC AND MOLECULAR PHOTONICS

CICLO **XXXV**

Coordinatore Prof. Wiersma Diederik

Atom Interferometry with Bose-Einstein Condensate in optical Beat Note Superlattices

Settore scientifico disciplinare: **FIS/03**

Dottorando
Tommaso Petrucciani

Tutor
Prof. Marco Fattori

Coordinatore
Prof. Wiersma Diederik

Anni Accademici 2019/2022

Abstract

Optical lattices represent a fundamental tool in the field of ultra-cold atoms that allow to simulate a large variety of quantum phenomena like the conduction of electrons in solids, to explore the physics of quantum particles in low dimensions and to implement spin models to simulate quantum magnetism. In addition optical lattices allow manipulation of ultra-cold atoms in atomic clocks and atom interferometry experiments for the precise measurement of time, gravity, fundamental constants and for fundamental physics tests.
Optical lattices of wavelength λ, created by retro-reflecting a laser beam on a mirror, show useful stability properties, since the lattice period is exactly $\lambda/2$, so the position of the minima of the potential depends only on the frequency. With current technologies it is possible to stabilize frequencies below the Hz level. Moreover, this configuration is strongly immune to beam pointing instabilities, vibrations of the mirror can be reduced and, as for the residual intensity noise, they can only induce common-mode fluctuations of the site potentials. There is strong interest in many of the research fields mentioned above in creating periodic potentials with larger separations between the different sites, which is limited to fraction of μm due to the available narrow-linewidth laser sources.
During my PhD we have realized an innovative, large-spacing optical superlattice based on the beating note between two retroreflected optical lattices with commensurate wavelengths, $n\lambda_2 = (n+1)\lambda_1$. Choosing $n \gg 1$ we demonstrated that the resulting potential is periodic and, for sufficiently low lattice depths, the energy spectrum of the superlattice is equal to the one of an optical lattice with wavelength $n\lambda_2$, so with lattice spacing n time larger than standard retroreflecting lattice. We refer to it as Beat-note Super Lattice (BNSL).
In the framework of atom interferometry, we implemented the BNSL technique in different ultra-cold trapped atom interferometry experiments showing its flexibility. In the first one, we used a 10μm spacing BNSL to realize a spatial Bloch oscillation interferometer which operate in presence of small external forces. When cancelling the interatomic interactions by means of a magnetic Feshbach resonance, the dynamics exhibits a coherence up to 1 s, demonstrating how BNSL provides very stable potentials with a large spatial periodicity.
The second interferometer relies on a multimode configuration in an harmonic trap, where the coherent splitting and recombination of a BEC into multiple momentum components are realized by means of Kapitza-Dirac (KD) diffraction from a pulsed 5 μm BNSL. Here the harmonic trap closes the trajectories of the momentum components, and the BNSL pulses allow to reduce their recoil velocity, hence the oscillation amplitude. This is important, since we need to keep the dynamics in the harmonic region of our optical harmonic trap. A third kind of interferometer, we are currently working on, is based on BEC optically trapped in array of double well potentials. To realize such array we exploit two collinear BNSLs with a periodicity of one twice the other (10μm and 5μm), and to do this I need only three commensurate wavelengths. Each one of this double well represents a sensor I can exploit to realize a Mach-Zehnder interferometer. A preliminary set of measurements, with no external perturbation applied, show correlations between the outputs of each Mach-Zehnder. Having more the one correlated interferometers is possible to perform differential analysis between the outputs to subtract common noise and to realise a trapped atom gradiometer. Our studies are focusing on that goal. A last series of measures performed with our array of double wells potential concerns the possibility to introduce repulsive interaction during the input state preparation to reduce the large noise we are actually observing in the measurements. This goes in the direction of realizing non-classical states (number squeezed state) to enhance the sensitivity of the sensor beyond the standard quantum limit.

Ringraziamenti

Ringrazio il mio supervisor, Marco Fattori, per avermi dato l'opportunità di fare ricerca insieme in questi tre anni di dottorato. Se mi sono appassionato all'attività di laboratorio è grazie anche all' entusiasmo che Marco trasmette nello svolgere questo lavoro.
Voglio ringraziare tutte le persone, ricercatori e non, che ho incrociato nei corridoi del Dipartimento di Fisica e del LENS, per aver dedicato un po' del loro tempo a me e al mio progetto. Ringrazio Giovanni Ferioli e Leonardo Masi, per essere stati miei mentori e avermi passato molti trucchi del mestiere. In particolare Leonardo, che tra una pandemia e un dottorando alle prime armi (io) è riuscito a insegnarmi moltissimo. Ringrazio Giovanni Modugno, per la sua disponibilità e i suoi utili consigli. Grazie a Matteo Zaccanti e ai ragazzi del laboratorio 9, per tutte le cose che ho preso in prestito in questi anni e per la loro assistenza. In particolare ringrazio Andreas per tutti i consulti tecnici. Allo stesso modo ringrazio Francesco Minardi, Alessia Burchianti e il laboratorio 29, con cui ho avuto il piacere di collaborare. Ringrazio tutta l'officina elettronica per il prezioso aiuto ricevuto (e per la pazienza). Un grazie speciale a Francesca e Josephine, che tra un esperimento e tantissimi caffè sono state delle splendide amiche e colleghe. Grazie a Duccio Fanelli per la prontezza con cui, come Direttore, ha sempre risposto alle varie (tantissime) esigenze dei laboratori. Grazie ai nuovi arrivati, Chiara (post-doc e DJ del laboratorio) e Andrea (dottorando), per l'aiuto e l'entusiasmo che stanno dimostrando.
Ci sono molti amici a cui sono grato, perché nonostante i diversi impegni la loro presenza mi è stata fondamentale per arrivare fin qui, ed è ancora oggi una costante nella mia vita. Quindi grazie ai vecchi compagni di studi, che non perdono mai occasione di organizzare una rimpatriata. Grazie agli amici del gruppo musical Dancing Time, perché ogni anno realizziamo insieme qualcosa di unico. Grazie agli amici delle innumerevoli serate giochi, con i quali intavolo discussioni sui temi più strani e disparati. Grazie agli amici di una vita, che ancora oggi mi chiedono in cosa consiste esattamente il mio lavoro, dandomi così l'opportunità di trovare nuove fantasiose spiegazioni. Grazie a Massi, Jacopo, Viola e Martina, perché ci siete sempre stati. Infine ringrazio i miei genitori, che mi hanno sempre supportato in tutto, e mio fratello, perché posso sempre contare su di lui.

Contents

Chapter 0

Introduction

Atom Interferometry, thanks to the use of massive particles, allows to perform measurements of inertial forces[1] and gravity[2] with the highest resolutions, to precisely determinate fundamental constants [3, 4] and to realize experiments to test the equivalence principle[5, 6, 7]. The state of the art of Atom Interferometry is represented by free falling atom interferometers [2], where cold atomic samples, while evolving in the external gravitational field, are split in two separate paths and recombined by multi-photon transitions.
Depending on the phase accumulated along the two paths, the interference pattern at the output provides information about the external perturbation the atom experienced during the interrogation time T. The resolution of those sensors scales as $\Delta \mathrm{kT}^2$, i.e. linearly with the size of the apparatus and with the transferred multi-photon momentum Δk. So, much effort is currently spent to enhance these two quantities.
One possibility is to realize large apparatus [8, 9], but this is technically demanding since we need to shield the wave packets from external noise and to control its spread over large regions of space. Moreover, the spatial resolution is limited by the size. New projects aim to bring atom interferometry in space[10, 11], so that the size of the device is no longer determined by the dropping height, as required on ground. Other solutions include exploiting high order Raman transition[12] or multi-photon Bragg diffraction[13] to enhance Δk.
One very interesting class of sensors is represented by trapped atom interferometers, in which the interferometric steps (initial state preparation, splitting, interrogation time and recombination of the atomic wavefunction) are performed by means of the confining potential itself. In this way atoms are sustained against gravity during the all the sequence, allowing to extend the interrogation time and realize compact devices with high spatial resolution[14]. A small size of the system can allow precision measurements of forces on micrometric scales and it can be exploited for fundamental studies, like the investigation of Casimir effects [15] near surfaces.
Although they are very promising, the problem of inter-atomic interactions in high density trapped samples (like Bose-Einstein condensate) and instabilities of the confining potential reduce the interrogation time and limit the sensitivity of these sensors[14]. In our system, where Bose-Einstein condensate of ^{39}K are used, the possibility of tuning the interaction strength to negligible values by means of Feshbach resonances can help to overcome the first limitation[16, 17].
Among the possible geometries of the confinement potentials, the double-well scheme represents one of the most simple, which has already been exploited for the realization of Mach-Zehnder interferometers with trapped BECs[14]. This latter, combined with the tunability of inter-atomic interactions allows also the creation and the control of quantum entangled states[18], which are of great interest in quantum interferometry community for the operation of interferometric sensors with sub shot noise sensitivity[19, 20, 21].
In the framework of trapped atom interferometry, the goal of our experiments is to study a

Bose-Einstein condensate optically confined and separated in spatial modes whose relative distance can be precisely controlled. Such separation needs to be as large as possible, since in the trapped atom devices the sensitivity scales proportionally to the separation of the trapped modes[17]. However, the geometry of the trapping potential needs to be robust against external source of noise. A configuration with a good intrinsic stability is represented by optical lattices created by retro-reflecting a laser beam of wavelength λ on a single mirror, since it is strongly immune to beam pointing instabilities [22] and the phase noise can be suppressed by stabilizing the mirror motion [2] and the frequency of the laser. In addition, the residual intensity noise of optical lattices is normally not an issue, since it induces common-mode fluctuations of the site potentials. However, the spatial periodicity of optical lattices based on counter propagating beams, $\lambda/2$, is limited to $\sim 1\mu$m with only few exceptions[23], mainly due to the available narrow-linewidth laser sources.
In this thesis I present an innovative, large spacing optical superlattice based on the beating note between two retroreflected optical lattices with slightly different wavelengths λ_1 and λ_2. I show that, when the two wavelengths fulfil the condition $n\lambda_2 = (n + 1)\lambda_1$ with $n \gg 1$ integer, the resulting potential is periodic and, for sufficiently low lattice depths, the energy spectrum of the superlattice is equal to the one of an optical lattice with wavelength $n\lambda_2$. Working with $\lambda_1 \sim \lambda_2$ and n=20 I get an effective lattice period around 10μm.
I refer to this as a Beat-Note Super Lattice (BNSL). Note, in quantum gases experiments lattice with large spacing can be realized exploiting laser beams crossed at a small angle [24]. Unfortunately the smaller is the angle the larger is the sensitivity of the lattice spacing to its fluctuations.
In this work, with BNSL in a horizontal confguration (no gravity component in lattice direction) we have realized different interferometric experiments.
The First one [25] is based on Bloch oscillations in a large spacing optical lattice, which can be exploited to measure weak force in the same way it has been already exploited to measure gravity [26, 27] with high precision. The observed dynamic exhibits a coherence up to 1 s, demonstrating how this new technique provides very stable potentials with a long periodicity.
A second interferometric scheme [28] relies on a multimode configuration, where the coherent splitting and recombination of a BEC into multiple momentum components are realized by means of Kapitza-Dirac (KD) diffraction from a pulsed optical lattice. This scheme was proposed theoretically for noninteracting systems in [29], where the presence of an harmonic potential acts like a "mirror" to close the trajectories and to prevent the spatial spread of wave packets, as it would occur in free space. We have realized a proof of principle demonstration of this scheme showing the limitations of our system and analysing future improvements to enhance its performance.
In a most recent experiment, I study a BEC optically trapped in array of double well potentials. To realize such array I exploit two collinear BNSLs with a periodicity of one twice the other (10μm and 5μm), using three commensurate wavelengths. With BECs loaded in three double wells, I have realized three Mach-Zehnder interferometers operating in parallel. Observing correlations between the outputs of the three sensors we realize an operative trapped atom gradiometer, where differential analysis allows to subtract the common noise acting on the double wells.
Finally, within the same system, I have started to study the reduction of noise in the preparation of the input state of the interferometers, introducing in the system repulsive interactions. This goes in the direction of realizing non-classical states (number squeezed state) to enhance the sensitivity of the sensor beyond the standard quantum limit.

The thesis is structured as follows.

In Chapter 1 I briefly introduce the theory of atoms in optical lattices, describing the physics

of single particles in periodic potentials. In particular I cover aspects like dynamics in presence of an external constant force, Kapitza-Dirac diffraction, and theory of a BEC in a double well potential. Then, I explain the BNSL idea, investigating its properties both analytically and with the help of numerical simulations.
In chapter 2 I describe our experimental platform for the realization of Bose-Einstein condensates with tunable interaction in the beat-note optical lattice, focus the attention on the laser system and techniques to stabilize three frequencies on the same optical cavity.
In chapter 3 main results about long lasting Spatial Bloch oscillations of a BEC in a 10μm BNSL are reported.
In chapter 4 I show the working principle of a Kapitza-Dirac multimode interferometer and its realization in our system.
In chapter 5 I present preliminary results about the Mach-Zehnder trapped atom interferometer with a BEC trapped in the array of double well potential made with BNSL. In chapter 6 I conclude with a discussion of the results that we have obtained so far and the future perspectives offered by our system.

List of publications

- Nałęcz, I., Masi, L., Ferioli, G.,text Petrucciani, T., Fattori, M. and Chwedeńczuk, J., 2020. Sensitivity bounds of a spatial Bloch-oscillation atom interferometer. Physical Review A, 102(3), p.033318.

- Masi, L.,text Petrucciani, T., Ferioli, G., Semeghini, G., Modugno, G., Inguscio, M. and Fattori, M., 2021. Spatial Bloch Oscillations of a Quantum Gas in a "Beat-Note" Superlattice. Physical Review Letters, 127(2), p.020601.

- Masi, L., Petrucciani, T., Burchianti, A., Fort, C., Inguscio, M., Marconi, L., Modugno, G., Preti, N., Trypogeorgos, D., Fattori, M. and Minardi, F., 2021. Multimode trapped interferometer with noninteracting Bose-Einstein condensates. Physical Review Research, 3(4), p.043188.

- Petrucciani, T. et al., Precision gradiometry with an array of trapped atom interferometers, in preparation

Chapter 1

Theory

This chapter has the purpose to introduce the Beat-Note superlattice (BNSL), a novel technique for trapping and manipulating ultracold atoms which I exploited to realize experiments in the field of atom interferometry [25, 28] reported in Chap.3,4, and for some latest measurements in Chap.5.
I explore the validity of such technique and its applicability with a theoretical analysis including numerical simulations, before dealing with the experimental works.
First, I give a brief description of the theory of single particles in optical lattices and I derive the analytic expression of the energy spectrum in presence of weak and deep potentials. Then I give an intuitive description of the evolution of a system of non interacting particles in a lattice when an external force F is present (i.e., the coherent dynamics named Bloch oscillation).
Then, I give a brief description of the mean field theory of a weakly interacting Bose Einstein Condensate (BEC) and I will introduce the two mode approximation that is the basic tool to describe a BEC in a Double Well potential.
Finally, in the two last sections I illustrate how the BNSL works supporting analytical studies with numerical simulations. In particular, I focus on its spectrum in different regimes to underling limitations and advantages of this technique, I show how to realize an array of double wells potential with it and how atom diffraction works with this kind of potential.

1.1 1D Optical Lattices

Neutral atoms interact with light in both dissipative and conservative way. An incident light field $\vec{\mathrm{E}}(\vec{\mathrm{r}},\mathrm{t}) = \hat{e}\tilde{\mathrm{E}}(\vec{\mathrm{r}})\exp(-i\omega\mathrm{t}) + c.c.$ induces a dipole moment in the atom $\vec{\mathrm{p}}(\vec{\mathrm{r}},\mathrm{t}) = \hat{e}\tilde{\mathrm{p}}(\vec{\mathrm{r}})\exp(-i\omega\mathrm{t}) + c.c.$, where the amplitude of the dipole moment is proportional to the field amplitude $\tilde{\mathrm{E}}$ through the complex polarizability α, $\tilde{\mathrm{p}} = \alpha\tilde{\mathrm{E}}$. If you consider the real part of the polarizability $\Re(\alpha)$, which describes the component of $\vec{\mathrm{p}}$ oscillating in phase with $\vec{\mathrm{E}}$, the interaction potential is given by [30]

$$\mathrm{U}_{dip}(\vec{\mathrm{r}}) = -\frac{1}{2\epsilon_0 c}\Re(\alpha)\mathrm{I}(\vec{\mathrm{r}}) = \frac{3\pi c^2}{2\omega_0^3}\frac{\Gamma}{\Delta}\mathrm{I}(\vec{\mathrm{r}}) \tag{1.1}$$

where $\mathrm{I}(\vec{\mathrm{r}}) = 2\epsilon_0 c\left|\tilde{\mathrm{E}}\right|^2$ is the field intensity. In the last equality of 1.1 we can replace the atomic polarizability α calculated in a semiclassical approach for a two-level quantum system interacting with the classical radiation field with no saturation effect. Γ in this picture is the damping rate (corresponding to the spontaneous decay rate of the excited level) and $\Delta = \omega - \omega_0$ is the detuning from atomic resonance ω_0.
The dissipative interaction comes due to the absorption of photons from an incident field,

followed by spontaneous emission. The scattering rate of this process, which is described by the imaginary part of the polarizability, is

$$\Gamma_{sc}(\vec{r}) = \frac{3\pi c^2}{2\hbar\omega_0^3}\Big(\frac{\Gamma}{\Delta}\Big)^2 \mathrm{I}(\vec{r}) \tag{1.2}$$

In case of "red" detuning, $\Delta < 0$, the dipole potential is negative and the atoms are attracted by maximum light intensity regions. The dipole potential scales as $\frac{\mathrm{I}}{\Delta}$, whereas the scattering rate scales as $\frac{\mathrm{I}}{\Delta^2}$. So, optical dipole traps usually use large detunings Δ and high intensities to keep the scattering rate as low as possible at a certain potential depth.
Eq. 1.1 shows that a spatially dependent intensity induces a spatially dependent potential energy. An interesting case is represented by optical lattices, standing wave potentials which provide extremely tight confinement along the axial direction. The simplest possible lattice is a one dimensional (1D) lattice realized by retro reflecting a laser beam or superimposing two counter-propagating lasers with the same frequency ω and amplitude E_0, such that a standing wave interference pattern is created. Let's consider the total field of such configuration,
$\mathrm{E}(\mathrm{x},\mathrm{t}) = \mathrm{E}_0\exp(\mathrm{kx}-\omega\mathrm{t}) + \mathrm{E}_0\exp(-\mathrm{kx}-\omega\mathrm{t}+\phi)$, where $\mathrm{k}= 2\pi/\lambda$ is the wave vector and λ is the wavelength of the radiation. The total intensity, proportional to the square module of total field, is

$$\mathrm{I}(\mathrm{x}) = \frac{1}{2\epsilon_0 c} 4\mathrm{E}_0^2\cos(\mathrm{k_L x})^2 \tag{1.3}$$

where $\mathrm{k_L} = \pi/d$ is the lattice wave vector, related to lattice periodicity by the lattice constant $\mathrm{d}= \lambda/2$. Exploiting 1.1 the energy potential felt by the atoms is

$$\mathrm{V_{latt}}(\mathrm{x}) = \mathrm{V}_0\cos(\mathrm{k_L x})^2 \tag{1.4}$$

where the amplitude V_0 is called "lattice depth". Usually, lattice depth is measured in units of the recoil energy $\mathrm{E_R} = \hbar^2\mathrm{k_L^2}/2m_a$, that represents the main energy scales for atoms of mass m_a in the optical lattice.
In a red detuned optical lattice atoms are strongly confined in the anti-nodes of the standing wave, which are the potential minima. Making a power expansion around a potential minimum (e.g. at $\mathrm{x}= \mathrm{d}/2$) we find that the axial confinement of the optical lattice is

$$\omega_{latt} = \frac{\pi}{\mathrm{d}}\sqrt{\frac{2\mathrm{V}_0}{m_a}} \tag{1.5}$$

which is the harmonic oscillation frequency of an atom trapped inside one of the lattice wells. To be more precise, taking into account the Gaussian profile of the beam, this is the trap frequency at the centre of the trap. The oscillation frequency decreases when moving along the x-axis due to the decreasing light intensity ($\propto \mathrm{E}_0^2$).

1.1.1 Single particle in a lattice (Bloch Theorem)

Atoms interacting with a spatially modulated optical potential resemble in many aspects electrons in the solid crystals ion-lattice potential, and one of the most important characteristics of a periodic potential is the emergence of a band structure, as a results of Bloch's Theorem [31]. The Hamiltonian describing a single particle of mass m_a in a 1D optical lattice is $\mathrm{H}= \frac{\hat{\mathrm{p}}^2}{2m_a} + \mathrm{V_{latt}}(\mathrm{x})$, with $\mathrm{V_{latt}}(\mathrm{x}) = \mathrm{V_{latt}}(\mathrm{x}+\mathrm{ld})$ a potential with periodicity set by the lattice constant d, with l an integer indicating the l-th site. Bloch theorem assures that the eigenstates can be chosen to have the form of a plane wave times a complex function u with the same periodicity of the potential

$$\psi_{\mathrm{k,n}}(\mathrm{x}) = \exp(i\mathrm{kx})u_{\mathrm{n,k}}(\mathrm{x}) \tag{1.6}$$

The wave vector k is an index introduced by the Bloch Theorem, called *quasi momentum*, which can be seen as a quantum number characteristic of the translational symmetry of the periodic potential. It describe how does the phase of the Bloch state change as a result of a translation in the lattice. Because of the discrete invariance of H, k is confined in the so called first Brillouin Zone (BZ), i.e $-\pi/\mathrm{d} < \mathrm{k} < \pi/\mathrm{d}$.
The index n, or *band index*, appears in Bloch's theorem because for a given k there are many solutions to the Schrödinger equation, so each n refers to the n-th energy band.
Without going into too much detail in solving the eigenvalue problem (the reader can find it in [31]), the idea is to write down both 1.6 and the potential $\mathrm{V_{latt}(x)}$ in Fourier series

$$\begin{aligned} \psi_{\mathrm{k,n}}(\mathrm{x}) &= e^{i\mathrm{kx}} \sum_{\mathrm{m}} \mathrm{c_{k-mG}} e^{i(k-\mathrm{mG})\mathrm{x}}, \\ \mathrm{V_{latt}}(x) &= \sum_{\mathrm{m}} \mathrm{U_{mG}} e^{i\mathrm{mGx}} \end{aligned} \tag{1.7}$$

with m integer and where $\mathrm{G}=2\mathrm{k}_L$. If we consider a finite system consisting of a number M of lattice sites, for the periodic boundary condition M represents also the number of discrete values assumed by the quasi-momentum k. So, substituting 1.7 in the Schrödinger equation, we can stop the Fourier series at $|\mathrm{m}|=\mathrm{M}$, obtaining a system of 2M+1 linear equations.

$$\Big(\frac{\hbar^2}{2m_a}(\mathrm{k}-\mathrm{mG})^2 - \mathrm{E}\Big) c^n_{\mathrm{k-mG}} + \sum_{\mathrm{m'}\neq\mathrm{m}} \mathrm{U_{m'G-mG}} \mathrm{c^n_{k-m'G}} = 0 \tag{1.8}$$

For each k, 2M+1 solutions with different energies $\mathrm{E^n}(k)$ exist, with n= 0...2M. To each eigenvalue then it is associated an eigenstate which is given by the Fourier component $\mathrm{c^n_{k-mG}}$. Finally, substituting the latter in 1.7, the Bloch function associated with this solution can be obtained.
For the optical lattice in 1.4 we have $\mathrm{V}_{latt}(\mathrm{x}) = \Big(\frac{\mathrm{V_0}}{2} + \frac{\mathrm{V_0}}{4} e^{i2\mathrm{k_L x}} + \frac{V_0}{4} e^{-i2k_{\mathrm{L}}\mathrm{x}}\Big)$.
Apart from the constant term, the Fourier coefficients $\mathrm{U}_{\pm 2k_{\mathrm{L}}} = \frac{\mathrm{V_0}}{4}$ couples states whose wave vector differ by $\mathrm{G}=2\mathrm{k_L}$. Physically, this process represents the absorption of a photon from a lattice beam with a momentum $\hbar\mathrm{k_L}$ and the consequent stimulated emission of a photon with a momentum $-\hbar\mathrm{k_L}$ in the other beam.

1.1.2 Perturbative approach (shallow lattice)

In the limit of weak potential, i.e. $|\mathrm{V}| = \mathrm{V_0} \ll \mathrm{E_R}$ we can solve analytically 1.8 using a perturbative approach [31]. As a perturbation theory, we need to consider two different cases, depending on whether the two states that are coupled by the potential are degenerate or not.

Non degenerate states
States $\mathrm{c^n_{k-mG}}$ with unperturbed energy $\mathrm{E^0_{k-mG}} = \frac{\hbar^2(\mathrm{k-mG})^2}{2m_a}$ are non-degenerate with level $\mathrm{E^0_{k-m'G}}$ if $\left|\mathrm{E^0_{k-m'G}} - \mathrm{E^0_{k-mG}}\right| \gg \mathrm{U_{mG}}$, $\forall \mathrm{m} \neq \mathrm{m'}$.
Then the general solution for the eigenvalues ϵ is

$$\epsilon^0(\mathrm{k}-\mathrm{m'G}) = \mathrm{E^0_{k-m'G}} + \sum_{\mathrm{m}\neq\mathrm{m'}} \frac{|\mathrm{U_{mG-m'G}}|^2}{\mathrm{E^0_{k-m'G}} - \mathrm{E^0_{k-mG}}} \tag{1.9}$$

Since for an optical lattice $\mathrm{G}= \pm 2\mathrm{k_L}$ and $\mathrm{U}_{\pm 2\mathrm{k_L}} = \mathrm{V_0}/4$, the energy spectrum of the lowest energy band $\epsilon^0(\mathrm{k})$ can be written as

$$\epsilon^0(\mathrm{k}) = \frac{\hbar^2\mathrm{k}^2}{2m_a} + \frac{\mathrm{V_0^2}}{64\mathrm{E_R}\Big[\frac{\mathrm{k}}{\mathrm{k_L}} - 1\Big]} - \frac{\mathrm{V_0^2}}{64\mathrm{E_R}\Big[\frac{\mathrm{k}}{\mathrm{k_L}} + 1\Big]} \tag{1.10}$$

For a particle with k= 0 then $\epsilon(\mathrm{k}=0) = -\frac{\mathrm{V}_0^2}{32\mathrm{E_R}}$

Degenerate states
If there is $\mathrm{N_d}$ states $\mathrm{c_{k-m_i G}}$, with i=1...$\mathrm{N_d}$, such that their energy difference is of the order of Fourier coefficient U, then you have to solve the following system of equation

$$\begin{aligned}\Big(\epsilon(\mathrm{k}) - \epsilon_{\mathrm{k-m_i G}}\Big)\mathrm{c_{k-m_i G}} = &\sum_{j=1, j\neq i}^{\mathrm{N_d}} \mathrm{U_{m_j G - m_i G} c_{k-m_j G}} + \\ &+ \sum_{j=1}^{\mathrm{N_d}} \left(\sum_{\mathrm{m}\neq \mathrm{m_1 ... m_{N_d}}} \frac{\mathrm{U_{mG-m_i G} U_{m_j G - mG}}}{\epsilon(\mathrm{k}) - \mathrm{E^0_{k-mG}}} \right) + \mathrm{O(U^3)}\end{aligned} \tag{1.11}$$

Now we have that there is linear term in U and one of the order of U^2 (while in the non-degenerate case there was only a second order contribution in U).
Since our optical lattice 1.4 is 1D, the maximum degeneracy $\mathrm{N_d} = 2$ the system in 1.11 reduce to a couple of linear equation. If then one takes only the first order contribution in U the solution is

$$\epsilon = \frac{\Big(\mathrm{E^0_{k-m_1 G}} + \mathrm{E^0_{k-m_2 G}}\Big) \pm \sqrt{\Big(\mathrm{E^0_{k-m_1 G}} - \mathrm{E^0_{k-m_2 G}}\Big)^2 + 4|\mathrm{U_{m_1 G - m_2 G}}|^2}}{2} \tag{1.12}$$

that in case of two exactly degenerate states reduce to $\epsilon_{1,2} = \mathrm{E^0_{k-mG}} \pm |\mathrm{U_{m_1 G - m_2 G}}|$.
The coupling with the external potential removes the degeneracy, showing an avoid crossing behaviour. The condition of exact degeneracy is satisfied for $\mathrm{k} = \pm \mathrm{k_L}$, therefore the effect of the potential is the creation of a gap

$$\Delta \mathrm{E_{gap}} = 2|\mathrm{U_{m_1 G - m_2 G}}| = \mathrm{V_0}/2 \tag{1.13}$$

In figure 1.1 are plotted some of the results studied so far.

1.1.3 Tight-binding regime

As the depth of the potential increases, each lattice site resembles an isolated potential well, and the energy bands shown in the Fig. 1.1 will become more and more flat. Within this limit it is expected that the Bloch solutions become increasingly localized near the lattice minima. The wavefunction of the system can be more conveniently written as a superposition of many wavefunctions located at each lattice site x_l, where l is an integer indicating the l-th lattice site. They are defined as:

$$\mathrm{w_n(x - x_l)} = \frac{1}{\sqrt{\mathrm{M}}} \sum_{BZ} e^{-i\mathrm{k x_l}} \psi_{\mathrm{n,k}}(\mathrm{x}) \tag{1.14}$$

where the sum is over the first Brillouin zone $\Big($to pass from discrete to continuous case replace the $\sum$ with $\sqrt{\frac{\mathrm{d}}{2\pi}} \int_{\mathrm{BZ}} \mathrm{dk}\ \Big)$.
Those are the so called Wannier functions, which become strongly localized as the lattice depth increases. In this approximation one can only take into account overlap between Wannier functions in nearest neighbour sites. If initially the atoms are prepared in the lowest band, then we can restrict to Wannier functions of only the lowest band, $\mathrm{w_0(x - x_l)}$. Then, we can expand the lowest band wavefunction on the basis of Wannier functions and study the temporal evolution of the wave packet resolving the discrete Schrödinger equation. If

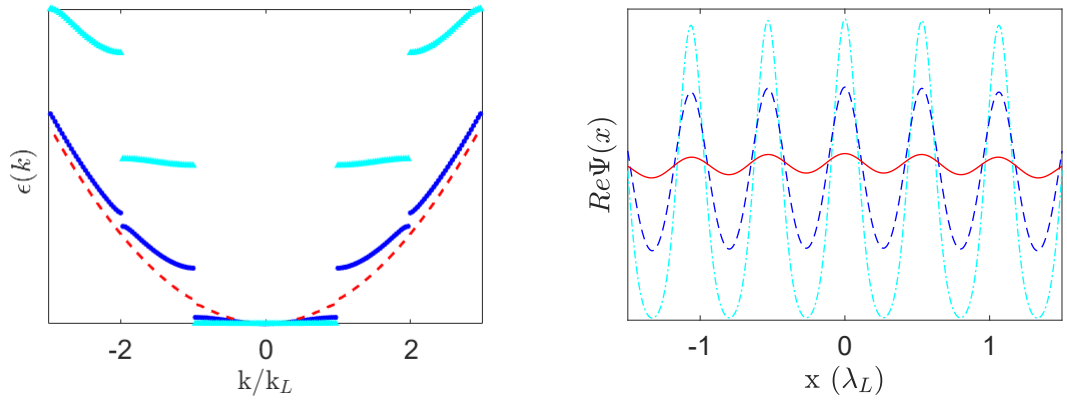

Figure 1.1: Left: spectrum of a particle in a optical lattice showing the first three energy band for three different depths, $\frac{V_0}{E_R} = 0.45$ (red-dashed line),$\frac{V_0}{E_R} = 4.5$ (Blue circle) and $\frac{V_0}{E_R} = 18$ (light blue triangle). For low V_0 in the dispersion relation energy gaps are so small that the spectrum almost resume that of a free particle (quadratic dispersion), while for $V_0 > E_R$ an energy gap between the first two bands appears (k= k_L). For even grater V_0, energy gap begins to open also at k= $2k_L$ and the bands become flatter.
Right: real part of the lowest band wavefunction with k = 0 for three different depths of the periodic potential, $\frac{V_0}{E_R} = 0.45$ (red line),$\frac{V_0}{E_R} = 4.5$ (Blue dashed line) and $\frac{V_0}{E_R} = 18$ (light blue dashed-dot line). Increasing the lattice depth, the wavefunction changes from a weakly modulated plane wave to a function that is strongly localized on the lattice sites (for this numerical calculation, λ =1.064nm).

we consider again the optical lattice potential in 1.4, it's possible calculate analytically the dispersion law ϵ(k) and the tunneling energy between nearest neighbouring lattice sites J

$$\begin{aligned} \epsilon(k)/E_R &= \sqrt{\frac{V_0}{E_R}} - 2J\cos(kd) \\ J &= \frac{4}{\sqrt{\pi}}\left(\frac{V_0}{E_R}\right)^{\frac{3}{4}} e^{-2\sqrt{\frac{V_0}{E_R}}} \end{aligned} \tag{1.15}$$

From this point let's introduce the dimensionless parameter s= $\frac{V_0}{E_R}$ to refer to lattice depth. As we can see, J decays exponentially with the lattice depth s, and so the energy dispersion of low-lying bands are only weakly dependent on the quasi-momentum k (see Fig. 1.1,left) In this regime, around each minimum we can make the harmonic approximation $V(x) = V_0\cos^2(k_L x) \simeq V_0 k_L^2 x^2 = 1/2 m_a \omega_L^2 x^2$, where ω_L defines an effective trapping frequency $\omega_L = \sqrt{\frac{2V_0 k^2}{m_a}}$

1.1.4 Dynamics of non interacting atoms in a lattice

Let's now study linear matter-wave propagation in which only Bloch states in one band are involved, in absence or in presence of an additional external potential

Pure periodic potential

The temporal evolution of a wave packet in an optical lattice can be described by decomposing the initial wavefunction into Bloch states $\psi_{k,n}(x)$ with the corresponding amplitude $f_n(k)$, and the subsequent evolution is purely a consequence of the accumulated phase $\Phi_{n,k}(t) = \epsilon^n(k)t/\hbar$ [32]:

$$\psi(\mathrm{x},\mathrm{t}) = \sum_{\mathrm{n}} \int_{\mathrm{BZ}} \mathrm{f_n(k)}\psi_{\mathrm{k,n}}(\mathrm{x}) e^{\Phi_{\mathrm{n,k}}(\mathrm{t})}\,\mathrm{dk} \tag{1.16}$$

The description becomes very simple if the quasi-momentum distribution only involves a small range of quasi-momenta centered around $\mathrm{k_0}$ (i.e., the spatial extent of this wavepacket is much larger than the lattice spacing) and only one band (e.g., the lowest band) is involved. We can refer to this as a semiclassical approximation, for which the energy dispersion relation band structure can be approximated by a Taylor expansion:

$$\epsilon(\mathrm{k}) = \epsilon(\mathrm{k_0}) + (\mathrm{k}-\mathrm{k_0})\frac{\partial\epsilon(\mathrm{k})}{\partial \mathrm{k}}\Big|_{\mathrm{k=k_0}} + \frac{(\mathrm{k}-\mathrm{k_0})^2}{2}\frac{\partial^2\epsilon(\mathrm{k})}{\partial \mathrm{k}^2}\Big|_{\mathrm{k=k_0}} + ... \tag{1.17}$$

Substituting 1.17 into 1.16 it is easy to see that the wave-packet moves with the group velocity

$$\mathrm{v_g(k_0)} = \frac{1}{\hbar}\frac{\partial\epsilon(\mathrm{k})}{\partial \mathrm{k}}\Big|_{\mathrm{k=k_0}} \tag{1.18}$$

as well as a packet of electromagnetic waves having a dispersion relation $\omega(\mathrm{k})$ and a velocity $\frac{\partial\omega}{\partial \mathrm{k}}$. In analogy to the spreading of a wave packet in free space due to the dispersion relation $\mathrm{E_R} = \hbar^2\mathrm{k}^2/2m_a$, the matter wavepacket in the optical lattice also spreads, but with a modified dispersion described by the effective mass m_{eff}.

$$m_{\mathrm{eff}}(\mathrm{k_0}) = \hbar^2 \left(\frac{\partial^2\epsilon(\mathrm{k})}{\partial \mathrm{k}^2}\Big|_{\mathrm{k=k_0}}\right)^{-1} \tag{1.19}$$

Dynamics with additional potential (Bloch oscillation)

Let's introduce an external force F on the system always with the assumption that the width of the wave packet in quasi-momentum space is small, thus the wave packet can be characterized by a single mean quasi-momentum $\mathrm{k_0}$. The external force then leads to a time-dependent $\mathrm{k_0(t)}$ such that $\hbar\dot{\mathrm{k}}_0(\mathrm{t}) = \mathrm{F}$, and if F is constant then k evolves linearly in time $\mathrm{k_0(t)} = \mathrm{k_0(t=0)} + \mathrm{Ft}/m_a$ [31]. Since k is define module π/d with d lattice constant, the evolution is periodic with period $\tau_{\mathrm{B}} = h/\mathrm{Fd}$ [33, 34]. τ is the so called Bloch period, the time $\mathrm{k_0}$ need to scan a full Brillouin zone.
The group velocity 1.18 depends on k, so the width of the wave packet in momentum space continuously changes (which is the quantity measured in the laboratory experiments when you release the atoms). This periodic evolution is known as Bloch oscillation in real space [34, 35].
If the force F generate an energy gradient between the sites large respect to the depth of the lattice, the so called Landau-Zener tunneling occurs [36]. In particular, when the k reaches the boundary of the Brillouin zone, the tunneling probability across the gap is given by [32]

$$\begin{aligned} \Gamma_z &= \mathrm{e}^{-\mathrm{a_c/a}} \\ \mathrm{a_c} &= \frac{\mathrm{V_0^2 d}}{16\hbar^2} \end{aligned} \tag{1.20}$$

depending on lattice spacing d and the potential $\mathrm{V_0}$, with a the acceleration induced by F.
Let us now relax one of the starting condition and take a width of the wave packet in quasi-momentum space comparable with the width of Brillouin zone (i.e., few lattice sites are occupied by the atoms.)
To simplify the analysis, we can consider a tight binding model and a single-band approximation (e.g. lowest band, n=0) and exploit the notion of Wannier states 1.14 to write the tight binding hamiltonian as [37]

$$\mathrm{H} = \sum_l (\mathrm{E_0} + \mathrm{Fdl})\,|l\rangle\langle l| + J\sum_l (|l+1\rangle\langle l| + |l-1\rangle\langle l|) \tag{1.21}$$

where J is the tunneling energy between neighbouring sites and, given the energy spectrum $\epsilon(\mathrm{k})$ in 1.15, $\mathrm{E_0} = \mathrm{E_R}\sqrt{\mathrm{V_0/E_R}}$. The Hamiltonian 1.21 leads to a discrete spectrum $\mathrm{E}_l = \mathrm{E_0} + \mathrm{Fd}l$ knows as Wannier-Stark ladder [38], and the correspondent eigenfunctions $|\phi_l\rangle = \sum_j \mathcal{J}_{j-l}\left(\frac{J}{2\mathrm{dF}}\right)|j\rangle$ are knows as Wannier-Stark states, with $\mathcal{J}_{j-l}(z)$ ordinary Bessel function. The Wannier-Stark states are localized in space with a localization length l_{WS} that depends on the force applied on the lattice: if dF>J (strong force) then $\mathrm{l}_{WS} = 1$ (in unit of lattice period d) while $\mathrm{l}_{WS} \sim \frac{\mathrm{J}}{\mathrm{Fd}}$ for dF<J (weak force).
Now, the general solution of the Schrödinger equation can be written as a sum over the Wannier-Stark states

$$\psi(\mathrm{x,t}) = \sum_l \mathrm{c}_l \mathrm{e}^{i\mathrm{E}_l \mathrm{t}/\hbar}\phi_l(\mathrm{x}) \tag{1.22}$$

and the dynamics is represented by an oscillation of the center of mass of the wave packet, where l_{WS} defines the maximum distance where the wave-packet can move to.

In the end to resume, we can say that the choice of how many initial sites are occupied is crucial, cause it set where the dynamics is easier to be experimentally observed. For atoms (the reader imagines loading a degenerate gas as a Bose Einstein condensate in the lattice) spread over many sites the width of momentum distribution is narrower then the FBZ, so when k changes in time due to the presence of a constant force also the width of momentum distribution changes. So, if we release the cloud from the trap and observe it in far field we can detect a clear oscillation.
For atoms load in phew site instead the width of momentum distribution is larger then the whole FBZ, try to detect its evolution in far field is not convenient. We can observe anyway an in situ dynamics of the centre of mass of the cloud, assuming that your resolution allows to resolve single site scale.
As a limit case, consider the initial state strongly localized in the site l=0. Then, as stated above, the centre of mass dynamic is frozen. Anyway it still possible observe a periodic evolution of the system, but this time the observable is the width of wave packet in real space[35]. Indeed, the evolution of the wavepacket

$$\begin{aligned} |\psi(\mathrm{t})\rangle &= \sum_l \mathrm{c}_l(t)\,|l\rangle \\ \mathrm{c}_l(\mathrm{t}) &= \mathcal{J}_l\left(\mathrm{A}\sin\left(\frac{\pi \mathrm{t}}{\tau_\mathrm{B}}\right)\right) e^{il(\pi - \omega_\mathrm{B}\mathrm{t})/2} \end{aligned} \tag{1.23}$$

In such a breathing mode, the wavepackets widen and shrink periodically populating an interval $|l| < A$, where A= 4J/Fd.

1.1.5 Kapitza-Dirac scattering

When atoms diffract from a standing light wave, each two-photon (absorption-stimulated emission) scattering event changes the atomic momentum along the standing wave by either zero or $2\hbar\mathrm{k_L}$, which for multiple such events results in a series of evenly spaced atomic momenta. The kind of scattering depends on the strength and duration of the interaction with the light field [39, 40], and in particular when interaction is sufficiently short and strong we talk about Kapitza-Dirac scattering [41, 42]. Kapitza–Dirac scattering is a kind of scattering that can be properly described by neglecting particle motion over the duration of the interaction. Consider an atomic wavefunction $\Psi(x)$ subject to a 1D standing wave potential for a certain time, then the Schrödinger equation reads

$$i\hbar\partial_t\Psi(\mathrm{x,t}) = \left[-\frac{\hbar^2}{2m_a}\partial_\mathrm{x}^2 + \mathrm{sE_R}\sin^2(\mathrm{kx}+\phi)\right]\Psi(\mathrm{x,t}) \tag{1.24}$$

where E_R is the recoil energy, s=V/E_R the a-dimensional lattice depth parameter and ϕ lattice phase. At t=0, before the potential is turned on, we have a wavepacket $\Psi_0(x)$. If the pulse duration τ is short enough, then we fall within Raman-Nath limit, which allows to neglect the kinetic energy term in the Hamiltonian [42]. In that limit, the only effect of the lattice is to imprint a phase on the wavefunction. Then we can write

$$\begin{aligned}\Psi(kx,\tau) &= \Psi_0(x)\exp\left[-i\frac{\tau E_R}{\hbar}\frac{s}{2}\Big(1-\cos(2kx+2\phi)\Big)\right] = \\ &= \Psi_0(x)\exp(-i\beta)\sum_{n=-\inf}^{n=+\inf} i^n \mathcal{J}_n(\beta)\exp[-in(2kx+2\phi)]\end{aligned} \tag{1.25}$$

Where in the last equality I use of the identity for Bessel functions $\mathcal{J}$ of the first kind, with $\beta = \frac{\tau E_R}{\hbar}\frac{s}{2}$. Considering only n=0,±1 we have then three component of momenta p=0,±2ħk with amplitudes

$$\begin{aligned}&\mathcal{J}_{+1}(\beta)\exp\left[i(\frac{\pi}{2}-2\phi)\right]\\ &\mathcal{J}_0(\beta)\\ &\mathcal{J}_{+1}(\beta)\exp\left[i(\frac{\pi}{2}+2\phi)\right]\end{aligned} \tag{1.26}$$

As pointed out in the beginning, to restrict the atomic motion during the interaction time to distances small compared to the characteristic dimensions of the interaction potential requires short interaction times. For a standing wave interaction, this approximation is well satisfied if the atomic motion during the interaction time is small compared to the wavelength of the illuminating radiation. As a result, Kapitza–Dirac scattering is limited (relative to Bragg scattering) to short interaction times,τ, generally much smaller than the inverse recoil frequency ($\tau \ll \omega_{rec}$) [43]. To observe appreciable population transfer at such short times, large intensities are needed.

1.1.6 Talbot Effect

Splitting condensate in several momentum components can be used to probe coherence properties of BEC in particular regime where interesting physics happens, or it can also be used for realization of matterwave interferometry. Diffraction by optical lattice it is also a tool to get knowledge about the lattice depth with high precision [32]. Indeed, to calibrate lattice depth by mean of 1.1 one has to know the intensity, i.e. waist and power of the beam. Beam waist in the position of the atomic clouds it's really difficult to measure due to propagation through optics and windows of vacuum system, while measurements of the absolute optical power have systematic errors on the order of 20%. An alternative method makes use of Raman-Nath diffraction [41].
If the lattice is switched on suddenly for a time $\Delta t < 1/\omega_{rec}$, with ω_{rec} recoil frequency, the resulting diffraction pattern is in the Raman-Nath regime and the value of V_0 can be calculated from the relative populations in the 0 and 2ħk momentum components. This method has the advantage of needing only a short interaction time with the lattice.
However, for lattice depth ≤1 E_R, with E_R the recoil energy, the diffracted population are small. In order to increase the signal it's possible to employ a multi-pulse diffraction that coherently adds the effects of each pulse[44]. For shallow lattice only order with |q| ≤1 are populated, and for initially stationary atoms |q| =1 orders (i.e.±2ħk momenta components) are equivalent and can be represented as a single state. So, to get a more intuitive picture, we can describe the system as a two level system, hence exploit the Bloch sphere picture. Component q=0 is the north pole of the sphere and |q| =1 are the south pole.
Free evolution corresponds to precession about the vertical axis with period $\hbar/(4E_R)$, called

the Talbot time [45]. So, we start with the atomic state vector aligned with the north pole. During a weak lattice pulse, the precession axis is tilted from the vertical axis by an angle proportional to the lattice depth, and state vector start to rotate around it for an half precession period $\hbar/(8E_R)$. After that, once the lattice pulse is ended, free evolution for another $\hbar/(8E_R)$ makes the state vector rotate around the vertical axis. Alternating lattice and free evolution with duration $\hbar/(8E_R)$ efficiently increases the diffracted population.
To calculate the populations P transferred in |q| =1 after N pulses we refers to the work [46]. In the weakly diffracting limit P_0 and P_1 oscillate sinusoidally with the number of pulses N, with amplitude and frequency which depend solely on the dimensionless lattice depth V/E_R. For $V \ll E_R$ it results that P_1 has a quadratic dependence by N.

$$P_1 = 8(V/2E_R)^2 N^2 \propto N^2 \tag{1.27}$$

In Fig.1.2 I show a numerical simulation for P_1 as function of the number of pulses N for a lattice with $\lambda = 1\mu$m and different depths.

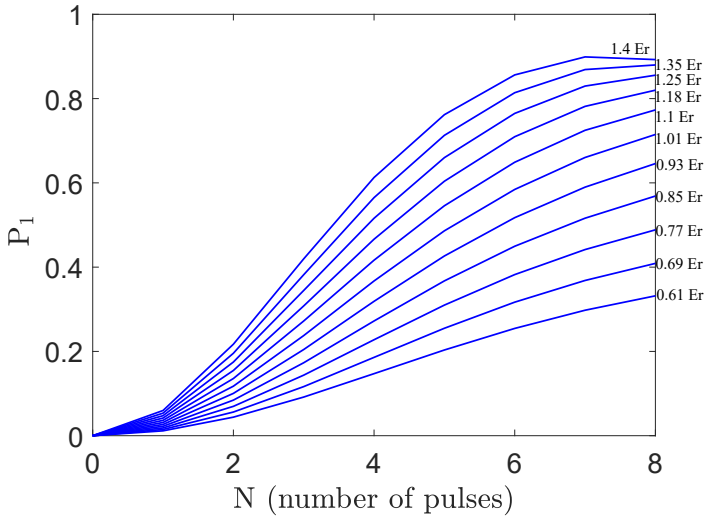

Figure 1.2: Numerical simulation of population transferred in order |q| =1 ($\pm 2\hbar$k) as function of the number of pulses N for a lattice with $\lambda = 1\mu$m and different depths.

1.2 BEC in a Double well potential

In this section I will shortly discuss the theory of a BEC in a double well potential.

1.2.1 Weakly interacting BEC

A system made by N interacting bosons in external potential $V_{ext}(\vec{r})$ can be approached with the formalism of second quantization. In this framework, the many-body Hamiltonian operator becomes

$$\begin{aligned} H = &\int d^3r \Psi^\dagger(\vec{r}) \left(-\frac{\hbar^2}{2m_a}\nabla + V_{ext}(\vec{r}) \right) \Psi(\vec{r}) + \\ &+ \frac{1}{2} \int d^3r d^3r' \left(\Psi^\dagger(\vec{r}) \Psi^\dagger(\vec{r'}) V_{int}(\vec{r} - \vec{r'}) \Psi(\vec{r}) \Psi(\vec{r'}) \right) \end{aligned} \tag{1.28}$$

where $\Psi(\vec{r})$ and $\Psi^\dagger(\vec{r})$ are the field operators satisfying the bosonic commutation rules, $N=\int d^3r\Psi^\dagger(\vec{r})\Psi(\vec{r})$ is the atom number operator and $V_{int}(\vec{r}-\vec{r'})$ is the inter-particle interaction potential.
For ultracold dilute bosonic sample the average distance between particles is larger then the range of the interatomic forces, and the collisional energy is so low that one can make use of the pseudo-potential approximation [47] to write $V_{int}(\vec{r}-\vec{r'})$ as a contact potential

$$V_{int}(\vec{r}-\vec{r'}) = g\delta(\vec{r}-\vec{r'}) \tag{1.29}$$

where $g=\frac{4\pi\hbar^2 a_s}{m_a}$ and a_s the s-wave scattering length, the only parameter in this picture that describes the strength of the interaction between two identical ultracold atoms. Thanks to Feshbach resonances [48], a_s can be tuned in experiments by applying a uniform magnetic field, making it possible to change the sign of the interactions.
The field operator is defined as $\Psi(\vec{r}) = \sum_i \psi_i(\vec{r})\hat{a}_i^\dagger$, where $\hat{a}_i^\dagger$ is the single particle creation operator of the i-th state described by the wave-function $\psi_i(\vec{r})$.
If we assume that the cloud is all condensed in the ground state of the system, i.e. it is a dilute gas at very low temperature $T\simeq 0$, then we have a macroscopic occupation of a single quantum state, and we can make the so called Mean-Field (MF) approximation. This mean that all the creation and annihilation operators of states different from the ground state can be neglected.
Then we can ask that

$$\hat{a}_0^\dagger = \sqrt{N_0} \longrightarrow \Psi(\vec{r},t) \simeq \sqrt{N_0}\psi_0(\vec{r},t) \tag{1.30}$$

where N_0 is the number of atoms in the ground state and ψ_0 is the wavefuntion of the condensate. Substituting Eq. 1.29 and Eq. 1.30 in the many-body Hamiltonian (1.28) we obtain the so-called time-dependent Gross-Pitaevskii equation [49]

$$i\hbar\frac{d\psi_0(\vec{r},t)}{dt} = \left[-\frac{\hbar^2}{2m_a}\nabla + V_{ext}(\vec{r}) + gN_0|\psi_0|^2\right]\psi_0(\vec{r},t) \tag{1.31}$$

If we search for stationary solutions $\psi_0(\vec{r},t) = \psi_0(\vec{r})\exp(-i\mu t/\hbar)$, we get that μ is the chemical potential of the atomic cloud. So we can rewrite Eq. 1.31 and obtain the equation

$$\left[-\frac{\hbar^2}{2m_a}\nabla + V_{ext}(\vec{r}) + gN_0|\psi_0|^2\right]\psi_0(\vec{r}) = \mu\psi_0(\vec{r}) \tag{1.32}$$

1.2.2 Two-mode Approximation

Quantum harmonic oscillator characterized by a trapping frequency ω has discrete eigenvalues equally separated by $\hbar\omega$. The effect of rising up a barrier in the centre of this potential is to reduce the energy difference between the ground state and the first excited one, as well as the one between the second and third excited states (and so on).
In the linear case (no interactions among the particles in such potential) both ground and first excited state are well defined, and correspond to that of a single particle. However, in presence of interactions, the exact definition of ground and first excited state is not trivial, due the fact that it's a manybody problem.
To simplify the description we ask that the scales of energy involved (temperature and interaction energy) are way lower then the separation from the excited states, which is of the order of $\hbar\omega$. This is the so called Two-Mode Approximation, which allow to rewrite the field operator Ψ with the following expression

$$\Psi = \psi_g\hat{a}_g + \psi_e\hat{a}_e \tag{1.33}$$

where $\psi_{g,e}$ are the wave functions of the symmetric and antisymmetric ground states of stationary Gross-Pitaevskii equation Eq. 1.32 with chemical potential $\mu_{g,e}$, while $\hat{a}_{g,e}$ are the correspondent destruction operator. In Fig. 1.3 is reported a picture of the double well potential and of its symmetric and anti-symmetric GPE ground states . We refers to the energy separation between the two lowest level as J=E_e-E_g.

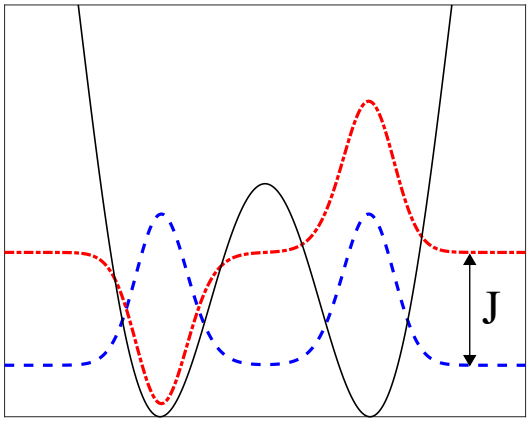

Figure 1.3: Double well potential (black line) and its symmetric (blue dashed line) and antisymmetric (red dashed-dot line) ground states. The energy difference between this two levels is the tunneling J

A more suitable base to describe the system is obtained using the wave function localized in the left or right well

$$\begin{aligned} \psi_{R(L)} &= \frac{1}{\sqrt{2}}(\psi_g \pm \psi_e) \\ \hat{a}_{R(L)} &= \frac{1}{\sqrt{2}}(\hat{a}_g \pm \hat{a}_e) \end{aligned} \tag{1.34}$$

By plugging the ansatz in Eq. 1.34 in the many body Hamiltonian in Eq. 1.28, with some algebra, we get [50]:

$$\hat{\mathrm{H}}_{2\mathrm{M}} = \frac{\mathrm{E}_c}{8}\left(\hat{a}_L^\dagger \hat{a}_L - \hat{a}_R^\dagger \hat{a}_R\right)^2 - \frac{\mathrm{E_J}}{\mathrm{N}}\left(\hat{a}_L^\dagger \hat{a}_R + \hat{a}_R^\dagger \hat{a}_L\right) + \frac{\delta \mathrm{E}}{4}\left(\hat{a}_L^\dagger \hat{a}_R + \hat{a}_R^\dagger \hat{a}_L\right)^2 \tag{1.35}$$

where

$$\begin{aligned} &\mathrm{E}_c = 8\mathrm{K}_{g,e}, \\ &\mathrm{E_J} = \frac{\mathrm{N}\left(\mu_e - \mu_g\right)}{2} - \frac{\mathrm{N}(\mathrm{N}+1)}{2}\left(\mathrm{K}_{e,e} - \mathrm{K}_{g,g}\right) \\ &\delta \mathrm{E} = \frac{\mathrm{K}_{e,e} + \mathrm{K}_{g,g} - 2\mathrm{K}_{g,e}}{4} \\ &\mathrm{K}_{i,g} = \frac{\mathrm{g}}{2}\int d\mathrm{r}|\psi_i|^2|\psi_j|^2 \quad \text{with} \quad i,j = g,e \end{aligned} \tag{1.36}$$

and N the total number of particles. The coupling term proportional to $\mathrm{E_J}$ describes the tunneling of particles from one well to the other, the one proportional to E_c (on-site interaction energy) corresponds to the local interaction within the two wells, and the term proportional to δE describes two particle processes like two particle tunneling. Usually in experiments, this last term is negligible respect to the other two, so it will be neglected in this work. Introducing the population imbalance (i.e. atom number difference) operator

$\hat{n} = \left(\hat{a}_L^\dagger \hat{a}_L - \hat{a}_R^\dagger \hat{a}_R\right)/2$ and the tunneling operator $\hat{\alpha}_+ = \left(\hat{a}_L^\dagger \hat{a}_R + \hat{a}_R^\dagger \hat{a}_L\right)/\mathrm{N}$, the two mode hamiltonian in Eq. 1.35 reads

$$\mathrm{H_{2M}} = \frac{\mathrm{E}_c}{2}\hat{n}^2 - \mathrm{E_J}\hat{\alpha}_+ \tag{1.37}$$

which is know as the Bose-Hubbard Hamiltonian for the double well system.
Note, the atom number operator expectation value range is $[-\frac{\mathrm{N}}{2}, \frac{\mathrm{N}}{2}]$.

Spectrum of the Bose-Hubbard Hamiltonian

A good choice of basis to diagonalize the Hilbert space is the one made by the N+1 Fock states $|n\rangle = \left|\frac{\mathrm{N}}{2}+n\right\rangle_L \left|\frac{\mathrm{N}}{2}-n\right\rangle_R$, with $n \in [-\frac{\mathrm{N}}{2}, \frac{\mathrm{N}}{2}]$.
The limited size of the Hilbert space allows exact numerical diagonalization of the two mode Hamiltonian. Anyway, at low energy ($\mathrm{E}<2\mathrm{E_J}$) it is also possible find an analytical solution to this problem.
A generic state of the system can be written as a superposition of the N+1 Fock states defined above, then applying Eq. 1.37 to such superposition one can see that the eigenstate values are organized in couple of equal values, separated like in a harmonic oscillator by a constant amount $\hbar\omega_p$, where

$$\omega_p = \frac{1}{\hbar}\sqrt{\mathrm{E_J}\left(\mathrm{E}_c + \frac{4\mathrm{E_J}}{\mathrm{N}^2}\right)} \tag{1.38}$$

is the well known plasma frequency.

1.2.3 Mean Field description of the Two-mode model

We can start again from the ansatz for the localized wavefunction 1.34 and within the mean-field approximation we make the sequent substitution:

$$\hat{a}_L = \sqrt{\mathrm{N}_L}e^{i\phi_L} \quad \text{and} \quad \hat{a}_R = \sqrt{\mathrm{N}_R}e^{i\phi_R} \tag{1.39}$$

where $\mathrm{N}_{L,R}$ are the populations of the localized modes and $\phi_{L,R}$ the phases. With Eq. 1.39 is possible to get a simpler version of the two mode Hamiltonian.
Following [50, 51], starting from the Gross-Pitaevskii equation Eq. 1.31 we can introduce a the quantity

$$\mathrm{n} = \frac{(\mathrm{N}_L - \mathrm{N}_R)}{2} \quad \text{and} \quad \phi = \phi_L - \phi_R \tag{1.40}$$

where n is the population imbalance and ϕ is the relative phase. In the end, the effective two mode Gross-Pitaevskii Hamilton function assumes the form:

$$\mathrm{H}_{GP2M} = \frac{\mathrm{E}_{c-GP}}{2}\mathrm{n}^2 - \mathrm{E}_{\mathrm{J}-GP}\sqrt{1-\frac{4\mathrm{n}^2}{\mathrm{N}^2}}\cos\phi + \frac{\delta\mathrm{E_{GP}}}{2}\left(1-\frac{4\mathrm{n}^2}{\mathrm{N}^2}\right)\cos(2\phi) \tag{1.41}$$

where

$$\begin{aligned}
\mathrm{E}_{c-GP} &= \frac{2}{\mathrm{N}}\frac{10\gamma_{g,e} - \gamma_{g,g} - \gamma_{e,e}}{4}, \\
\mathrm{E}_{J-GP} &= \frac{\mathrm{N}\,(\mu_e - \mu_g)}{2} - \frac{\mathrm{N}}{2}\,(\gamma_{e,e} - \gamma_{g,g}) \\
\delta\mathrm{E}_{GP} &= \frac{\mathrm{N}}{2}\frac{\gamma_{e,e} + \gamma_{g,g} - 2\mathrm{K}_{g,e}}{4} \\
\gamma_{i,g} &= \frac{\mathrm{g}}{2}\int d\mathrm{r}|\psi_i|^2|\psi_j|^2 \quad \text{with} \quad i,j = g,e
\end{aligned} \tag{1.42}$$

For large N and small δE the Bose-Hubbard and the Gross-Pitaevskii constants are approximately equal, and considering that for high value of the barrier the overlap of ψ_L and ψ_R in the place of the barrier is negligible, we can go further with simplification in analogy to Eq. 1.37. In this limit, introducing the normalized atom number difference z= $\frac{2\mathrm{n}}{\mathrm{N}} = \frac{\mathrm{N}_L - \mathrm{N}_R}{\mathrm{N}}$, the effective Hamiltonian can be written as

$$\mathrm{H_{2Meff}} = \frac{\mathrm{E}_c}{2}\mathrm{N}^2\frac{\mathrm{z}^2}{4} - \mathrm{E_J}\sqrt{1-\mathrm{z}^2}\cos\phi \tag{1.43}$$

which is the well known equation that describes the Bosonic Josephson Junction in the mean field model[17].
Note, the interaction term depends on atom number difference between the two wells. When all the atoms are in one of the two wells, the interaction term is maximum (minimum) for E_c>0 (<0). z=0 means N_L=N_R (equally populated wells), and the minimum of energy happens for $\phi = 0$, i.e. for the symmetric state of the double well potential, while we have the maximum energy for $\phi = \pi$, the anti-symmetric one.
From all this picture turns out that the variables n (i.e. z) and ϕ are conjugate, and their equations of motion can be written in the canonical form $\frac{\partial}{\partial t}\phi = \frac{\partial}{\partial \mathrm{n}}\mathrm{H_{2Meff}}$ and $\frac{\partial}{\partial t}\mathrm{n} = -\frac{\partial}{\partial \phi}\mathrm{H_{2Meff}}$. The classical hamiltonian in Eq. 1.43 can be quantized replacing the conjugated variables with operators satisfying the commutation relation $[\hat{\phi},\hat{n}]$=i [52], which introduces quantum fluctuations in the equilibrium state of the system. These fluctuations are directly related to measurable observables. For example, if one calculates the in situ imbalance of two separated condensates with a fixed relative phase ϕ, the variance of n will be given by

$$(\Delta\mathrm{n})^2 = \langle\hat{n}^2\rangle - \langle\hat{n}\rangle^2 = \frac{1}{2}\sqrt{\frac{\mathrm{E_J}}{\mathrm{E}_c + 4\mathrm{E_J}/\mathrm{N}^2}} \tag{1.44}$$

The product of the fluctuations leads to an uncertainty relation of the form

$$(\Delta\mathrm{n})^2 \times (\Delta\phi)^2 \geq \frac{1}{4} \tag{1.45}$$

where the equality is valid for the ground state.
Note, for E_c =0 (null interaction) $(\Delta\mathrm{n}) = \frac{\sqrt{\mathrm{N}}}{2}$, which is the so called "shot noise limit", corresponding to the fundamental minimum value of uncertainty reachable with uncorrelated particles. On the other hand, the presence of the interaction between the atoms of the gas leads to have fluctuations in the number of particles lower than those that occur in the previous case. About that, we can define the squeezing factor ξ_N as [14]

$$\xi_N = \frac{\Delta\mathrm{n}}{\sqrt{\mathrm{N}}/2} = \left(\frac{\mathrm{E_J}}{\mathrm{E_J} + \mathrm{N}^2\mathrm{E}_C/4}\right)^{1/4} \tag{1.46}$$

Summarizing, as the interaction increases, the fluctuations of the number of atoms decrease, and states with a well-defined number of atoms are therefore energetically favoured.

1.3 Beat-Note Superlattice

Consider a system formed by a particle of mass m_a in presence of a potential energy

$$V_B^{1,2}(x) = V_1 \sin^2(k_1 x + \phi_1) + V_2 \sin^2(k_2 x + \phi_2) \tag{1.47}$$

associated with two optical lattices with amplitudes $V_1$and V_2, wavevectors $k_{1,2} = 2\pi/\lambda_{1,2}$ and wavelength $\lambda_{1,2}$, which fulfil the commensurability condition $(n+1)\lambda_1 = n\lambda_2$, with n an integer. For $n \gg 1$, the particle feels an effective periodic potential characterized by a large spacing periodicity $d_- = \pi/(k_1 - k_2) = n\lambda_1/2$ and a short spacing amplitude modulation $d_+ = \pi/k_+$, with $k_+^{1,2} = (k_1 + k_2)/2$. This potential, with n=20, λ_1 =1013.7 nm and λ_2 =1064.5 nm, was implemented experimentally in [25] where it was called Beat-note Superlattice (BNSL), Fig 1.4.

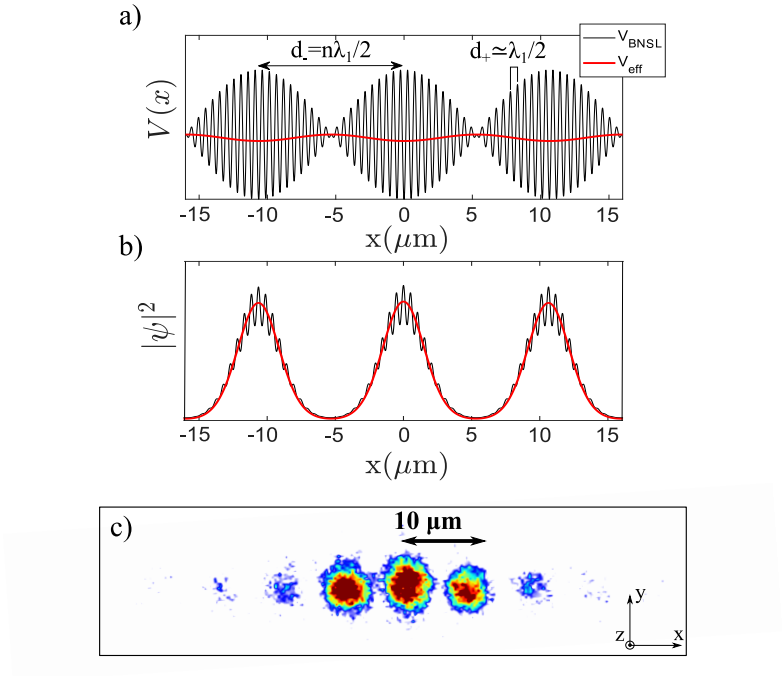

Figure 1.4: BNSL with n=20, λ_1 =1013.7 nm and λ_2 =1064.5 nm as reported in [25]. a) Plot of the beat-note optical lattice (thin line) and the correspondent effective potential V_{eff} (thick line). b) Profile of the ground-state atomic wavefunction in presence of a BNSL with a depth V_1 =V_2 =$0.5E_{R+}$ (thin line) and in presence of a standard large spacing optical lattice with a depth equal to the effective depth of the BNSL (thick line). c) Density distribution of a non interacting condensate in the ground state of the BNSL that shows the spatial modulation with a period of 10 μm.

In order to give the right interpretation about how the BNSL works as large spacing periodic trap for cold atoms, let's rewrite 1.47 in a more convenient way. Both term on the right part of 1.47 can be rewrite as $V_i/2(1 - \cos(2k_i x + 2\phi_i))$ with i=1,2, then, if we add and subtract to each one of them $\left(\frac{V_1 - V_2}{4}\right)\cos(2k_i x + 2\phi_i))$ we can rewrite the potential as

$$\left(\frac{V_1+V_2}{4}\right)\Big[2-\cos(2k_1 x + 2\phi_1)-\cos(2k_2 x + 2\phi_2)\Big]-\left(\frac{V_1-V_2}{4}\right)\Big[\cos(2k_1 x + 2\phi_1)-\cos(2k_2 x + 2\phi_2)\Big].$$

Now, if we apply prostapheresis formula to both terms in the square brackets we get

$$\left(\frac{V_1+V_2}{2}\right) + \left(\frac{V_1+V_2}{2}\right)\cos\Big(2k_+^{1,2}x + \phi_1 + \phi_2\Big) + \left(\frac{V_1-V_2}{2}\right)\sin\Big(k_-^{1,2}x + \phi_1 - \phi_2\Big)$$

where $k_-^{1,2} = k_1 - k_2$. Now, in order to apply the sum identities, we can introduce

$$\cos(\theta_{1,2}) = -\frac{\left(\frac{V_1+V_2}{2}\right)\cos\left(k_-^{1,2}x+\phi_1-\phi_2\right)}{A^{1,2}(x)} \text{ and } \sin(\theta_{1,2}) = \frac{\left(\frac{V_1-V_2}{2}\right)\sin\left(k_-^{1,2}x+\phi_1-\phi_2\right)}{A^{1,2}(x)}.$$

Imposing the identity $\cos^2(\theta_{1,2}) + \sin^2(\theta_{1,2}) = 1$ we can easily find

$$A^{1,2}(x) = \sqrt{\frac{V_1^2+V_2^2}{4} + \frac{V_1V_2}{2}\cos\left(2k_-^{1,2}x + \phi_1 - \phi_2\right)}$$

So, the potential 1.47 can be rewrite as

$$V_B^{1,2}(x) = \left(\frac{V_1 + V_2}{2}\right) + A^{1,2}(x)\cos\left(2k_+^{1,2}x + \phi_1 + \phi_2 - \theta_{1,2}\right) \tag{1.48}$$

Expression 1.48 highlights the presence of a single lattice with a fast spatial frequency $k_+^{1,2}$ and a slow varying amplitude $A^{1,2}(x)$. To make it easier to visualize, let's consider the case $V_1 = V_2 = V_0$. Then expression 1.48 can be rewrite as

$$V_B(x) = V_0 - V_0\cos\left(k_-^{1,2}x + \phi_1 - \phi_2\right)\cos\left(2k_+^{1,2}x + \phi_1 + \phi_2\right) \tag{1.49}$$

So, for $n \gg 1$, expression 1.49 says that the sum of two initial lattices, except for constant term, can be seen as a single (primary) lattice which has a fast spatial oscillation on a distance provided by $d_+ = \pi/k_+^{1,2}$ modulated over a large length scale by $\cos\left(k_-^{1,2} + \phi_1 - \phi_2\right)$. To see how from the slow modulation of potential 1.49 it is possible to confine and separate atoms over distances set by $d_- = \pi/k_-^{1,2} = n\lambda_2/2$ (see Fig. 1.4b) we need to proceed with a perturbative approach.

1.3.1 Perturbative regime

As pointed out in [53] a quantum particle evolving in a potential with a periodic spatial modulation experiences an attractive effect in comparison to a constant one with the same average value. The reason is that, although the modulation naturally increases the kinetic energy due to a coupling to high momentum states, the resultant modulation of the wavefunction, with maxima localized at the minima of the trap, causes a stronger reduction of the potential energy. In the perturbative regime, i.e $V_0 < E_{R_+}$, where $E_{R_+} = \hbar^2(k_+^{1,2})^2/2m_a$ is the recoil energy of the primary lattice, this "attractive" effect can be quantify by estimating the second order energy shift of a general momentum state k due to its coupling to states whose wavevector differs by $\pm 2k_+^{1,2}$.
Indeed, consider 1.49 as a potential with an amplitude $V_B = V_0\cos\left(k_-^{1,2}x + \phi_1 - \phi_2\right)$ roughly constant. So, if the Fourier components of 1.49 are made explicit

$$V_B(x) = V_0 - V_0\left(\frac{e^{i(2k_+^{1,2}x+\phi_1+\phi_2)}}{2} + \frac{e^{-i(2k_+^{1,2}x+\phi_1+\phi_2)}}{2}\right) \tag{1.50}$$

then the Bloch theory, as showed in sec 1.1.1 , asserts that through 1.50 a particle in the general momentum state k interacts only with states whose wavevector differs from k by a "reciprocal lattice vector", i.e. by $\pm 2k_+^{1,2}$.
In the perturbative limit $V_0 \ll E_{R_+}$, such theory says that energy correction $\Delta\epsilon$ of a particle in the momentum state k ($\forall k \in$ first Brillouin zone, except for the edge of the zone itself) is

$$\Delta\epsilon = -\frac{|V_B/2|^2}{\frac{\hbar^2(2k_+^{1,2})^2}{2m_a} - \frac{\hbar^2(k)^2}{2m_a}} - \frac{|V_B/2|^2}{\frac{\hbar^2(-2k_+^{1,2})^2}{2m_a} - \frac{\hbar^2(k)^2}{2m_a}} \tag{1.51}$$

which means

$$\Delta\epsilon(x) = V_{eff}(x) = -\frac{V_0^2 \cos^2(k_-^{1,2}x + \phi_1 - \phi_2)}{8E_{R_+}}\left(\frac{1}{1-(\frac{k}{k_+^{1,2}})^2}\right) \tag{1.52}$$

In the limit of $k \ll k_+^{1,2}$ such correction is independent by k and it correspond to an effective potential $V_{eff}(x) = V_0 - \frac{V_0^2 \cos^2(k_-^{1,2}x+\phi_1-\phi_2)}{8E_{R_+}}$. So, the potential energy of an atom in such trap is lower in regions where the modulation amplitude is larger, which is where the atom localizes.
The validity of this approximation for $V_0 \ll E_{R_+}$ is confirmed in Fig 1.5a, where the energy spectrum and the wavefunction of a particle in a BNSL with $V_0 \simeq 0.3E_{R_+}$ and in the potential $V_{eff}(x)$ are compared. In addition, Fig. 1.5b,c the wavefunctions of two different quasi-momentum states of the lowest band are reported.

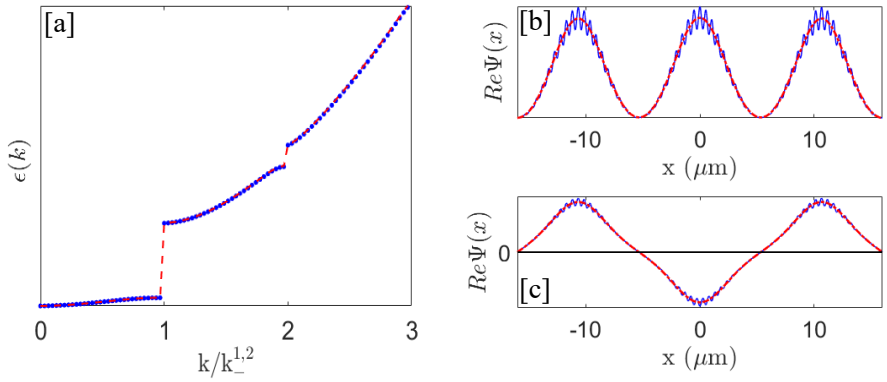

Figure 1.5: a) Comparison between the energy dispersion relation of a BNSL (blue dots) and that of $V_{eff}(x)$ (red dashed line) for $V_0/E_{R_+} \simeq 0.3$. Comparison between the wavefunction of the states with quasi-momentum $k = 0$ (b) and $k = k_-^{1,2}$ (c) for a BNSL (blue line) and the effective sinusoidal potential $V_{eff}(x)$ (red dashed line).

In order to test the validity of this approximation, in Fig. 1.6 we propose the same comparison for different values of V_0. Note that for $V_0 \approx E_{R_+}$, even if the analogy does not hold, it is possible to match approximately the first three energy bands of the BNSL with that of $V_{eff}(x)$ by multiplying their value with a proper coefficient (see red line in Fig. 1.6a,b,c).
For $V_0 > E_{R_+}$ the analogy is lost (see Fig. 1.6d,e,f).
As shown in Fig. 1.7 this occurs when the tunneling energy between the lattice sites separated by $\pi/k_+^{1,2}$ becomes of the order of the energy gaps, inducing a strong modulation of the atomic wavefunctions (see Fig. 1.6e,f).
It is important to stress that for $V_0 \approx E_{R_+}$, the BNSL depth parameter $s = V_{eff}(x)/E_{R-} = E_{R+}/(8E_{R-}) \propto n^2$ can be very large for $n \gg 1$, i.e. for large spacings between the sites of the BNSL. This means that for the BNSL the tunneling between sites separated by d_-, $J_{eff} \approx E_{R-}s^{3/4}e^{\sqrt{s}}$, becomes negligible (see Fig. 1.6a,d, the first energy band becomes flat for $V_0/E_{R_+} \geq 1$) and the BNSL can create arrays of independent clouds in each site separated by d_-. One can see the peculiarity of the spectrum for larger values of V_0, where the analogy with a large spacing standard lattice is no longer valid, looking at the first two energy gaps of the BNSL plotted in Fig. 1.7. The first energy gap of the BNSL deviates from the linear behaviour, while the second one reaches a maximum and then decreases to zero. The reason for this is to be found in the role that the phase difference $\phi_1 - \phi_2$ assumes in the regime of high depth, as it will be pointed out in the next paragraphs.

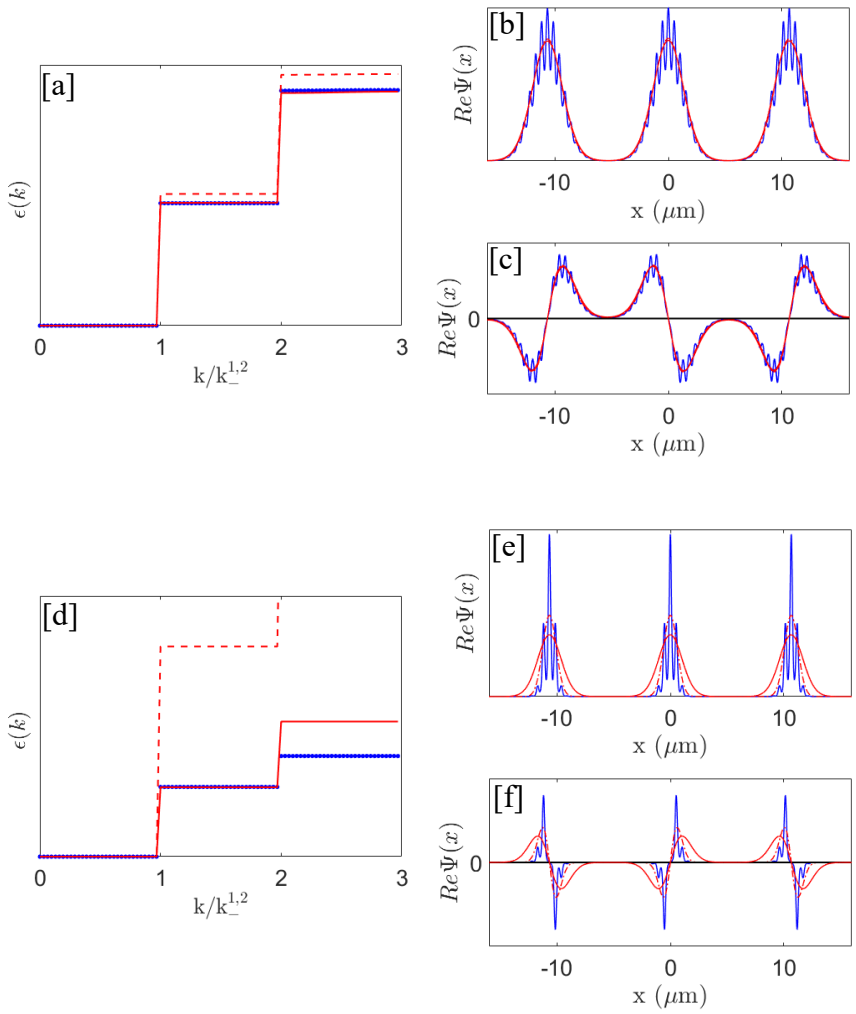

Figure 1.6: a) Comparison of the energy dispersion relation of a BNSL (blue dots) and that of of $V_{eff}(x)$ (red dashed line) for $V_0/E_{R_+} \simeq 1$. For this depth the analogy starts to fail but we can recover it with a simple rescaling of the depth of the effective lattice (red line). b) The ground state density probability between a BNSL (blue line) and $V_{eff}(x)$ (red dashed line) and $V_{eff}(x)$ rescaled. c) Same comparison for the lowest momentum state of the first excited band of the spectrum.
d,e,f) $V_0/E_{R_+} \simeq 4.5$. For this depth the structure of the spectrum of a BNSL becomes completely different from the one of a single wavelength lattice with the same periodicity and the rescaling cannot be applied anymore.

1.3.2 Band structure

To better understand the origin of gaps at $k = mk_-^{1,2}$, with m= 1, 2, ...*etc* in the band structure showed in Fig 1.6,1.7 let's go back to what stressed in the paragraph 1.1.2 for states at the edge of Brillouin zone in the perturbative regime. The state at $k=k_-^{1,2}$ is degenerate with $k= -k_-^{1,2}$ and the linear term in 1.11 can only couple states whose momenta differ by $2k_{1,2}$, so it cannot justify the presence of gaps with multiply of $k_-^{1,2}$. The second order term instead contains two different Fourier components, that can belong to the two different lattices.
Such term represents a two-photon process (absorption and stimulated emission) in a lattice, with momentum transfer $\pm\hbar k_1$, and another two-photon process in the other lattice, with momentum transfer $\mp\hbar k_2$, in total $\pm\hbar(2k_2 - 2k_1) = \pm 2\hbar k_-^{1,2}$. It is responsible for the creation of corresponding energy gaps.

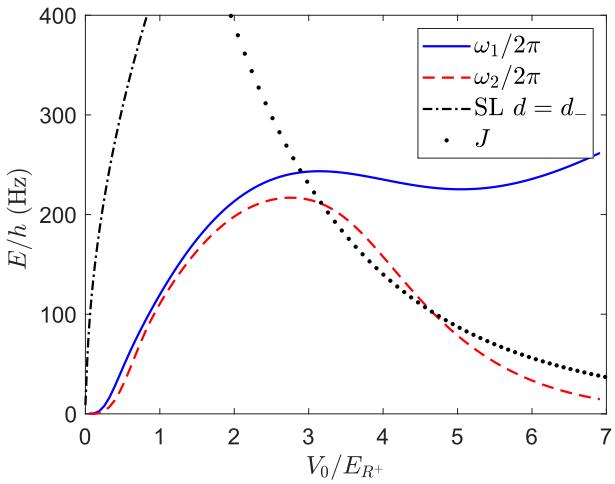

Figure 1.7: a) Theoretical calculations of the first (blue solid line) and the second (red dashed line) energy gaps of the BNSL with $d_- = 10\mu$m and $\phi_1 - \phi_2 = 0$ as a function of V_0. In addition we plot the energy gap of a single lattice with periodicity d_- (dashed-dotted line) and the tunneling energy J (dotted line) in a lattice with periodicity d+. Note that the bifurcation of the two energy gaps and their deviation from the ones of a single lattice with depth V_0^2/E_{R_+} occurs when J becomes comparable to the energy gaps.

About the amplitude of such gaps, we have to estimate the term in brackets in 1.11. The magnitude of the two Fourier components, by equation 1.49, is $|V_0/4|$.
As for the detuning in the denominator, we can consider an atom in the momentum state $k = k_-^{1,2}$ (first Brillouin zone) acquiring an extra $2k_2$ by a lattice. The energy difference between the initial and intermediate state is
$\frac{\hbar^2(2k_2-(k_2-k_1))^2}{2m_a} - \frac{\hbar^2(k_2-k_1)^2}{2m_a} = 4E_R\frac{n+1}{n}$.
Considering also the other lattice, for an extra $-2k_1$, and that everything above applies if the initial state is $k = -k_-^{1,2}$, then energy gap at the edge of the first Brillouin zone of the BNSL is

$$\Delta E_{gap} = \frac{V_0^2}{16E_{R_1}\left(\frac{n+1}{n}\right)} \tag{1.53}$$

with $E_{R_1} = \hbar^2(k_1)^2/2m_a$. This result is in agreement with the relation 1.52, since the value of the first energy gap for it is $\frac{1}{2}\frac{V_0^2}{8E_{R_+}}$ (see theory in par.1.1.2).

1.3.3 Array of Double Wells potential

Double well potentials have been used to realize atom interferometers using Bose Einstein condensates trapped in two spatial modes [14]. In previous experiments [17, 54, 16]we created an array of double well potentials, i.e. an optical superlattice, exploiting two couples of laser beams crossed at a small angle and forming optical lattices with a large spacing. A large lattice constant is required to load a macroscopic number of atoms in a single well. The operation of such devices are strongly affected by trapping instabilities, that leads to a fast loss of coherence; indeed, smaller is the angle and larger is the sensitivity of the lattice spacing to its fluctuations.
A new configuration immune to noise sources might lead to superior performances, and a reliable configuration is the one that exploits retro-reflected beams by a single mirror [22], where the position of the minima of the potential depends only on the relative frequency of the lasers and the vibrational noise of the retro-reflecting mirror. With the current technologies, it is possible, for example, to stabilize the frequency below the Hz level with an

ultra-stable cavity or a frequency comb and the vibration of the mirror can be reduced with anti-vibrational platforms [2].
So, one interesting solution is offered by a superlattice composed by two lattices with one spatial periodicity equal to half the other. This configuration realizes an array of double wells where the two modes are spatially separated by half the value of the shorter wavelength, when the optical lattices are realized with beams retroreflected on a mirror. Unfortunately, the spatial periodicity of optical lattices based on counter-propagating beams is limited to the range from 0.2 to 0.7 μm, with only few exceptions [23], mainly due to the available narrow-linewidth laser sources. High densities and consequent strong three body losses limit the maximum atom number that can be manipulated in such potentials.
The solution proposed in this thesis is the use of a couple of large spacing BNSLs, exploiting only three laser beams whose wavelengths fulfil the conditions

$$\begin{aligned} (\mathrm{n}+1)\lambda_1 &= \mathrm{n}\lambda_2 \\ (\mathrm{n}-1)\lambda_3 &= (\mathrm{n}+1)\lambda_1 \end{aligned} \tag{1.54}$$

with n integer $\gg 1$ (see Fig. 1.8).
The beating between λ_1 and λ_2 creates an effective lattice with lattice spacing $\mathrm{n}\lambda_2/2$, while the beating of λ_3 and λ_1 generates an effective lattice with spacing $\mathrm{n}\lambda_2/4$, i.e. exactly equal to half the first one. The latter has the function of creating potential barriers in place of the potential minima of the first one, which in the end realizes the splitting of atomic wavefunctions in the two spatial modes.
However the introduction of the third lattice gives rise to an interference effect between lasers with wavelengths λ_2 and λ_3 that creates a second effective lattice with spacing $\mathrm{n}\lambda_2/2$ that will unavoidably interfere with the other BNSL with the same periodicity. We show in the following that such interference is destructive when the choice of the lattice phases fulfil the balanced double well condition.
To derive the effective potential provided by the sum of three optical lattice $\mathrm{V}_i \sin(\mathrm{k}_i\mathrm{x}+\phi_i)^2$ let's start from result 1.48 for the lattice λ_1 and λ_3

$$\mathrm{V}_B^{1,3}(\mathrm{x}) = \Big(\frac{\mathrm{V}_1+\mathrm{V}_3}{2}\Big) + \mathrm{A}^{1,3}(\mathrm{x})\cos\Big(2\mathrm{k}_+^{1,3}\mathrm{x}+\phi_1+\phi_3-\theta_{1,3}(\mathrm{x})\Big) \tag{1.55}$$

Considering the choice of the wavelengths in 1.54 we have $\mathrm{k}_+^{1,3} = \mathrm{k}_2$. As a consequence the total potential

$$\mathrm{V}_B^{1,2,3}(\mathrm{x}) = \mathrm{V}_B^{1,3}(x) + \mathrm{V}_2\sin(\mathrm{k}_2\mathrm{x}+\phi_2)^2 \tag{1.56}$$

is the sum of two potentials with the same fast spatial periodicity $\lambda_2/2$. Applying the half angle trigonometric identity on the second term of Eq. 1.56 and then the sum formula of the derived expression one gets

$$\mathrm{V}_B^{1,2,3}(\mathrm{x}) = \frac{\mathrm{V}_1+\mathrm{V}_2+\mathrm{V}_3}{2} + \mathrm{B}(\mathrm{x})\cos(2\mathrm{k}_2\mathrm{x}) + \mathrm{C}(x)\sin(2\mathrm{k}_2\mathrm{x}) \tag{1.57}$$

where $\mathrm{B}(\mathrm{x}) = \mathrm{A}^{1,3}(\mathrm{x})\cos(\phi_1+\phi_3-\theta_{1,3}(\mathrm{x})) - \frac{\mathrm{V}_2}{2}\cos(2\phi_2)$
and $\mathrm{C}(\mathrm{x}) = -\mathrm{A}^{1,3}(\mathrm{x})\sin(\phi_1+\phi_3-\theta_{1,3}(\mathrm{x})) + \frac{\mathrm{V}_2}{2}\sin(2\phi_2)$.
Since B(x) and C(x) are slowly varying function, the overall potential can be written, except constant terms, as a single lattice with spatial periodicity $\lambda_2/2$ and amplitude $\sqrt{\mathrm{B}^2(\mathrm{x})+\mathrm{C}^2(\mathrm{x})}$ (this is easy to see if one writes the last two term of 1.57 in complex form).
According to 1.52 the effective potential is $\mathrm{V}_{\mathrm{eff}}^{1,2,3} = -(\mathrm{B}(\mathrm{x})^2+\mathrm{C}(\mathrm{x})^2)/(8\mathrm{E}_{\mathrm{R}_2})$, then with few

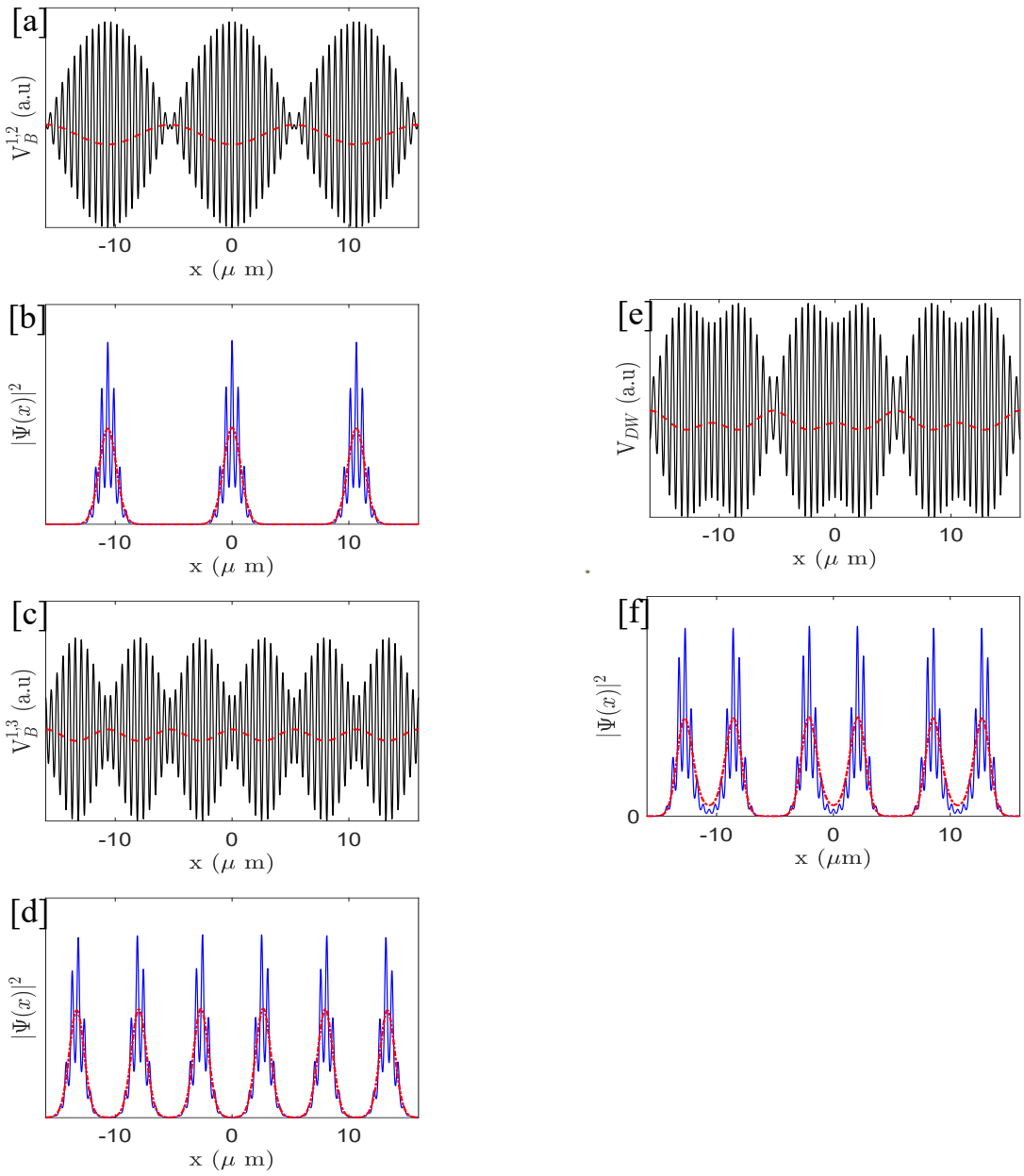

Figure 1.8: a) Plot of the BNSL (thin black line) with n= 20, $\lambda_1 = 1013.7$nm, $\lambda_2 = 1064.5$nm and $\phi_1 = \phi_2 = 0$ and the correspondent effective potential $V_{\text{eff}}^{1,2}$ (thick red dashed line). b) Profile of ground-state atomic wavefunction in presence of BNSL (blue thin line) and $V_{\text{eff}}^{1,2}$ (thick red dot-dashed line) with $V_1 = V_2 \simeq 1.5 E_{R_+}$.
c) Plot of the BNSL (thin black line) with n= 20, $\lambda_1 = 1013.7$nm, $\lambda_3 = 1120.4$nm and $\phi_3 = \phi_1 + \pi/2$ and the correspondent effective potential $V_{\text{eff}}^{2,3}$ (thick red dashed line). As one can notice, in this case the spacing is $d_{1,3} = d_{1,2}/2 = \frac{1}{2}(n\lambda_2/2)$, i.e. half that of $V_{\text{eff}}^{1,2}$, and the two of them are in counterphase. d) Profile of ground-state atomic wavefunction in presence of BNSL (blue thin line) and $V_{\text{eff}}^{2,3}$ (thick red dot-dashed line) with $V_1 \simeq 1.5 E_{R_+}$ and $V_3 \simeq 0.75 E_{R_+}$.
The combination of this two lattice give rise to the pattern in e), an array of double wells separated (thin black line) by $d_{1,2}$ whose spatial modes are separated by $d_{1,3}$ ($V_{\text{eff}}^{1,2,3}$ is represented by thick red dashed line). f) Profile of ground-state atomic wavefunction in presence of the combination of the two BNSL (blue thin line) and $V_{\text{eff}}^{1,2,3}$ (thick red dot-dashed line).

calculations we get

$$\begin{aligned} V_{\text{eff}}^{1,2,3}(x) = \frac{V_1+V_2+V_3}{2} - \frac{1}{8E_{R_2}} \times \Big[\frac{V_1^2+V_2^2+V_3^2}{4} + \\ + \frac{V_1V_3}{2}\cos\Big(2k_-^{1,3}x + 2(\phi_1-\phi_3)\Big) + \\ + \frac{V_1V_2}{2}\cos\Big(k_-^{1,3}x + 2(\phi_1-\phi_2)\Big) + \\ + \frac{V_2V_3}{2}\cos\Big(k_-^{1,3}x + 2(\phi_2-\phi_3)\Big)\Big] \end{aligned} \tag{1.58}$$

where $E_{R_2} = \frac{\hbar^2 k_2^2}{2m_a}$. In order to achieve an array of balanced double wells we choose $\phi_1 = \phi_2$ and $\phi_3 = \phi_2 + \pi/2$. In the end, constant term aside,

$$V_{\text{eff}}^{1,2,3}(x) = -\frac{V_1V_3}{16E_{R_2}}\cos\Big(2k_-^{1,3}\Big) - \frac{V_2(V_1-V_3)}{16E_{R_2}}\cos\Big(k_-^{1,3}x\Big) \tag{1.59}$$

So, the idea is to first load the atoms in the minima of the effective potential provided by lattice 1 and 2, with amplitude $\frac{V_1V_2}{16E_{R_2}}$. Then, increasing the depth of lattice3, we rise a barrier in the centre of every well with amplitude $\frac{V_1V_3}{16E_{R_2}}$. At the same time the interference between lattice 2 and 3 reduces the amplitude of second effective potential in Eq.1.59, which become null when $V_3 = V_1$.
For different values of ϕ_3 all the double wells acquire an energy mismatch between the right and the left modes.
It is worth to notice in the end that, once the conditions between the three phases are fulfil, ϕ_1 is a free parameter which doesn't change the profile of effective potential (its value changes only the position of minima of fast spatial modulation with respect to the slowly varying envelope that sets the effective potential felt by the atoms.)
To complete this analysis, I also studied the behaviour of the eigenvalues of the direct sum of three optical lattice $V_B^{1,2,3} = \sum_i V_i \sin(k_i x + \phi_i)^2$ and that of the effective potential in Eq. 1.59 as a function of V_3 in three different regimes. For sake of simplicity, I restrict my simulation to a single DW. Note, According to 1.59, once the depth of the BNSL made by k_1 and k_2 has chosen, V_3 needs to be smaller than $V_{1,2}$ not to loose the DW configuration.

In Fig. 1.9 the eigenvalues in Hz of the first three excited eigenstates are reported, from which the eigenvalues of the ground state has been subtracted as common offset. In this way, the blue-dots (BNSL Double well) and blue-continues lines (effective Double well) in the images show the trend of the Tunneling Energy.
With reference to Fig.1.6, the depths $V_1 = V_2 = V_0$ are chosen in the region where the BNSL made by k_1 and k_2 can be described by an effective potential, in particular $V_0 = 0.2\ E_{R_+}$,1 E_{R_+},2 E_{R_+}. We can see that, up to $V_0 = E_{R_+}$, Eq. 1.59 is a good approximation of $V_B^{1,2,3}$, while for $V_0 = 2E_{R_+}$ starts to fail (even if, looking at Fig. 1.9, it seems that it's only a matter of rescaling). As for the BNSL made by k_1 and k_2, when the depth is to large the structure of the spectrum shows a peculiar behaviour, so I will dedicate to it the next paragraph.

1.3.4 Large depth regime

Consider again the BNSL in equation 1.49. As shown in Fig. 1.7(d,e,f) when lattice depth $V_0 > E_{R_+}$ the modulation of the atomic wave-function due to fast periodicity set by $k_+^{1,2}$ is more and more relevant, and BNSL develops its own energy spectrum.
The validity of effective potential picture begins to fail when the atomic wavefunction starts

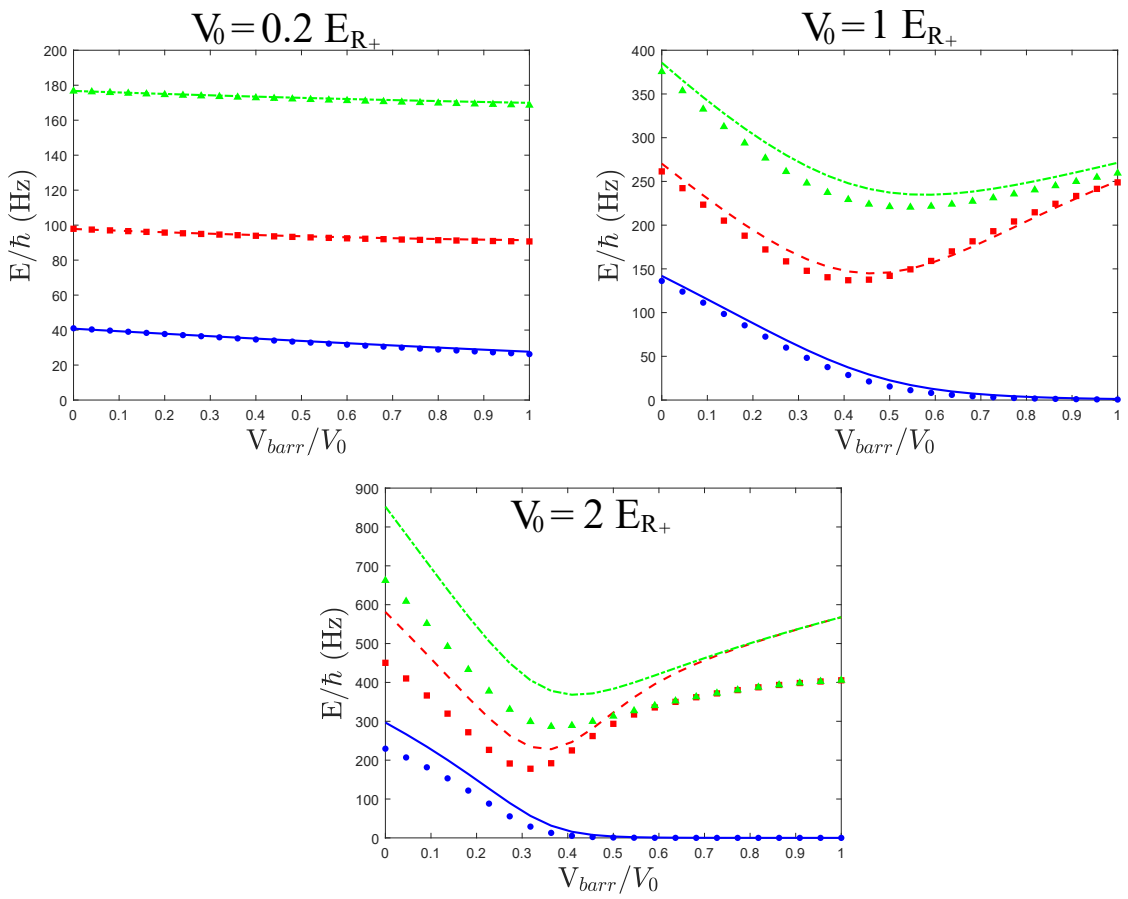

Figure 1.9: Eigenvalues in Hz of the first three excited eigenstates as function of barrier depth $V_{barr} = V_3$ in three different regimes. The eigenvalue of the ground state has been subtracted from the other as common offset. Blue-dot represent then the tunneling energy of the double well system made by $V_B^{1,2,3} = \sum_i V_i \sin(k_i x + \phi_i)^2$, while blue continuos line is the effective potential in Eq. 1.59.
Red square and green triangles are the eigenvalues of the second and third excited state, while red dashed line and green dashed-dot line are the eigenvalues for the correspondent states of the effective potential.

to localize in the minima of the primary lattice $\cos\left(2k_+^{1,2}x + \phi_1 + \phi_2\right)$. To understand when this occurs, it useful look at two energy terms, the tunneling J between the sites separated by $\pi/k_+^{1,2}$ and their potential energy difference δ provided by the slowly varying envelope of the BNSL, Fig1.10.

By 1.15 the tunneling J in tight-binding regime is $\propto s^{3/4} e^{2\sqrt{s}}$, where $s = V_0/E_{R_+}$.
To estimate δ one can proceed as follow:
Eq. 1.49 with $\phi_1 = \phi_2 = 0$ has a minimum in $x = 0$, and the next one is at $x_M = \pi/(2k_+^{1,2})$. Evaluating 1.49 at x_M and considering that $k_-^{1,2} \gg k_+^{1,2}$ with a little bit of algebra we get

$$\delta \simeq V_0 \frac{2\pi^2}{(2n+1)^2} \tag{1.60}$$

As long as $\delta < J$, the possibility to tunnel between the sites separated by $\pi/k_+^{1,2}$ is so large that you can consider the energy levels in such wells degenerate, as it happens for any optical lattice. In this regime the effective potential picture is still valid.
When $\delta \geqq J$, δ is what mostly determines the energy spacing. The reason why in Fig. 1.7 the

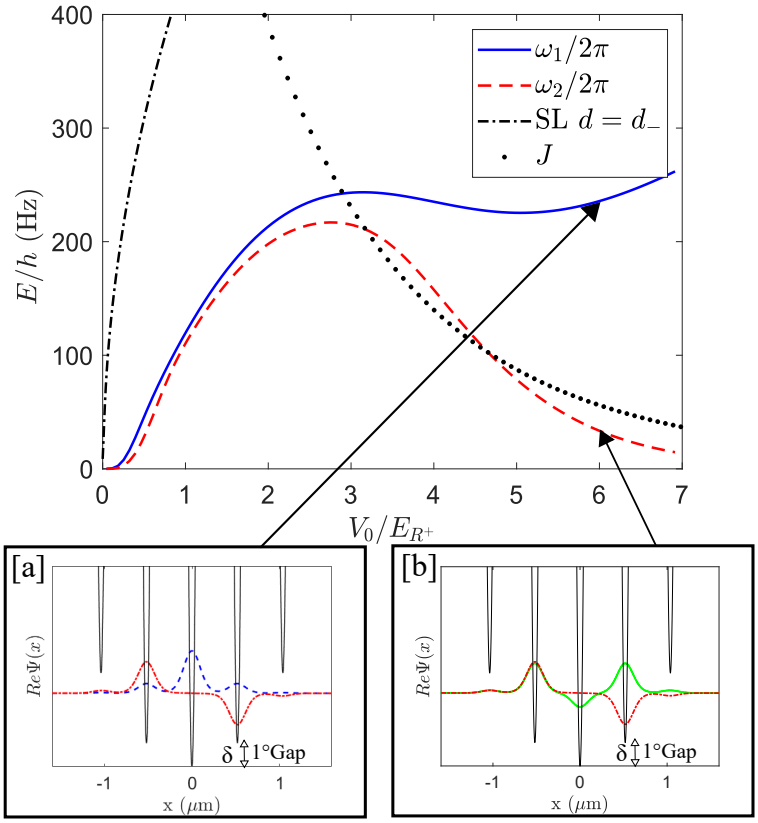

Figure 1.10: This picture show the same spectrum reported in Fig.1.7.
Inset a) shows the BNSL potential around the minimum, comparing the wavefunctions of the first (blue dashed line) and second (red dashed-dot line) on-site energy eigenstates for $V_0/E_{R_+} \simeq 6$. The first gap becomes asymptotically equal to the potential shift of the two sites adjacent to the one with the lowest energy.
The reduction of the second gap is instead due to the negligible energy difference between the antisymmetric and symmetric states of the second (red dashed-dot line) and third band (green dot line) respectively, as shown in the inset b)

second energy gap reaches a maximum when it is of the same order of J, and then goes to zero with increasing values of the lattice depth is due to negligible energy difference between the antisymmetric and symmetric states of the second and third band respectively (see inset b in 1.10).
The fact that, for the BNSL in this regime, the energy gap goes like δ without the need for an additional external potential is what makes it truly appealing for experiments aiming to have highly confined atomic samples in one direction. Indeed, if the effective potential picture of the BNSL still hold even for large depth V_0, then the longitudinal confinement of the atoms, as it happens for a standard lattice, would scale as $\sqrt{V_0}$, while now $\delta \propto V_0$, Fig1.11.
This demonstrates that, at high depths, BNSLs are preferable in comparison to equal spacing single lattices, in particular in applications where arrays of atoms at high temperature are used (for example for quantum computation [55, 56]) or where strong spatial confinement is required [24, 57].
This linear scaling of the energy gap as a function of the lattice depth occurs until δ becomes equal to $\hbar\omega$, with ω the single site trapping frequency.
For deeper lattices $\delta = \hbar\omega = \sqrt{V_0/E_{R_+}^{1,2}}$ and the wave-function completely localizes in the site with minimum energy, the one at the bottom of the BNSL envelop.

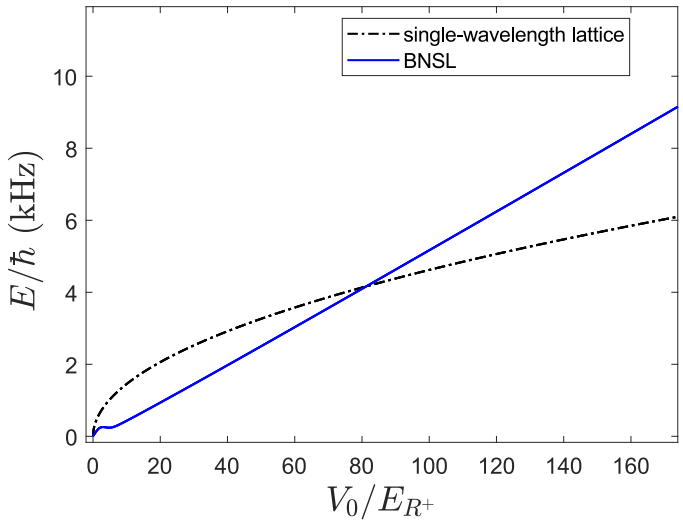

Figure 1.11: Amplitude of the first energy gap of a single wavelength lattice with periodicity d_- and of a BNSL with the same effective periodicity. The first one shows the usual square root scaling in the tight binding regime and the second one exhibits the peculiar linear behaviour as a function of V_0. For $V_0 > 80 E_{R_+}$ the BNSL surpasses the single lattice providing a larger gap for the same depth.

So far we have deliberately omitted the role of the phases ϕ_1 and ϕ_2 of the two lattices which make the BNSL. As one can deduce from 1.49 for different values of $\phi = \phi_1 + \phi_2$, the fast spatial modulation of the BNSL potential is spatially shifted with respect to the slowly varying envelope by an amount proportional to ϕ itself.
It's worth to report the case of $\phi = \pi/2$ characterized by two equal absolute potential minima equally displaced with respect to the minimum of the BNSL envelope, Fig. 1.12.
In this case the first energy gap of the BNSL is the one that, after reached a maximum, goes to zero with increasing values of the lattice depth. Like in a balanced double well potential, the first two eigenstates becomes the two degenerate symmetric and antisymmetric wavefunctions for large potential barrier separating the two spatial modes.
It is interesting to note that in the low depth regime the spectrum of the BNSL doesn't depend on ϕ, while it is crucial to define its behaviour in the large intensity limit. The perturbative approximation loses all the info about the phase of the fast spatial modulation, i.e. $\phi_1 + \phi_2$, while turns out to be again relevant in the large depth regime, as explained above.
To conclude in Fig.1.13 are showed the eigenvalues of the first three excited states of a BNSL double well potential as in Fig. 1.9, in the large depth limit $V_0 = 5 E_{R_+}$.

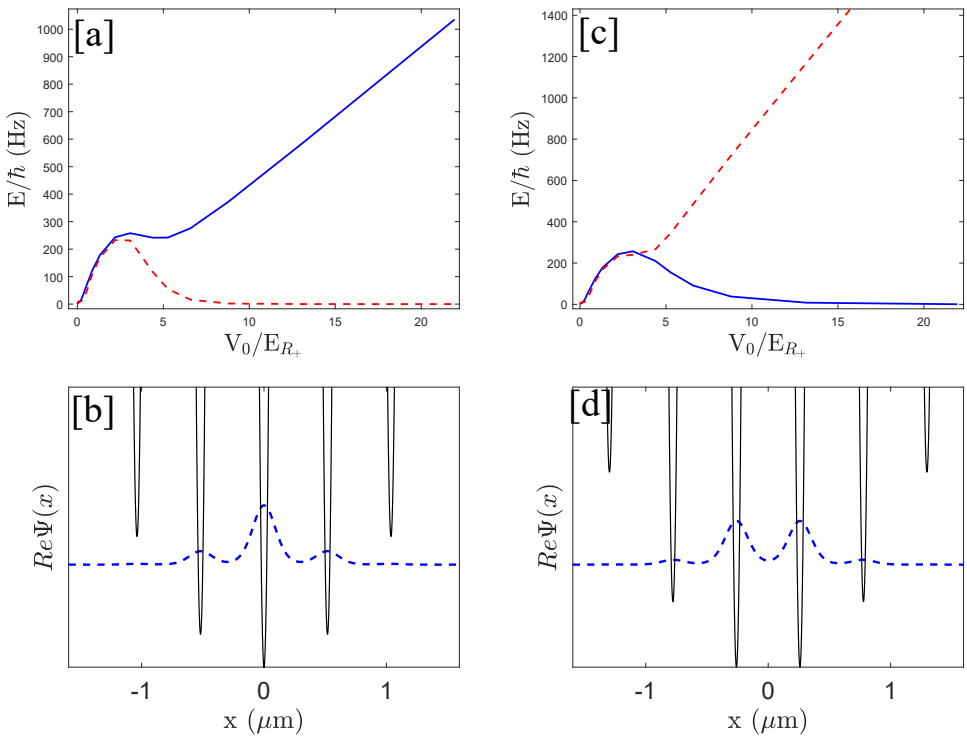

Figure 1.12: Theoretical calculations of the first (blue solid line) and the second (red dashed line) energy gaps of the BNSL with $d_- = 10\mu m$ and a) $\phi_1 = \phi_2 = 0$, c) $\phi_1 + \phi_2 = \pi/2$ as a function of V_0. In b) the wavefunctions of the first (blue dashed line) on-site energy eigenstates for $\phi_1 = \phi_2 = 0$ and d) for $\phi_1 + \phi_2 = \pi/2$.
As one can notice, the spectrum of the BNSL doesn't depend on ϕ up to $V_0 \geq 3E_{R_+}$

1.4 Kapitza Dirac diffraction with a Beat-Note Superlattice

BNSL in Eq.1.47 can be exploit to perform Kapitza Dirac scattering pulses to split the original condensate in momentum components finely spaced, $p=\pm j2\hbar k_-$, with $j \in \mathbb{N}$. This has already been used to perform multi-mode interferometry on a trapped condensate with time-pulsed lattices, the so-called Kapitza-Dirac interferometry, as it will be shown in chap.4.
In such work small momentum component generated by KD diffraction are essential to limit the region of the trapping potential explored by the atoms. This is possible since in the perturbation regime, $V_{1(2)} < E_{R_{1(2)}}$, BNSL can be described by an effective periodic potential with momentum k_-, as explained in chap.1.3. Beyond the effective potential approximation, the KD pulses diffract atoms also at momentum components associated with the two fundamental optical lattices, i.e., at integer multiples of $2\hbar k_{1(2)}$, and the atoms of these components are effectively lost for the purpose of the interferometer due to their large momenta.
To understand why, in the perturbative regime during KD diffraction, the population in the large momenta components is not so relevant, we can describe the short atom-light interaction with quasi-stationary perturbation theory (a constant potential which is turned on for a time t) as it is described in many introductory quantum mechanics books [58].
In par.1.3.2 we mentioned that BNSL effective potential is a consequence of a a four photon process. On the other hand, the large momenta components in KD scattering are generated by a two photon transition, where a photon of momentum k_1 (or k_2) is absorbed and one of momentum k_1 (k_2) is emitted.
So we have to compare the strength of this two process. At time t=0 we suppose the system is in the state of zero momentum $|p = 0\rangle$, which is the lowest eigenstate of the initial

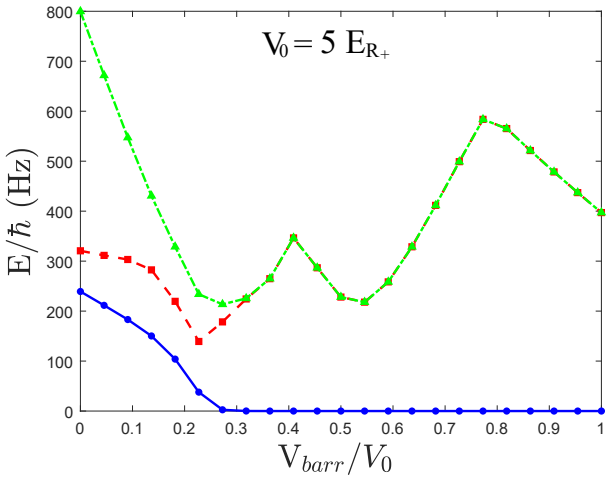

Figure 1.13: Eigenvalues in Hz of the first three excited eigenstates as function of barrier depth V_{barr} =V_3 for V_0 =5 E_{R_+}. The eigenvalue of the ground state has been subtracted from the other as common offset. Blue-dot represent then the tunneling energy of the double well system made by $V_B^{1,2,3} = \sum_i V_i \sin(k_i x + \phi_i)^2$, while blue continuos line is the effective potential in Eq. 1.59.
Red square and green triangles are the eigenvalues of the second and third excited state, while red dashed line and green dashed-dot line are the eigenvalues for the correspondent states of the effective potential..

unperturbed Hamiltonian H_0 (zero energy reference). When a small perturbation is turned on for a time t, the wavefunction $|\Psi(t)\rangle$ of the perturbed system can be still decomposed on the basis of eigenstate $|p\rangle$ of H_0, $|\Psi(t)\rangle = \sum_p c_p(t) e^{iE_p t/\hbar}|p\rangle$. It turns out that, applying the Method of variation of constants, stopping at the second perturbative order, and neglecting all terms proportional to time t since we are in a short pulse regime, we get

$$\begin{aligned}|\Psi(t)\rangle = |0\rangle &+ \sum_{p\neq 0} \frac{\langle p|V_B^{1,2}|0\rangle}{E_p}\left(e^{-\frac{iE_p t}{\hbar}} - 1\right)|p\rangle + \\ &+ \sum_{p\neq 0}\sum_{m\neq 0} \frac{\langle p|V_B^{1,2}|m\rangle\langle m|V_B^{1,2}|0\rangle}{E_m E_p}\left(1 - e^{-\frac{iE_p t}{\hbar}}\right)|p\rangle + \\ &+ \sum_{p\neq 0}\sum_{m\neq 0} \frac{\langle p|V_B^{1,2}|m\rangle\langle m|V_B^{1,2}|0\rangle}{E_m(E_p - E_m)}\left(e^{-\frac{iE_p t}{\hbar}} - e^{-\frac{iE_m t}{\hbar}}\right)|p\rangle + \\ &+ \sum_{p\neq 0} \frac{\langle p|V_B^{1,2}|0\rangle\langle 0|V_B^{1,2}|0\rangle}{E_p^2}\left(1 - e^{-\frac{iE_p t}{\hbar}}\right)|p\rangle\end{aligned} \tag{1.61}$$

where E_p is the recoil energy of a particle in momentum state $|p\rangle$. Making explicit the Fourier components of our BNSL we get
$V_B^{1,2} = \frac{V_0}{4}\left(2 + e^{i2\hbar k_1} + e^{-i2\hbar k_1}\right) + \frac{V_0}{4}\left(2 + e^{i2\hbar k_2} + e^{-i2\hbar k_2}\right)$,
so this potential can only couple momentum states $\pm 2\hbar k_{1,2}$. The state we are looking at is $|p = \pm 2\hbar k_-\rangle$, so as expected it can not be described by the second term in Eq. 1.61, which represents two photon transition to momentum state $\pm 2\hbar k_{1,2}$. For the same reasons also the last term in Eq. 1.61 is not useful. Third and fourth terms in Eq. 1.61 can describe the transition to state $|p = \pm 2\hbar k_-\rangle$, but we notice that in such terms the states $|m\rangle \equiv |\pm 2\hbar k_{1,2}\rangle$, so $E_m \gg E_p$. Thus, we can safely say that the probability amplitude which describes the four photon process $|0\rangle \rightarrow |p = \pm 2\hbar k_-\rangle$ is that of the third term of Eq. 1.61

$$\frac{\langle p|V_B^{1,2}|m\rangle\langle m|V_B^{1,2}|0\rangle}{E_m E_p} \propto \frac{V_0^2}{E_{R_{1,2}} E_{R_-}} = \frac{V_0^2 n^2}{E_{R_{1,2}}^2} \tag{1.62}$$

comparing this to that of second term in Eq. 1.61, which is $\propto V_0/E_{R_{1,2}}$, we understand that between the probability amplitude of the four photon process and that of the two photon process there is a factor $(V_0 n^2/E_{R_{1,2}})$. Even in perturbative regime of the BNSL description where $V_0 < E_{R_{1,2}}$, if $n \gg 1$ (for us n=20) the four photon process will be favourable.
To investigate the validity of BNSL description in scattering regime, I'll proceed with numerical simulations of KD diffraction by a BNSL.
First of all I compare the momentum distributions obtained after a KD pulse with the BNSL in 1.47 and with the effective potential in 1.52, see Fig. 1.14.
Note, in this simulation the wavelengths of the BNSL fulfil $(n+1)\lambda_1 = (n-1)\lambda_2$ with n=20 and $\lambda_1 = 1.013\mu$m, which gives an effective 5 μm spacing lattice.

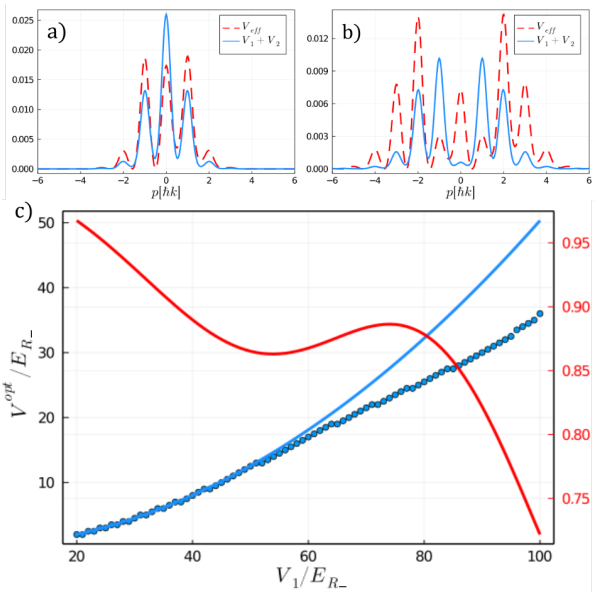

Figure 1.14: In the upper panel we compare the momentum distribution after a single KD pulse of the BNSL and of the effective potential for two different values of $V_1 = V_2 =:$ (a) $80E_{R_-}$, (b) $120\ E_{R_-}$. In (c) we report the numerically calculated "optimal" depths (blue points) compared with the perturbative depth of equation 1.52 (blue line), with the corresponding fidelity (red line, right axis)

As expected the approximation of the BNSL with the perturbative effective potential gets worse as we increase the BNSL amplitude. To quantify this aspect, in Fig. 1.14c I show the "optimal depth" V^{opt} of the effective potential V_{eff} as function of BNSL depth V_1=V_2. V^{opt} is calculated such that the fidelity $|\langle\Psi_{eff}|\Psi_{BNSL}\rangle|^2$ is maximum, where Ψ_{eff} and Ψ_{BNSL} are respectively the wavefunction in momentum space at the end of the first KD pulse τ=80μs for the effective and BNSL potential. We can see that the depth of the effective potential described by perturbative approximation and the one with depth equal to V^{opt} start to deviate at V_1=50 E_{R_-}, and that the fidelity drops below 0.9 for $V_1 \sim 40E_{R_-}$.
In the measurements shown in chap. 4 the BNSL depth was set to $V_1 = V_2 = 90\ E_{R_-}$, i.e. in a region where the perturbative expression is no longer valid. In order to confirm that the long wavelength approximation is still valid, we investigate numerically the population of the diffracted orders as a function of the length of the pulse Δt_{KD}.
In Fig. 1.15 I report the population of the first three diffracted orders and we compare them with the square modulus of the Bessel function $|\mathcal{J}_n(\frac{\Delta t_{KD} V^{opt}}{2\hbar})|^2$ with n=0,±1, as described in par. 1.1.5. We observe a very good agreement, except for residual little deviations that

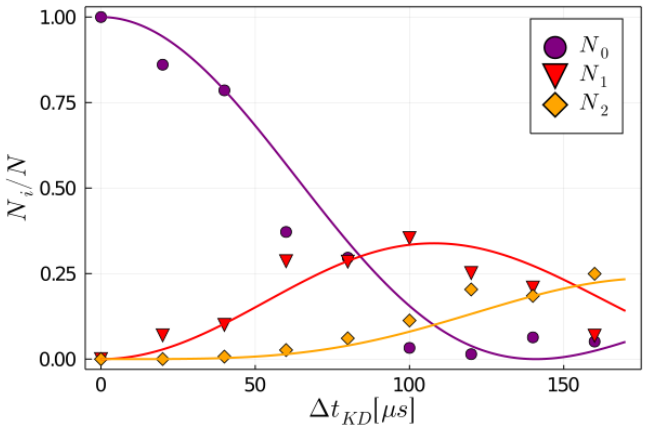

Figure 1.15: Numerical atomic fractional populations in the first three momentum components as a function of the length of the pulse for the BNSL with $V_1 = V_2 = 90E_{R\_}$ used in the experiment. The solid lines represent the theoretical prediction represented by the square module of Bessel function $|\mathcal{J}_n(\frac{\Delta t_{KD} V^{opt}}{2\hbar})|^2$, with n=0,±1.

are mainly due to the diffracted atoms also at the large momentum components associated with the two fundamental optical lattices. In Fig. 1.16 we show examples of the momentum

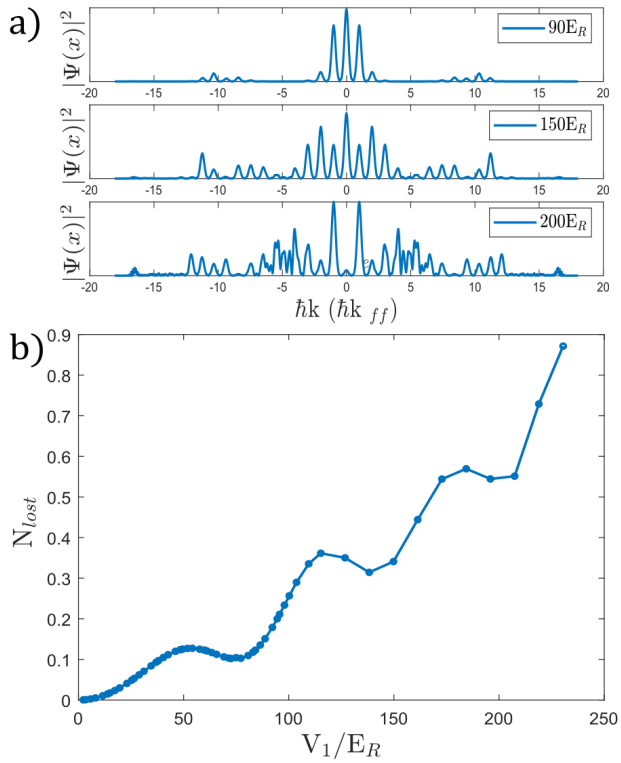

Figure 1.16: (a) Momentum distribution after a single KD pulse of the BNSL for different values of $V_1 = V_2$, i.e. 90 $E_{R\_}$ (used in the experiment, see chap.1.4), 150 $E_{R\_}$, and 200 $E_{R\_}$. Both small and large momentum components are displayed, in order to show how the diffraction pattern changes as function of V_1. (b) Fraction of atoms N_{lost} diffracted at momenta larger than the fourth-order component, as a function of V1.

distribution after a single KD pulse of the BNSL for increasing values of $V_1 = V_2$, together with an estimation of the fraction of atoms diffracted at large momentum components N_{lost}

as function of V_1. To evaluate the latter, we consider as "lost" the atoms with momentum $|p|>4\hbar k_-$, although as I will explain in chap.4 we have to restrict to $|p|<2$ in the experiment.

Chapter 2

Experimental Apparatus

In this chapter I describe our experimental platform for the realization of a Bose Einstein condensate trapped in a BNSL. Everything about the apparatus to produce and detect BECs of ^{39}K with tunable interactions, is part of the former group members' work in the past years, and more details can be found in their theses and publications [59, 60, 61].
In the first section I describe briefly the main parts of the experimental setup. Then I focus the attention on the new laser system used to produce the optical lattices I need for the BNSL. After a brief introduction to the theory of the Pound-Drevel-Hall method, I describe in more details the characteristic of the optical cavity and the electronic system that I have assembled in order to lock more than one frequency to the same reference. Finally, I give an estimation of the frequency noise affecting the locked lasers by mean of a second reference cavity.

2.1 Experimental platform

In this paragraph I will focus on the experimental apparatus for the realization of the Beat Note Superlattice (see 1.3.3), for its implementation in two works [25, 28], and for the creation of the array of Double well potentials (see 1.3.3), exploited to realize a trapped atom gradiometer.
Briefly, in a first vacuum chamber a 2D magneto-optic trap (2D-MOT) captures part of the gas of atoms released by a potassium solid sample, slowing the atoms along two orthogonal directions. This step produces an atomic beam that is collected from a 3D MOT in a second cell, where the atoms are cooled down to sub-doppler temperatures.
Then the atomic cloud is confined in a magnetic trap mounted on a mechanical translational stage and brought to the last vacuum chamber characterized by the lowest pressure and a wide optical access, where Bose Einstein condensation is accomplished by means of evaporative cooling into an optical dipole trap potential. In particular, once the atoms reach the science chamber (Fig 2.1), they are loaded in a crossed dipole trap provided by two tightly focused red detuned infra-red beams with a wavelength around 1060 nm. The first one, the 'radial beam', is provided by a Mephisto MOPA laser (Coherent) while the second one by an IPG photonics ytterbium fiber laser (YLR-100-LP-AC), which propagates in the horizontal plane with an angle of $\pi/4$ with respect to the radial beam.
Two pairs of coils are then used to generate the magnetic fields necessary for the experiment, i.e a uniform magnetic field to change the two body interaction via a broad magnetic Feshbach resonance at 400 G [61, 62, 63], and a magnetic field gradient to compensate for gravity.
The evaporative cooling consists in a selective loss of the most energetic atoms and a subsequent re-thermalization of the system at lower temperatures through collisions. However, since the ^{39}K background scattering length is negative, it exists for low energies a minimum value of the cross section (Ramsauer Townsend minimum). Once you reached such limit, the

system can no longer thermalize, so at a given temperature the evaporative cooling becomes inefficient. To solve this problem we change the scattering length exploiting Fashback resonances. We manage to produce with this system ensembles of up to $10^4 - 10^5$ atoms almost purely condensed.

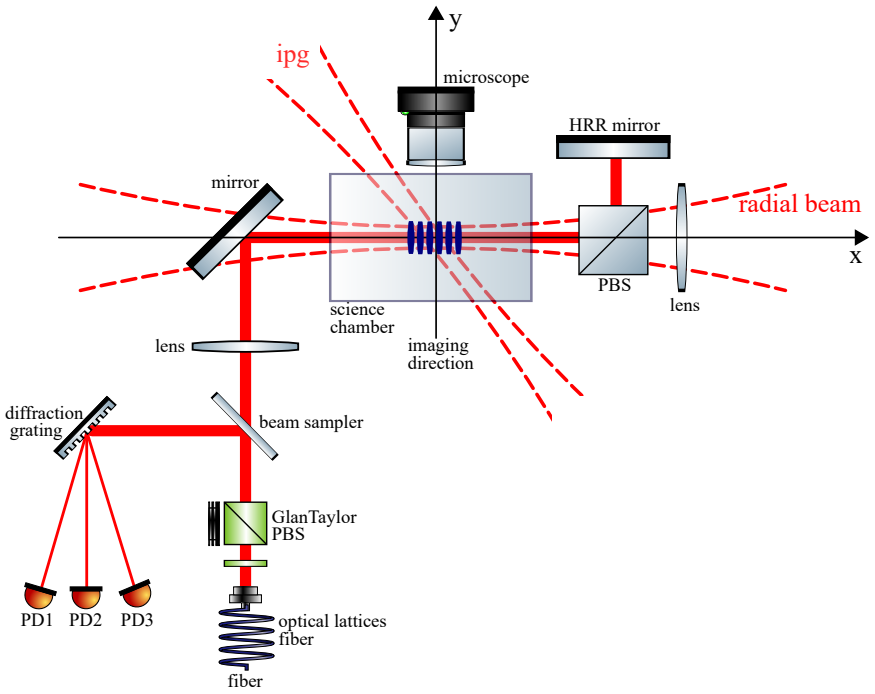

Figure 2.1: Sketch of the laser beams in the science chamber (from above). The radial beam and the lattice beams have different polarizations and they are mixed on a BS cube. After the fiber a part of the lattice beam is sent to a diffraction grating in order to separate the two wavelengths and measure the intensity of each beam on three photodiodes.

The three lasers exploited to produce the BNSLs (let's refer to them as 'lattice lasers') propagate along the same axis of the radial beam (the 'longitudinal direction', x-axis). After the evaporative cooling the IPG can be switched off adiabatically and a third infra-red beam which propagates perpendicularly to the IPG-radial plane is then turn on to give the longitudinal confinement. This beam, the 'vertical' beam (Mephisto MOPA laser), is mainly used to decide how many BNSL sites must be loaded with the condensate. After the loading, the vertical beam is switched off too, since the longitudinal confinement is now given by the BNSL, while the radial beam remains on during all the experiment in order to provide the confinement in the radial direction ($\omega_{y,z} \approx 2\pi \times 200$Hz).
All the lattice lasers come out from the same fiber, sharing the same spatial profile and the same optical path. The polarization is well defined by a Glan Taylor polarizer cube (model CGTP,broadband 350-2300nm,LAMBDA) placed at the output of the fiber. After they have passed through the cell, they are reflected by a beam splitter-cube where they are superimposed with the radial beam, that has an opposite polarization. Finally, they are simply retro-reflected with an HRR mirror and sent back into the fiber. At the output of the fiber, a fraction of the light is sent to a diffraction grating in order to separate the three wavelengths

and measure the intensity of each beam separately on two photodiodes. The three signals are sent to different PID (Proportional-Integrator-Derivative controller) controllers to monitor and stabilize the intensity.

2.2 Optical lattices laser setup

Fig 2.2 shows the laser setup for the production and the control of the frequency and intensity of the three lasers at 1064 nm, 1013 nm and 1120 nm. The light at 1064 nm is provided by a high power Mephisto MOPA (MM) infrared laser (1064,439 nm, vacuum) and the lights at 1013 nm (1013,751 nm, vacuum) and 1120 nm (1120,5xx nm, vacuum) are provided by two Toptica TA PRO diode laser with a maximum power of 2W.

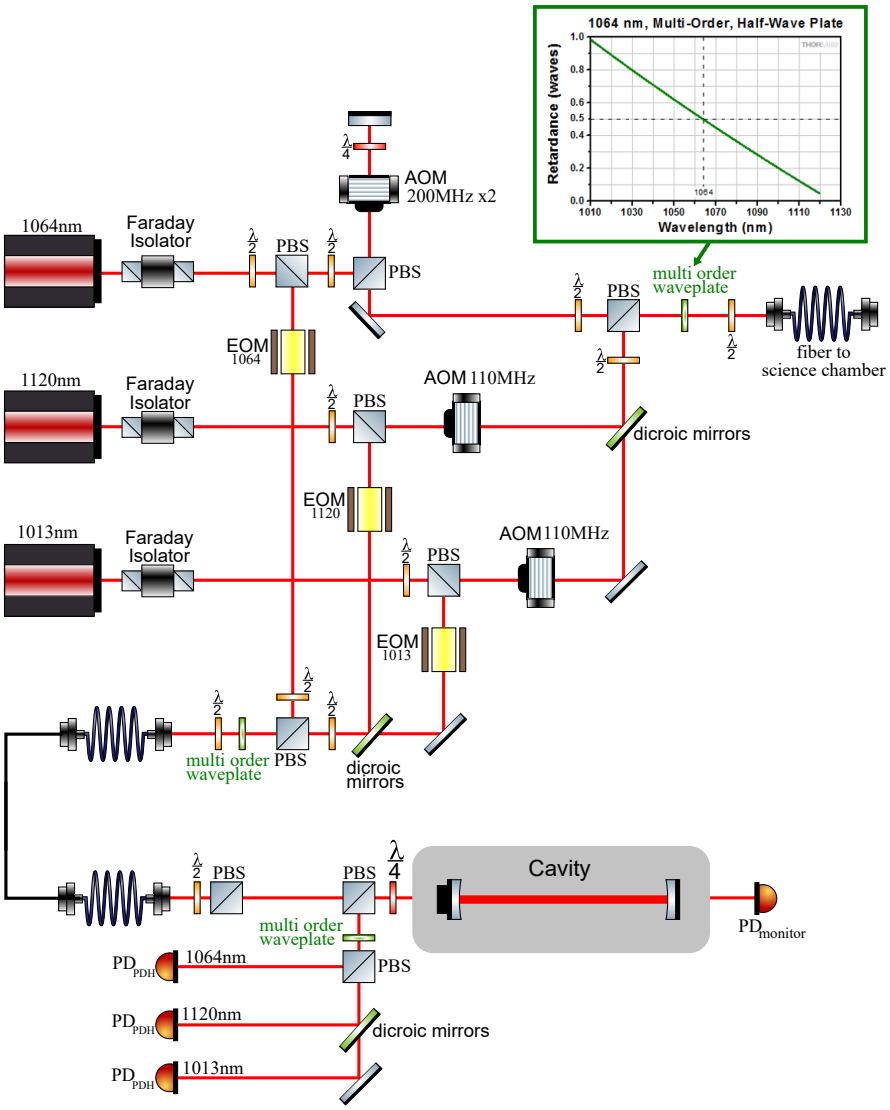

Figure 2.2: Scheme of the laser setup to produce and control the two lights at 1064 nm, 1013 nm and 1120 nm. In the inset above I show the retardance as a function of the wavelength of the multi-order waveplate used to obtain the same polarization at the entrance of the fiber.

After optical isolators a fraction of light of all beams is sent to electro-optical modulators (EOMs) and then they are combined with a beam splitter in a fiber that brings the light to an optical cavity exploited for lasers frequency locking. The rest of the light is sent to acusto-optical modulators (AOMs) that, together with the photodiodes in Fig. 2.1 and PID

controllers, allow to stabilize the intensity. For one of the two beams we use a double passage AOM (model 3200-1113, Crystal Technology) in order to have the possibility to tune dynamically the frequency of the laser in a wider range of about 160 MHz, while the other two are set in a single passage configuration (model 3110-197, Crystal Technology, driven at 110 MHz). After the AOMs, the three laser beams are mixed on a polarizing beam splitter cube (PBS) and sent together in the same fiber that brings the light to the atoms. Before this fiber, since the three beams have different polarizations, on the Glan Taylor polarizer at the exit (Fig. 2.1) it is not possible to have all the power transmitted for all of the beams at the same time. In order to avoid power losses, we have decided to use a multi-order half-lambda waveplate by Thorlabs (model WPMHOS-1064, THORLABS), whose retardance as a function of the wavelength is shown in the inset of Fig. 2.1. It allows to rotate the polarization of the 1064 light, while it left the polarizations of the others unchanged. In this way we can send the three beams inside the fiber with the same polarization and have all the power available for all of them.

2.3 Tunable interactions

An important tool in our experiment is the possibility to control the interatomic scattering length via a magnetic Feshbach resonance. The two-body scattering length depends on the magnitude of the magnetic field by the relation $\mathrm{a}_s = \mathrm{a}_{bg}\left(1 - \frac{\Delta \mathrm{B}}{\mathrm{B}-\mathrm{B}_0}\right)$.
The s-wave scattering length a_s, that defines the low energy limit (limit for momentum $\mathrm{k}\to 0$) for the elastic scattering cross-section $\sigma = 8\pi \mathrm{a}_s$, allows to describe interaction in a simple picture, where the particular features of the interatomic potential can be neglected in favour of an effective pseudo-potential $\mathrm{V}_{\mathrm{int}}(\vec{\mathrm{r}}, \vec{\mathrm{r}}') \simeq \frac{4\pi\hbar^2 \mathrm{a}_s}{m_a}\delta(\vec{\mathrm{r}} - \vec{\mathrm{r}}')$. The sign of a_s determines if the effective potential is attractive ($\mathrm{a}_s < 0$) or repulsive ($\mathrm{a}_s > 0$). This approximation relies on physical assumptions usually valid in case of cold bosons, namely low collisional energy and the symmetry of the atomic wavefunction for identical particle exchange.

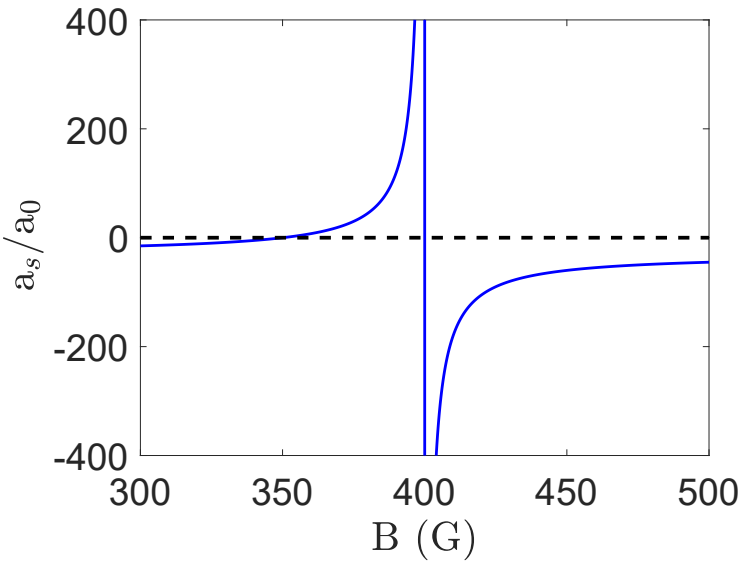

Figure 2.3: Value of the two-body scattering length a_s in Bohr radia versus the magnitude of magnetic field B in Gauss for the state $|\mathrm{F} = 1, \mathrm{M_F} = +1\rangle$ near the resonance at 400G

In particular, in the case of ^{39}K, there is a broad resonance for the state $|\mathrm{F} = 1, \mathrm{M_F} = +1\rangle$

(the atomic state we condense), near a value of B_0=400 G, Fig. 2.3. The width of this resonance is ΔB=50 G and the zero crossing point is at 350 G. Around this point the slope is $0.6a_0$/G so, if the magnetic field is stable enough, it is possible to change or cancel the value of the scattering length very precisely.

2.4 Imaging System

In our experiment we detect the distribution of the atoms and count them via absorption imaging, exploiting the wide optical access of the science chamber. This technique consists into shining the atoms with a low intensity I_{in} (i.e. less then saturation intensity I_s) probe resonant light beam of wavelength λ. Atoms absorb part of the incoming signal proportionally to the local column density $n_{x,y}$ of the atomic cloud according to the Lambert-Beer Law $I_{out}/I_{in}=e^{-\sigma n_{x,y}}$, where $\sigma = \frac{3\lambda^2}{2\pi}\frac{1}{1+\frac{I}{I_{sat}}+4\frac{\delta^2}{\Gamma^2}}$ is the scattering cross-section for the imaging light, Γ is the natural width of the atomic transition and $\delta = \omega - \omega_0$ is the detuning between the frequency of the laser and the frequency of the transition. The presence of atoms is then recorded as a negative image in the probe beam intensity profile, which is sent to the measuring device.

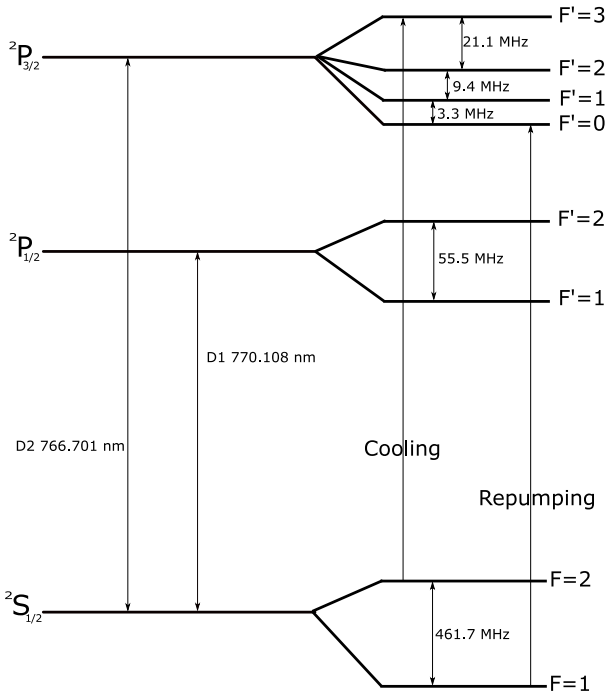

Figure 2.4: Optical transitions of the D1 and D2 lines of 39K.

To measure the ratio I/I_0 for each point it would be sufficient to acquire two images, one of the imaging light without the atoms and one of the light with the atoms, and calculate the ratio for each pixel. To increase the signal-to-noise ratio we acquire a third image without imaging light and without atoms, and subtract it from both images before performing the ratio.
Imaging direction is in the horizontal plane xy (see Fig. 2.1) and, to collect images, we exploit a microscope with short focal lens (objective, N.A 0.6) and a long focal imaging lens, to get a magnification of $M \sim 30$. An Andor Ikon-M digital camera acquires magnified images, whose micrometers to pixel conversion factor is $\alpha = 2.4 \pm 0.2 px/\mu m$.

For the ^{39}K in the state $|\mathrm{F}=1,\mathrm{M_F}=+1\rangle$ we exploit the D2 line (see Fig. 2.4), with $\Gamma/2\pi \simeq 6$MHz. The imaging procedure is performed with negligible magnetic field and using a light resonant with the transition F=2→F'=3 (named cooling light in Fig. 2.4) with a polarization σ_+. Since the atoms are in the state $|\mathrm{F}=1,\mathrm{M_F}=+1\rangle$, we need an initial pulse of light resonant with the transition F=1→F'=2 (named repumper light), in order to allow a decay in the state F=2. However, since the states F'=3 and F'=2 are close (about 3.6 Γ) there is a non zero probability that the imaging light induces the transition F=2→F'= 2 with consequent losses of atoms due to decay F'=2→F'=1. To avoid this, we need this repumping laser on during the whole imaging procedure

2.5 Laser frequency stabilization

Let's consider the beat-note superlattice made by two optical lattices (see chap. 1.3). The relative phase of the two lattices determines the position of the maxima and the minima of the resulting BNSL, so controlling such parameter allow to translate the whole BNSL in space.
To quantify this, think about the system in Fig. 2.1 with the BNSL on. The atoms are loaded in a single site of the BNSL, about D∼25 cm from the retro-reflecting mirror. This means that, on a single standing wave, a frequency fluctuation $\Delta\nu$ will result in a additional phase

$$\Delta\phi = 2\mathrm{D}\frac{2\pi}{c}\Delta\nu \tag{2.1}$$

meaning that, for $\Delta\nu$ ∼300MHz, we'll have a complete sweep of the minima of the BNSL, and the atoms will experience the passage through maximum of the trapping potential.
Breaking down noise fluctuations on this critical parameter is then a fundamental task that must be carried out in order to exploit BNSLs as a tool to coherently manipulate atoms over large distances.
So, in order to increase the stability in relative frequency fluctuations I have realized an experimental setup to lock all the frequencies to an external high finesse Fabry Perot cavity, exploiting a Pound-Drever-Hall technique.
Before going further on the PDH technique, I want to stress that the phase difference in the BNSL I'm referring to, the $\phi_{1,2} = \phi_1 - \phi_2$ term in expression 1.52, is the relative phase between the two standing waves in 1.47, and not between the two lasers, strongly relaxing the experimental requirements to minimize its fluctuations. In our setup the two possible sources of instabilities of $\phi_{1,2}$ are laser frequency fluctuations and instabilities of the retroreflecting mirror.

2.5.1 Optical cavity

The optical cavity we are currently using for the frequency locking (Fig2.5a) is made of INVAR (a material with a small thermal expansion coefficient) and the mirrors are in a hemispherical configuration (the input mirror is nearly flat, $\mathrm{R_1} \approx \infty$, and other one, $\mathrm{R_2} \simeq 30$ cm, is concave). Light can propagate through an optical cavity if half the wavelength λ is related to the cavity length L through the relation $\mathrm{n}_i\lambda/2 = 2\mathrm{L}$, where n_i is an integer. The optical cavity is then a filter whose transmission line (fundamental modes n_i) are separated in frequency by a fixed distance called Free Spectral Range (FSR), $\nu_{fsr} = \frac{c}{2\mathrm{L}}$ [64].
A piezoelectric transducer is placed behind the first mirror. Driving it with a triangle waveform of suitable frequency and amplitude it is possible change the cavity length L to scan over different resonance frequencies (otherwise, one can do the same thing scanning the frequency of the laser itself). The resultant spectra, measured by a photodiode that is placed behind

the cavity, is shown in Fig. 2.5b
Since we didn't build the cavity but we borrowed it from another experiment, I had to characterized it. The measured FSR is $\nu_{fsr} \simeq 1.09$ GHz, which correspond to L≃13.7 cm. Zooming on a single fundamental mode (Fig. 2.5d) we can measure the FWHM of the transmission peak, $\Delta_{FWHM} = 230$kHz, a quantity which is relate to the FSR by the finesse $f = \frac{FSR}{\Delta_{FWHM}}$, which is $f \approx 4800$.
To get info about the last quantity which define this cavity, the radius of curvature of the backside mirror R_2 we misalign slightly the cavity to measure the separation $\delta\nu$ between the transverse modes, which in figure Fig. 2.5c appear next to the fundamental ones. Such separation is related to R_2 by $\delta\nu = \frac{\nu_{fsr}}{\pi} \arccos\left(1 - \frac{L}{R_2}\right)$, and for our mirror is $R_2 \simeq 31.4$cm.

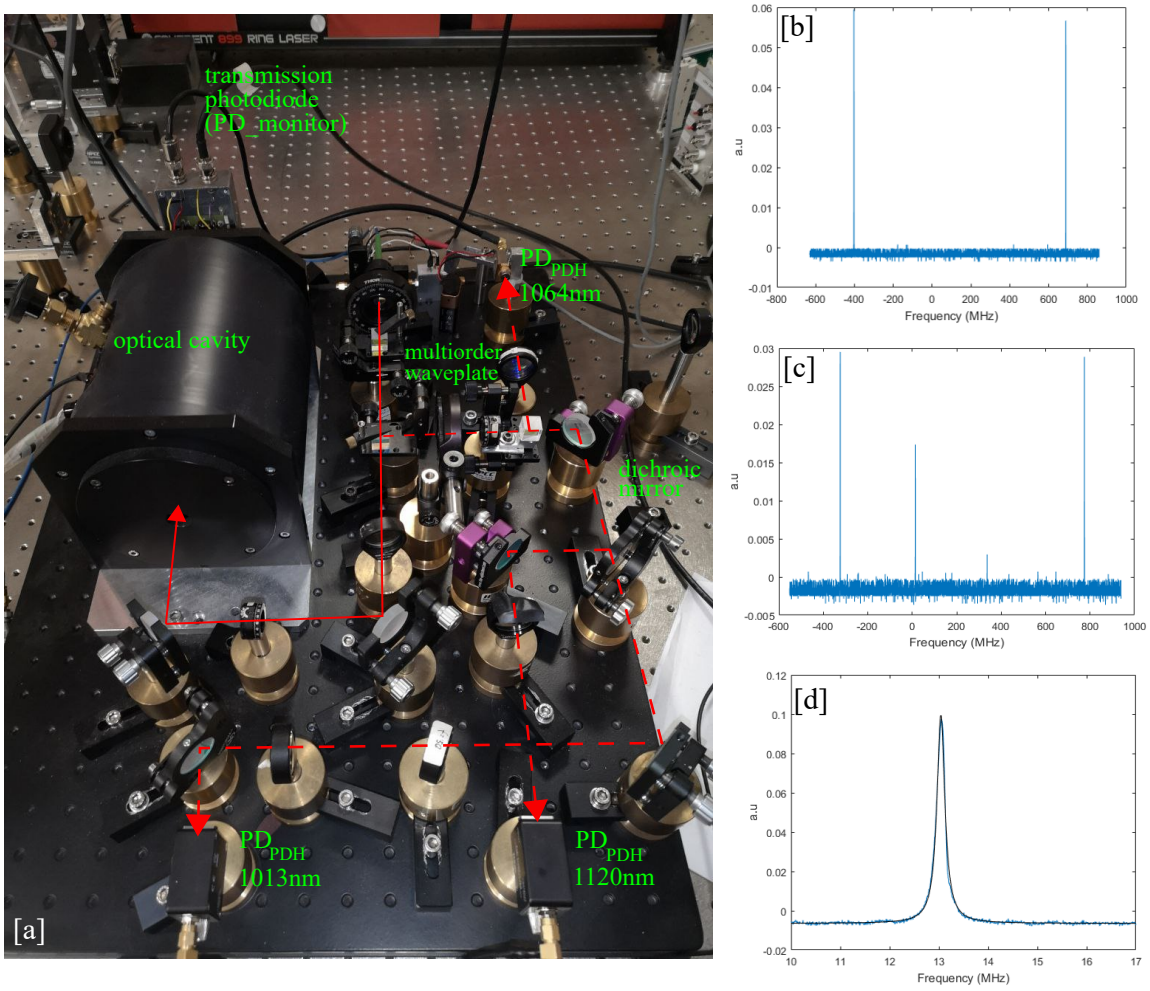

Figure 2.5: a) Picture of the cavity. Red thick line represents the beam incoming in the cavity, red dashed line is the reflected beam. b) A well aligned cavity shows very sharp fundamental modes. b) Higher order (transversal) modes appear when it is slightly misaligned. c) Zoom of the fundamental transmission peak

2.5.2 Pound-Drever-Hall locking

Single frequency locking
The frequency stabilization technique exploited in our experiment is based on the Pound-Drever-Hall (PDH) locking scheme [65, 66], which is shown schematically in the figure Fig. 2.6 for a single frequency (the one exploited for the lock of the 1064nm laser).

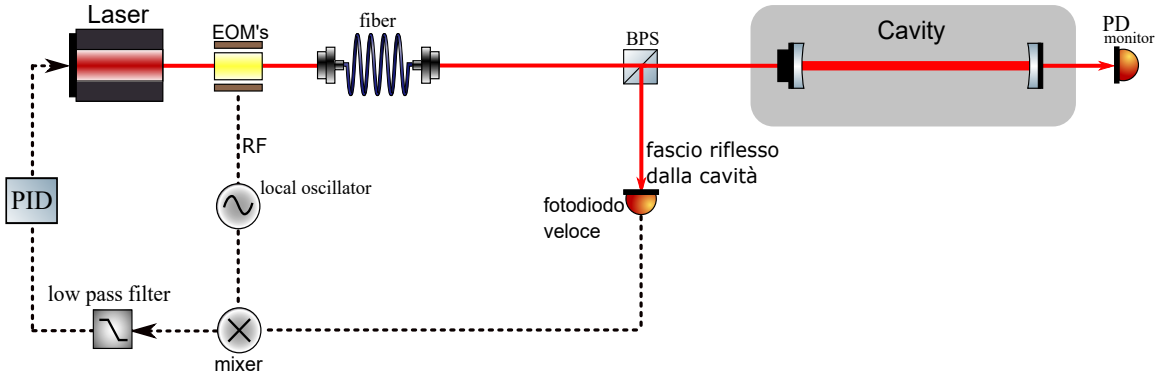

Figure 2.6: Schematic representation of PDH locking loop. Solid red line represents the optical paths and the black dashed line represents the path of the electronic signals.

The light incident on the cavity is first phase-modulated, usually by an EOM, so that the electric field is of the form

$$\mathrm{E}_{inc} = \mathrm{E}_0 e^{i(\omega_c \mathrm{t} + \beta \sin(\Omega \mathrm{t}))} \tag{2.2}$$

where E_0 is the amplitude of the incident field on the modulator, ω is the angular frequency of the incoming light, β is the modulation depth, and Ω is the angular frequency of the modulation. The effect of this modulation in the phase, at the first order in the amplitude β, is to generate three distinct frequency components, a carrier at $\omega = \omega_c$ and two sidebands $\omega = \omega_c \pm \Omega$. For the light at 1064 nm we use a free-space EOM by Thorlabs that has an RF bandwidth of 50 MHz, driven by $\Omega = 10.8$ MHz with 1V of amplitude. In Fig. 2.7 in blue it is shown signal recorder by the photodiode after the cavity.
For sufficiently large Ω, the sidebands are completely reflected when the carrier is near resonance. If also the carrier is not perfectly in resonance, a portion of it will reflect and generate an intensity modulation by interfering with the reflected sidebands at a frequency $\pm\Omega$. The amplitude of such modulation is proportional to the frequency difference between the carrier and the cavity resonance. To measure it, we collect the reflecting intensity on a fast photodiode (for the 1064 nm laser we use a PD G7096-03) and then we demodulate the output signal by a mixer driven with the same local oscillator at Ω.
The DC signal coming out from the mixer is the PDH error signal, which now can be sent to a servo amplifier (PID) to make the feedback signal. In the end, the feedback tells the driver laser how to change the output frequency ω_c in order to reduce the PDH error, and eventually locking the laser to the cavity. In Fig 2.7 an example of PDH error signal for the 1064nm laser.
The shape of the PDH error signal can be adjusted introducing a phase shift between the local oscillator and the signal from the photodetector. The error signal in Fig. 2.7 is anti-symmetric with respect to the resonance (zero level of the error signal), which means that it takes a positive value if it is above, or negative if it is below the such level. Therefore we can know which side resonance we are in, and correct accordingly. The slope of the error signal is a measure of the sensitivity of the error signal to fluctuations in the laser frequency or cavity length and it depends on the sidebands power, and it depends by the modulation depth β.
For the purpose of a good lock is to keep in mind that if the polarization of the light that enter in the EOM is not well parallel to the axis of the EOM crystal, a residual amplitude modulation (RAM) may occur [67], which can cause an uncontrolled spread of the laser linewidth due to intensity fluctuations. When this happen, not only the phase but also the polarization is modulated, and this modulation is translated to an intensity modulation by the cube just before the cavity. Since the frequency is the same as the phase modulation, the effect is the appearance of a floor in the signal after the mixer that does not depend on the frequency of the laser but that is proportional to the intensity of the laser. In order to

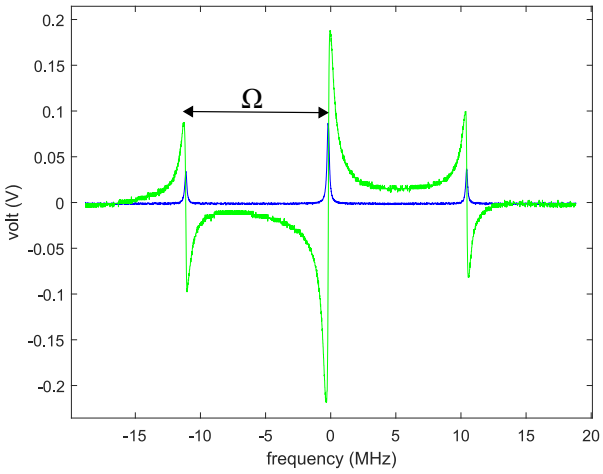

Figure 2.7: Blue thin line represents the signal on the photodiode after the cavity, green thick line is the correspondent Pound Drever Hall error signal for the 1064 nm laser.

minimize this effect we place a Glan Taylor polarizer before the EOM in order to clean very well the polarization.

Offset sideband locking

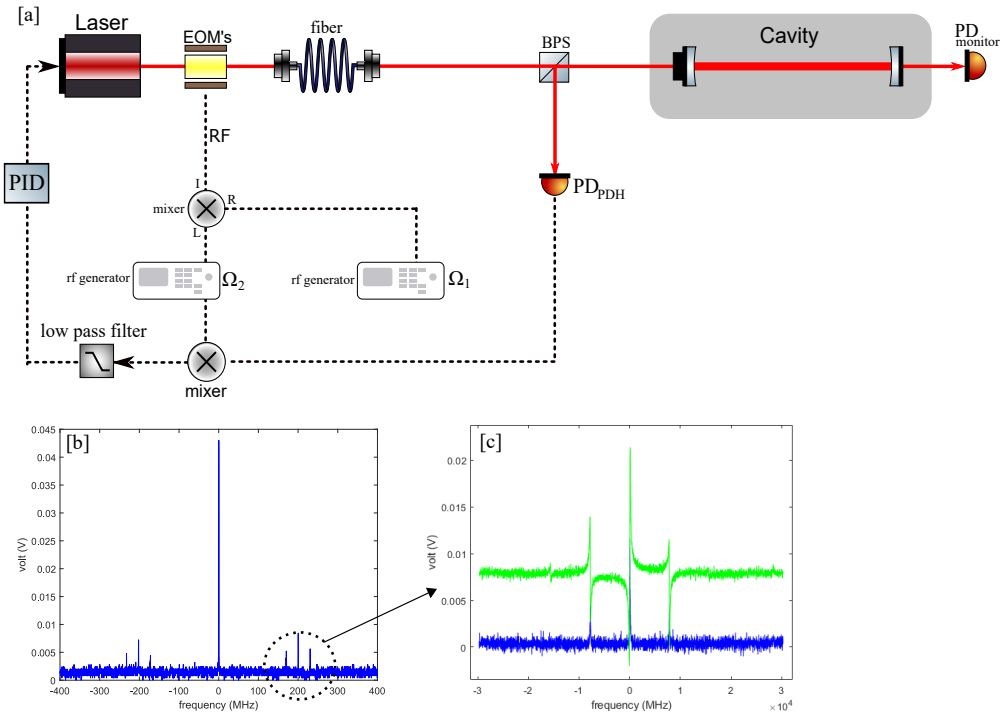

Figure 2.8: a) Schematic representation of PDH locking loop in dual-sideband configuration. b) Signal on he photodiode after the cavity which shows the sidebands and the sub-sidebands and c) Error signal after the mixer in the dual sidebands configuration for the 1013nm laser source.

The 1064 laser source, locked to the cavity, can be tuned by means of the double passage

AOM in Fig. 2.2, but the tunability range is lower then 200 MHz. For the other two laser source used in this work (the two Toptica TA-PRO laser at 1013nm and 1120nm) we used a slightly different technique, which instead allows to tune the laser frequency with respect to the cavity resonance inside the whole FSR. The technique is called offset sideband locking [68, 69], and in particular we use a dual-sideband configuration (DSB) modulating the beam at two distinct frequencies, one of which is adjustable (see Fig. 2.8a) . In this case, the electric field is

$$\mathrm{E_{inc}} = \mathrm{E_0} e^{i(\omega_c \mathrm{t} + \beta_1 \sin(\Omega_1 \mathrm{t}) + \beta_2 \sin(\Omega_2 \mathrm{t}))} \tag{2.3}$$

where $\Omega_{1,2}$ and $\beta_{1,2}$ are respectively frequencies and amplitudes of the modulations. The effect of this phase modulation is a carrier with angular frequency ω_c, sidebands with angular frequencies $\omega_c \pm \Omega_1$, sidebands with angular frequencies $\omega_c \pm \Omega_2$, and sub-sidebands at $\omega_c + \Omega_1 \pm \Omega_2$ and $\omega_c - \Omega_1 \pm \Omega_2$, Fig. 2.8b. The error signal is shown in Fig. 2.8 assuming $\Omega_1 > \Omega_2$ and $\beta_1 > \beta_2$ and it is relative to the part of the spectrum centred at $\omega_c + \omega_1$ with sidebands offset $\pm\Omega_2$. This scheme allows to place one of the $\omega_c \pm \Omega_1$ sidebands on resonance with the cavity and demodulate the reflected power with Ω_2. In this way it is possible to tune the frequency of the laser changing Ω_1.
The EOMs used to modulate the light at 1013nm and 1120nm are a fiber-integrated EOM by IXblue (NIR-MPX-LN-02), that has a RF bandwidth of the order of 2 GHz, it requires a low RF power to obtain a good modulation depth, and it is possible to drive it with more than one RF frequency. As shown in Fig. 2.8a for the 1013nm source the two frequencies Ω_1, Ω_2 are generated by two independent RF generators, the first tunable up to 2GHz and the second one fixed at 30 MH. The two signal are sent to a mixer whose output is then amplified and sent to the EOM. Part of Ω_2 is taken to demodulate the PDH signal from the fast photodetector. For the 1120 laser source we have Ω_1 tunable within the range 320-480MHz and Ω_2 fixed at 50 MHz.

2.5.3 Frequency noise estimation

By mean of an optical cavity similar to the one described above for the PDH frequency lock loop (lets call them respectively second and first cavity) it is possible to give an estimation of the residual frequency noise in the PDH error signal (this is true as long as there is no correlation in the noise affecting the two cavity). We manage to build the second cavity almost identical to the firs one, but unfortunately the mirror are different an it turns out it can not be used for the light at 1013 nm.
So, we start with a laser locked to the first reference cavity as described in the previous section. A portion of the light used in the first lock scheme is taken and sent to the second cavity. Changing the length of the second cavity by mean of a piezoelectric transducer I can find the resonance with the incoming light. I can observe the resonance sending the light transmitted by the cavity on a photodiode, and its output signal on a oscilloscope (a signal similar to that in Fig. 2.5).
Now, changing the piezo voltage to get close to the maximum of such signal means to be almost perfectly resonant with the incoming light. Anyway, to retrieve informations about the frequency noise level a better choice is drive the piezo such that the resonance is shifted by half of the cavity mode width. Basically, we are now at the centre of the slope of that signal instead of the maximum. At this "half point" a small fluctuation of the frequency of incoming light correspond a larger change in the intensity of transmitted signal (so, we are more sensitive). Moreover, at the centre of the slope intensity is, in a first approximation, linearly dependent on frequency, so I can convert from one to the other.
Thus, disconnecting the voltage signal which drives the piezo, but leaving the piezo charged, we can observe intensity (i.e. frequency) fluctuations as function of time, Fig. 2.9.

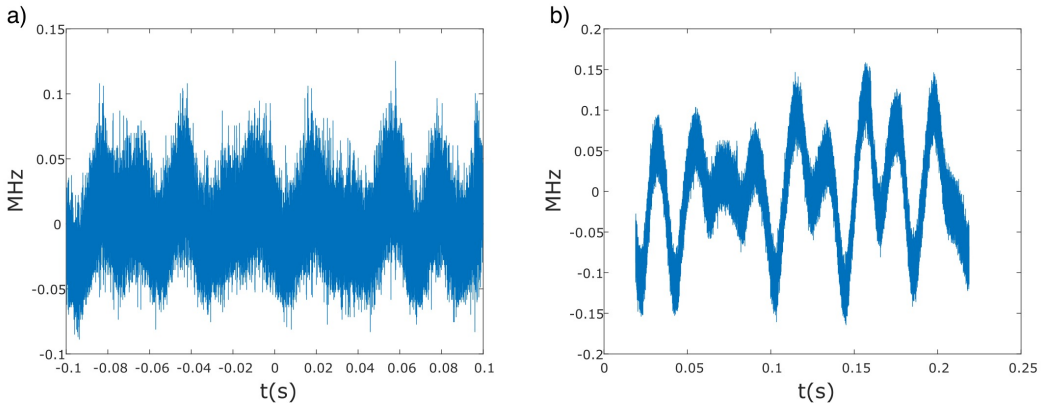

Figure 2.9: Frequency noise of the PDH error signal of a) light at 1064nm and b) at 1120 nm with a temporal window of 200 ms.

From the Fourier transform of signals in Fig. 2.9 we see that are present large low-frequency noise components between 20 and 100 Hz, probably due to electric noise (maybe some ground loop) Future optimizations of the locking system are clearly needed.

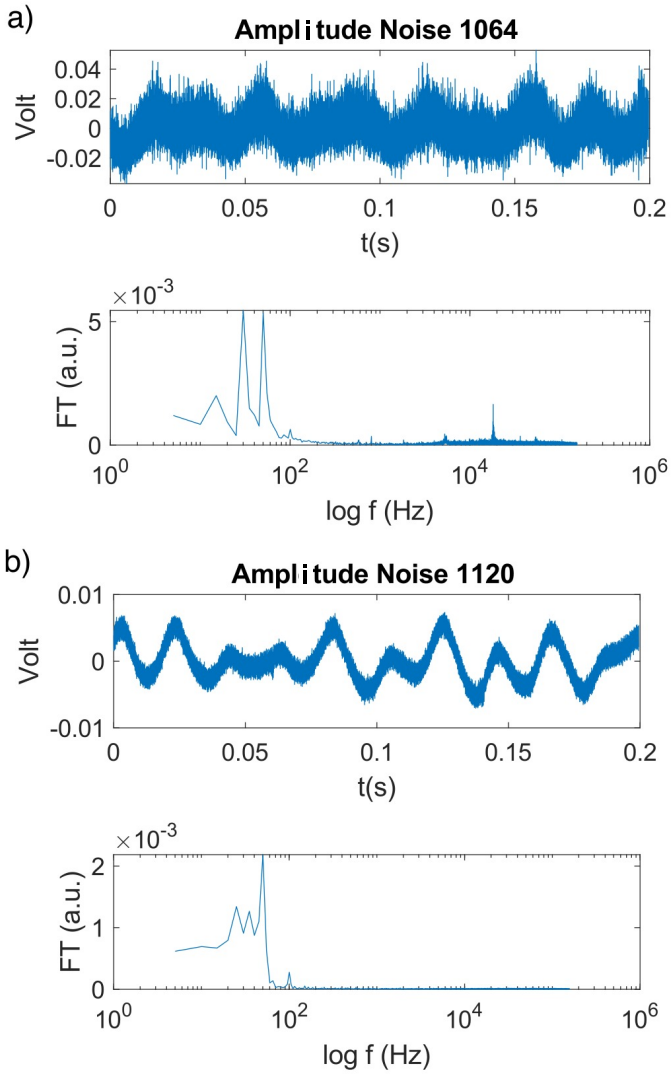

Figure 2.10: Spectrum of the frequency noise signal for a) light at 1064nm and b) at 1120 nm

2.6 Lattices calibration via Talbot pulses

Referring to par. 1.1.6, here I show same examples of calibrations of the three lattices by mean of Talbot pulses diffraction on the BEC. This is a technique I am currently studying to calibrate the depth of the three lattices individually, in a different (maybe more rigorous) way respect to what I have done so far (see par.3.1). It has not yet become standard practice.
1013 nm lattice $\rightarrow$ half Talbot time $T_{talbot}/2$ =25 μs
1064 nm lattice $\rightarrow$ half Talbot time $T_{talbot}/2$ =27 μs
1120 nm lattice $\rightarrow$ half Talbot time $T_{talbot}/2$ =30 μs
To realize the train of pulses I modulate the amplitude of each lattice switching on (for a time $T_{talbot}/2$) and off (for a time $T_{talbot}/2$) the AOMs placed on the respective optical path. In Fig. 2.11 are shown the relative population $(N_{-}1+N_{+}1)/N_{tot}$ transferred in order components ±1 (i.e. momenta $\pm2\hbar k_i$) as function of number of pulses N for three depths. The red curves on the plots are numerical simulation as the one shown in Fig. 1.2 for the three different lattices, which give us a range of $s=V/E_R$ on the estimation of depth by data point. Fitting data with quadratic approximation in Eq. 1.27 it is also possible, but we have to stay in the regime $V<<E_R$, which is not the case in these measurements.

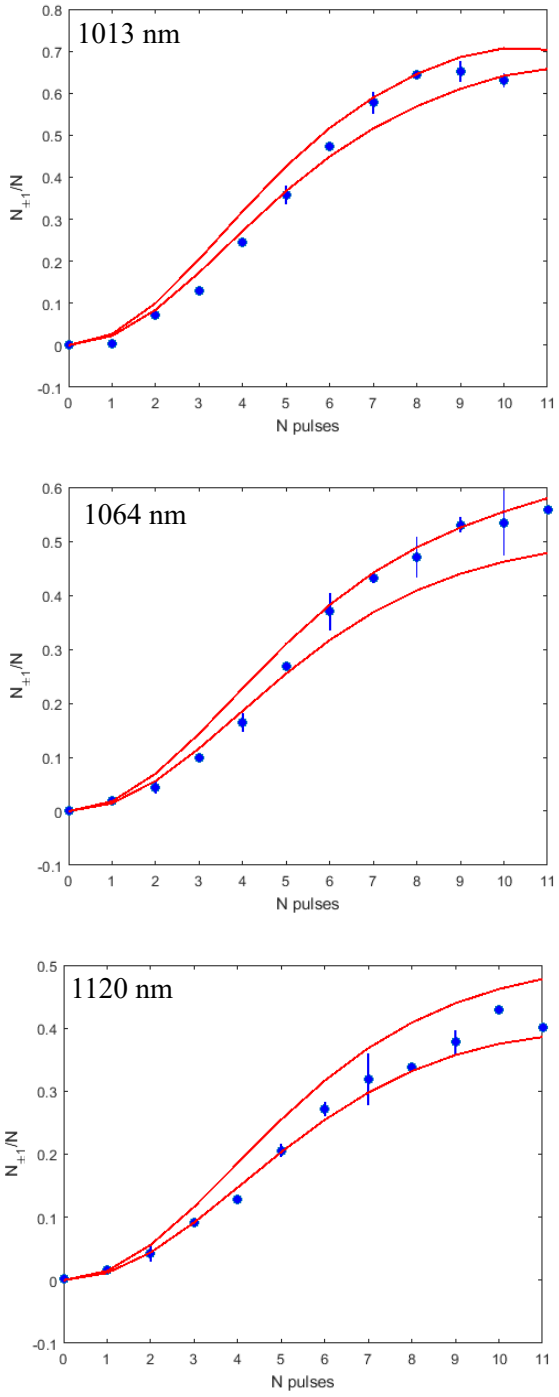

Figure 2.11: Diffracted population at fixed laser power and wavelength as function of number of pulses.The red curves on the plots are numerical simulation as the one shown in Fig. 1.2 for the three different lattices, which give us a range of s=V/E$_R$ on the estimation of depth by data point. In this case we have:
1013nm light, s=V/E_R=0.9±0.05 → 216±12 nK.
1064nm light, s=V/E_R=0.75±0.05 → 195±11 nK.
1120nm light, s=V/E_R=0.65±0.05 → 130±10 nK.

Chapter 3

Spatial Bloch oscillations of a quantum gas in a "beat-note" superlattice

All the results showed in this chapter are reported in [25] and they refer to the Beat-Note superlattice as it was presented theoretically in chapter 1.3.
To investigate the properties of the BNSL, we prepare a Bose-Einstein condensate of ^{39}K, $|1,1\rangle$, in its ground state, we employ it to measure the energy gaps between the first three bands and we study Bloch oscillations in the presence of an external force.
These measurements demonstrate that the BNSL is equivalent to a standard lattice up to depths of the order of the recoil energy of the two combined lattices. Moreover, when cancelling the interatomic interactions by means of a magnetic Feshbach resonance, the dynamics exhibits a coherence up to 1 s, demonstrating how this new technique provides very stable potentials with an arbitrarily long periodicity.
For this reason, this novel lattice is the ideal candidate for the coherent manipulation of atomic samples at large spatial separations. It might find direct application in atom-based technologies, like trapped atom interferometers [17], where the device sensitivity scales proportionally to the separation of the trapped modes, and quantum simulation of Hubbard-like models [70, 71, 72, 73].
I start describing the calibration of the lattice depth, that we perform measuring the on-site trapping frequencies. From the knowledge of the lattice depth we can estimate the tunneling rate between neighbouring sites by the help of numerical simulations. Then I show some measurements of the residual forces on the atom observing the clouds in free expansion. The calibration of this force is mandatory to finally study Bloch oscillation between the sites of BNSL. Finally, I compare the experimental data with the theoretical expectation predicted for Bloch oscillations.

3.1 Calibration of BNSL depth

Once we have evaporatively cooled the gas to condensation, we adiabatically ramp up two optical lattices along the x axis (see Fig. 2.1) with $\lambda_1 = 1064.5$nm and $\lambda_2 = 1013.7$nm. The radial beam, which propagates along the same axis, provides radial harmonic potential of $\omega_{x,y} \approx 2\pi \times 200$Hz. The two lattices realize a BNSL with $d_+ \approx 0.5\mu$m and $d_- \approx 10.6\mu$m with n=20. Turning off the IPG beam, that gives a tight longitudinal confinement, and letting the condensate expand we can decide how many BNSL sites to load (see Fig. 1.4).
As explained in chap 2.5, since the position of the effective minima depends on the relative phase between the starting lattices, both the lasers are locked to the same cavity reference.
We ramp up the two lattices to a final depth $V_0 \sim 200$nK, which means we are in the part

of the spectrum which doesn't depends on the phase $\phi = \phi_1 + \phi_2$.
We detect the in-situ atomic density from the z direction and we observe spatial separation of about 10μm between independent condensates localized in the effective sites of the BNSL. In our system, since we have access to the atomic population within the single BNSL site, we can measure lattice depth by measuring the oscillation frequency of the condensate in regimes where the tunnelling energy J_{eff} to the neighbouring sites is negligible. Indeed in this regime the energy bands of the BNSL (see Fig. 1.7) are flat, and the oscillation frequency correspond to the first energy gap.
The dynamics is triggered by a suddenly shift of the minima of the BNSL, which put the condensate out of equilibrium. In order to do this, we change the frequency of the RF sent to the double passage AOM placed on the optical path of 1064 laser (see Fig. 2.2). Thanks to the absorption imaging, we calculate that the displacement of the minima respect to a variation of the frequency is of the order of $\Delta x_0 \approx 0.02$ μm/MHz and the range, and with the double passage AOM we can change the frequency of the laser of about 160 MHz..
Some examples of oscillations of the center of the condensate in a single site, recorded for different values of the lattice depth, are reported in Fig. 3.1

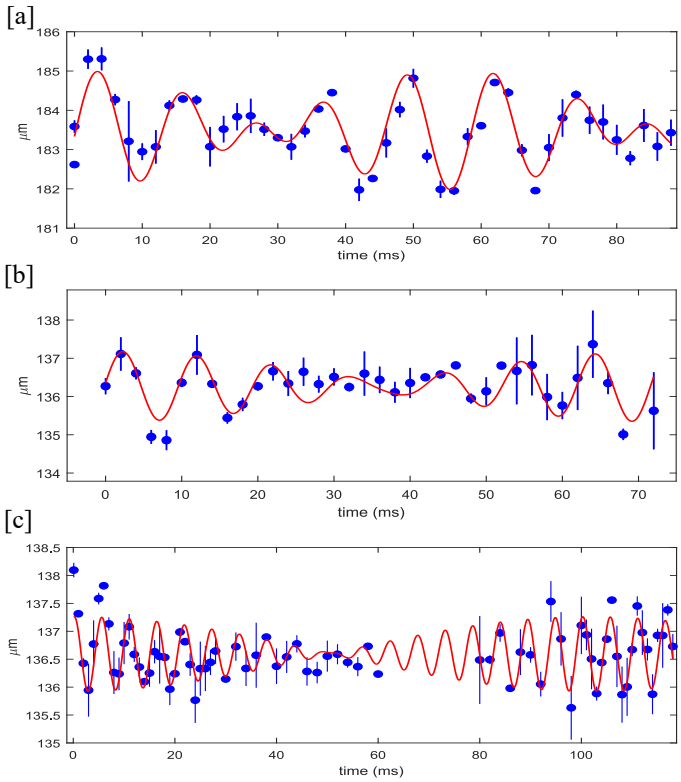

Figure 3.1: On-site oscillations of the condensate in the BL for different values of the lattice depth: a) 400 nK b) 200 nK c) 140 nK. We observe the beating of two frequencies that correspond to the first two energy gaps

where we intentionally shift the minima by an amount sufficiently large to project the initial condensate wavefunction on the first three bands.
Indeed, if ψ_0 is the initial wavefunction of the condensate loaded in a single site of the BNSL, after the shift Δx we can decompose it as a linear combination of the energy eigenfunctions ϕ(x) of the shifted BNSL, $\psi_0(\mathrm{x}) = \sum_i \mathrm{c}_i\phi_i(\mathrm{x})$. The larger is Δx the larger is the number of bands, with energy E_i, involved.
The evolution is $\psi_0(\mathrm{x},\mathrm{t}) = \sum_i \mathrm{c}_i\phi_i(\mathrm{x})e^{i\mathrm{E}_i\mathrm{t}/\hbar}$ and the expectation value of the center of mass position $\langle\mathrm{x}(\mathrm{t})\rangle$ at time t contains the oscillating terms with frequencies $\omega_{i,j} = (\mathrm{E}_i - \mathrm{E}_j)/\hbar$ and amplitude $2\mathrm{c}_i^*\mathrm{c}_j\langle|\mathrm{x}|\rangle$. As said before, we can easily shift the position of the minima up

to $\Delta x \approx 2$ μm, a quantity sufficient to involve three levels in the dynamics.
The center of mass oscillation of the gas is then characterized by the beating of two frequencies that correspond to the first two energy gaps, therefore we fit all the oscillations with the product of two sinusoidal functions and we derive the frequencies ω_1 and ω_2. The fit in Fig. 3.1 reproduces very well the observed behaviour. The amplitude of the beating oscillation provides info on the amplitudes $|c_0|^2 \approx 0.6$, $|c_1|^2 \approx 0.3$, $|c_2|^2 \approx 0.1$, that are in agreement with the predictions of a numerical analysis.
In Fig. 3.2 we compare the measured values of ω_1 and ω_2 with the theoretical expectations and their good agreement confirms the prediction and provide a good calibration of the energy gap and the tunnelling of the BL.

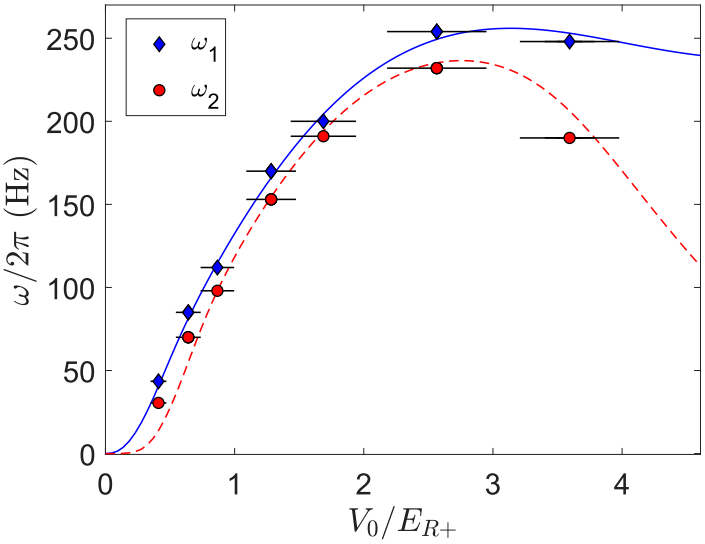

Figure 3.2: Measured values of ω_1 and ω_2 as a function of V0 compared with the theoretical values, blue line and red dashed line respectively. Error bars on the lattice depth take into account the uncertainties of the beam size on the atoms and of the optical power.

As pointed out in chap.1.3.1 if $V_0 \leq E_{R_+}$, according to Eq. 1.52, the effective potential is sinusoidal and its anharmonicity leads to two slightly distinct frequencies that scale with the square root of V_{eff} , i.e. linearly with V_0. For larger values of V_0, where the analogy with a large spacing standard lattice is no longer valid, the first energy gap of the BNSL deviates from the linear behaviour, while the second one reaches a maximum and then decreases to zero.

3.2 Residual forces on the system

During the measurements of the trapping frequencies, for small values of the lattice depth, we have observed a residual force on the atoms that tends to drag them away from the initial position. We have find out that there is a spurious external magnetic field gradient that causes an acceleration a$\approx 10^{-2}$ g, where g = 9.81 m/s^2. To compensate it, we exploit the optical force provided by the dipole trap propagating along the x axis whose focus position is shifted with respect to the condensate by a distance equal to the Rayleigh range of the beam. In this way the dipole potential imprints a force on the sample that can be controlled tuning the intensity of the beam.
In order to measure this residual force on the condensate at high magnetic field (all the experiment in the lattice are performed in the state $|F = 1, M_F = 1\rangle$ around 350 G), we can

observe the motion of the atomic cloud during a free expansion inside the beam for different values of the intensity and magnetic field. All the trajectories are shown in figure in Fig. (3.3) where I also report the correspondent measured accelerations as a function of the power P_{RAD} of the radial beam.

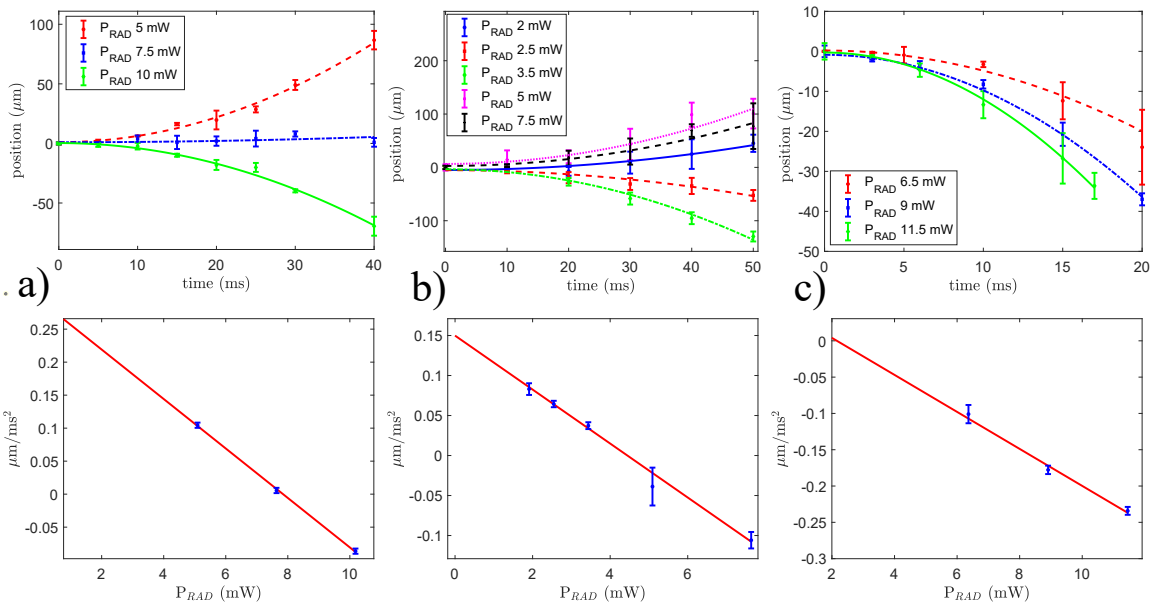

Figure 3.3: Trajectories of the free expanding condensate in the radial beam (upper) a) correspondent measured acceleration as a function of its optical power (lower). The measurements are performed with only the Feshbach field on at 350 G (a), with the gravity compensation switched on (b) and with a non magnetic cloud at B=83 G (c).

The first measurement (Fig. 3.3a) was taken at B≃350 G. We fit the data with a parabolic function and extract the acceleration which, as expected, goes linearly as a function of P_{RAD}. The intercept at P_{RAD}=0, which provides a measurement of the residual gradient in this configuration, is $a_{250G} \simeq 0.29\pm0.01$ μm/ms^2 $\sim 3\cdot10^{-2}$g, where g is the gravity acceleration. this value is surprisingly high, and explain why the atoms can't survive during the loading of the BNSL.
A second set of measurements (Fig. 3.3b) was taken in the working condition, B≃350 G + the gravity compensation coils on, and we find a gradient a factor of two smaller. This is due to the fact that the levitating system creates a force in the opposite direction that naturally helps to compensate the residual gradient. The extrapolated acceleration is $a_{250G} \simeq 0.160\pm0.015$.
Finally, in order to check if the strong acceleration that we measured comes only from spurious magnetic fields, we observe the motion of a condensate in the state $|F = 1, M_F = -1\rangle$ at B=83 G (Fig. 3.3,c). At this field the sample has a negligible magnetic dipole moment, of the order of $3\cdot10^{-3}\mu_B$ where μ_B is the Bohr magneton. The measured acceleration is $a_{250G} \simeq 0.06\pm0.02$, much smaller than the previous cases. It indicates that the main contributions to the residual gradients are provided by some magnetic effects acting on the apparatus. In particular, the resulting spurious magnetic gradient is $a_{250G} \leftarrow 0.22\pm0.01$G/cm.
A possible explanation can be that, due to the high field and the high currents that flow in the Feshbach coils, some thermal and mechanical effects can occur, leading to some deformations of the structure and the position of the coils. Moreover, the high field can magnetize some objects around the chamber, leading to a deformation of the magnetic field lines.
Finally, the little measured acceleration at B=83 G could be due to the non perfect horizontal alignment of the radial beam. If the direction of the beam has an angle α with the horizontal

direction, a fraction of gravity equal to gsin(α) is applied on the sample along x.

3.3 Calibration of the local force

As a consequence of what has been said in the previous section, it is necessary to compensate for this residual force on the atoms. The solution adopted in this work is tuning the intensity of the dipole trap (radial beam), such that we can finely adjust the total external force F along the beam direction around zero. Moreover, this give us a way to introduce a known and controllable force in the place of the atoms, which can be used to trigger the oscillations presented in the next chapter.
The force felt by the atoms is the dipole force F=-∂U/∂x, where U is the dipole potential in 1.1. Since it depends by the peak intensity $I_0(x)$ of a Gaussian beam, it means it scale as $\propto 1/\omega^2(x)$, where $\omega(x)$ is the $1/e^2$ waist. The last evolves in space as $\omega(x)=\omega_0\sqrt{1+(x-x_0)/x_R}$, with ω_0 the waist in the focus placed at x_0 and x_R the Rayleigh range. As a consequence, F shows a strong dependence on the position. In order to minimize such dependence we place the atoms around where the derivative of the force is negligible, which for us it means that the atoms are placed about 450±50 μm from the focus of the radial beam.
To calibrate this force applied to the atoms we observe again the ballistic expansion of the sample inside the radial beam. We set the scattering length of the condensate to a slightly negative value, in order to reduce the spread of the wave function, and we record the position of the centre of mass after a fixed time δt=50ms as a function of the intensity of the radial beam. During this evolution the displacement of the condensate from the starting point is always smaller than 50 μm. The results shown in Fig. 3.4, where we report the strength and the sign of the total force as a function of the optical power, can provide a first calibration of the local force as a function of the power of the beam. From a linear regression fit we obtain a calibration of the local force that can be tuned both in strength and sign.

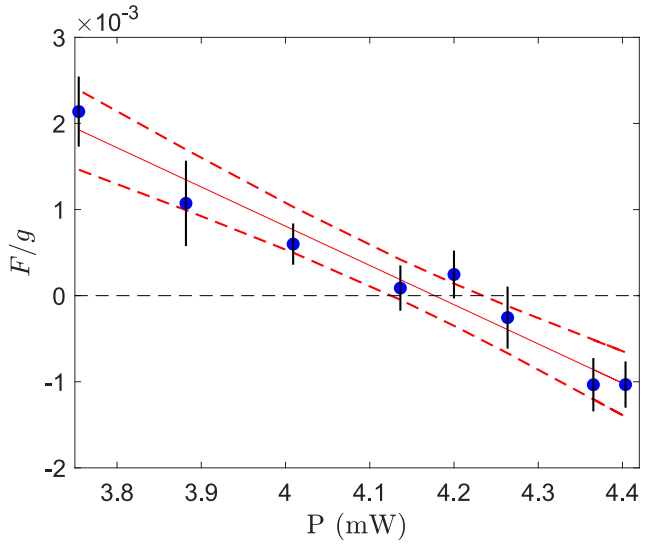

Figure 3.4: Local force on the atoms as a function of the optical power of the radial beam, obtained measuring the position of the cloud after 50 ms of ballistic expansion. The dots are data points, the solid line represents the linear fit with the best fit parameters and the dashed lines correspond to the confidence interval.

3.4 Spatial Bloch oscillation in a ∼10μm BNSL

In order to prove the analogy between a BNSL and a single wavelength large spacing optical lattice in the low V_0 limit we decide to observe the coherent dynamics between the different sites of the BNSL and measuring the correspondent effective tunneling J_{eff}. We then perform spatial Bloch oscillations, starting with a condensate loaded in a single site of the BNSL and detecting the subsequent oscillation of the density distribution, which spans few sites of the BNSL, driven by an external force [34, 35, 74].
As said in chap 1.1.4, the amplitude A of such breathing mode is proportional to the ratio between the tunneling rate, that depends on the lattice depth and the lattice spacing, and the potential energy difference among the sites. To have A larger than 1, since the dynamics that we want to observe has a time scale of few Hz, we need to work with very shallow lattices. The first energy gap of the BNSL in this condition is very low, of order of tens of Hz, so we need to pay attention to avoid unwanted excitations in the upper bands.

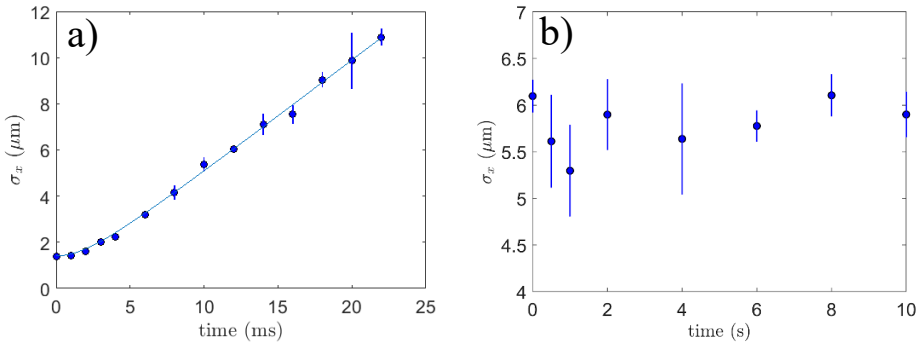

Figure 3.5: a)size of the cloud load in a single site of a BNSL with V_0=85 nK (first energy gap≈ 50 Hz) in free expansion and compared the evolution with the theoretical predictions for a final trapping frequency of 50 Hz.
b) Measure of the size of the condensate after turning off all the trap with a time of flight of 12 ms, as function of holding time.

In the following we describe the experimental procedure.
After the evaporative cooling in the dipole trap we ramp up the BNSL adiabatically in 300 ms to a lattice depth ∼1.5E_{R_+} (energy gap of ∼120 Hz). We populate only one site with a condensate of about $5{\cdot}10^3$ atoms, ensuring a negligible tunneling between neighbouring ones and keeping small repulsive interactions that help to evaporate the excitations. Once set the working value of the force, we switch off the dipole trap (IPG) that provides confinement along x and we decrease the BNSL depth to V_0 ≃70(±2) nK∼0.3 E_{R_+} in ∼50 ms (final energy gap of ∼40 Hz). The procedure is performed adiabatically with respect to the trapping frequencies of a single site but on a time-scale much shorter then the Bloch period. At the same time, we decrease also the intensity of the radial beam, changing the scattering length to the level of 0.05 a_0, where a_0 is the Bohr radius. This procedure helps to evaporate excitations that can be still present after the first step, and the negligible scattering length will minimize the decoherence induced by interactions during the subsequent oscillation. After this second evaporation, we change the power of the radial beam to the working value, setting the total final force. We set t = 0 at the end of this ramp. Obviously, mainly when the force is large, the dynamics can already start during the ramp, but this delay corresponds only to a phase shift with respect to the starting point.
To check if this reduction of the potential depth, used to trigger Bloch oscillations, is adi-

abatic, we performed an intensity ramp to values (85 nK) comparable to the ones used in the experiment (70 nK) but slightly larger to freeze the dynamics. We measured the size of the cloud in free expansion and compared the evolution with the theoretical predictions for a final trapping frequency of 50 Hz. We report the result in Fig. 3.5a as a function of the expansion time. The very good agreement confirms the ground state preparation of the sample. We also studied in Fig. 3.5b the energy of the sample as a function of the time spent in the BNSL by monitoring its size after a time of flight of 12 ms. As shown in the second Figure, no discernable increase is observed over a time scale of several seconds of evolution, confirming the occupation of only the first band of the lattice.

In Fig. 3.6 we report examples of absorption images of the condensate during one Bloch oscillation, together with the spatial density profile integrated in one direction. Since at t = 0 all the atoms are localized in a single site, the center of mass motion is frozen and we observe only a symmetric breathing evolution of the size. From 1.23, the on-site fractional populations evolve in time as [35]

$$n_l(\mathrm{t}) = \left|\mathcal{J}_l\left(\frac{4\mathrm{J_{eff}}}{\delta}\sin\left(\frac{\delta \mathrm{t}}{\hbar}\right)\right)\right|^2 = \left|\mathcal{J}_l\left(\frac{4\mathrm{J_{eff}}}{\delta}\sin\left(\frac{\pi \mathrm{t}}{\tau_B}\right)\right)\right|^2 \tag{3.1}$$

where $\mathcal{J}_l$ are Bessel functions of the first kind and $\delta = \mathrm{Fd}_-$ is the energy difference between neighbouring sites and τ_B is the Bloch time. Experimentally we count the atoms that remain in the starting well N_0 and the ones that tunnel to the other sites N_{tr}=$\sum_{i\neq 0}(\mathrm{N}_{+i} + \mathrm{N}_{-i})$.
In Fig. 3.7a we report a typical time evolution of N_{tr} in unit of the total number N_{tot} at each time. We observe a clear oscillation with the average amplitude reducing on a timescale of ≈1 second. Starting from Eq. 3.1 we fit the experimental data with the phenomenological model

$$f(\mathrm{t}) = \exp(-\mathrm{t}/\tau)\left(\left|\mathcal{J}_l\left(\frac{4\mathrm{J_{eff}}}{\delta}\sin\left(\frac{\pi \mathrm{t}}{\tau_B}\right)\right)\right|^2 - \mathrm{N}_f\right) + \mathrm{N}_f \tag{3.2}$$

such that f(0)=0 and f(t → inf)=N_f, where N_f is a steady value of the transferred population reached through an exponential decay with a time constant τ.
The observed decay of the oscillation contrast might be due to different sources of decoherence, like the presence of a spurious harmonic potential along the x axis or a residual interaction energy [75]. In Fig. 3.7b we compare the data with the result of exact numerical simulations of the Bloch dynamics in presence of a residual scattering length of 0.05 a_0 and of a longitudinal harmonic potential of 1.3 Hz (the one due to the presence of radial beam). In both the cases we observe a similar reduction of the amplitude on a time scale that is comparable with the best fit value τ of the order of 500-600 ms. From the fit we can estimate the Bloch period $\tau_B = h/\delta$, that is related to the external force F=δ/d, and the amplitude of oscillation A=$4\mathrm{J_{eff}}/\delta$, that is linked to the tunneling energy $\mathrm{J_{eff}}$.
We repeat the same procedure for different values of the applied force, tuning the power of the radial beam.
In Fig. 3.8a we investigate the linear dependence of δ on the external force F applied, where the dotted line indicates the theoretical predictions, while the shaded area takes into account the uncertainty in the calibration of the external force. Note that only a limited range of forces has been explored because outside it, the small depth $\mathrm{V_{eff}} \approx 3$ nK implemented, would cause Landau-Zener interband transitions and atom losses. This could be prevented increasing V_0 but the consequent reduction of the tunneling energy $\mathrm{J_{eff}}$ would reduce also A and the visibility of the spatial oscillations.
In Fig. 3.8b we plot the amplitude A as a function of δ and compare the results with the values we expect from the estimation $\mathrm{J_{eff}}$=(0.7±0.05) Hz, derived from the experimental calibration of V_0. We note that a good agreement is achieved in both plots, although a deviation of the measurements from the expected values is observed for Bloch frequencies ≈ 2 Hz.

For small values of the force, precise measurements are currently limited by the decoherence sources described above.

3.5 Sensitivity Bounds

In [76] it was calculated the best-achievable sensitivity for matter-wave interferometer consisting of a BEC undergoing spatial Bloch oscillations in an optical lattice oriented horizontally. We have talked, across this work, of BEC localized in a single site as initial state, but in [76] several conditions was studied. In particular it was shown the influence of the choice of the localization of initial state and also the choice of the observables to use, i.e. atomic population in the sites of the lattice or the width of the distribution. In par.1.1.4 we said that the hamiltonian H in Eq. 1.21 sets the dynamics of the Bloch oscillations of the gas in the lattice. Again, let's refer to energy difference between neighboring sites as $\delta = m_a \mathrm{da}$, where a is the acceleration and m_a is the mass. The highest precision an interferometer can achieve is given by the inverse of the Quantum fisher information $\mathrm{F_q}$ [77]

$$\mathrm{F_q} = 4(\langle \hat{h}^2 \rangle - \langle \hat{h} \rangle^2) = 4\Delta\hat{h}^2 \tag{3.3}$$

where $\hat{h}$ is the generator of the transformation set by the evolution operator $\hat{\mathrm{U}}(\mathrm{t}) = e^{i\mathrm{Ht}/\hbar}$

$$\hat{\hbar} = i\frac{\partial \hat{\mathrm{U}}(t)}{\partial a}\hat{\mathrm{U}}^{\dagger}(\mathrm{t}) \tag{3.4}$$

For a pure state like ours, the calculation of $\hbar$ together with the Cramer-Rao lower bound [78], gives the ultimate sensitivity as

$$\frac{\Delta \mathrm{a_{opt}}}{\mathrm{a}} = \frac{1}{\sqrt{\mathrm{F_q}}}\frac{1}{\mathrm{a}} \tag{3.5}$$

This sensitivity monotonously improves with time as a consequence of the action of the derivative in Eq. 3.4 of the evolution operator. This reflects the growth of information about a deposited in the system the larger is the number of Bloch times τ_B that are explored.
Now that the bound is set, the choice of different observables can lead you more or less close to it. In particular, assuming that one has single sites resolution, the sensitivity one gets from counting the number of atoms in each sites is periodic and reaches the optimal bound at the multiples of the Bloch period. Instead, the sensitivity from measuring the width of the cloud in the lattice is in general worse than the previous method, however it also reaches the ultimate bound at the multiples of the Bloch period.
It is interesting to understand the role of initial state size. As well-known properties of a standard Bloch-oscillation interferometer, the ultimate sensitivity increases with the initial coherence length, since larger is the initial number of occupied sites, narrower is the momentum distribution. Also for a spatial Bloch Oscillation interferometer (SBOI) the Quantum Fisher information predicts that the ultimate bound can improve with initial size. Nevertheless, the sensitivities of the two estimation protocols described above deteriorate. This means that from the point of view of these two strategies the optimal operation of an SBOI requires to start with atoms loaded in a single site of the lattice.

3.5.1 Dependence on the lattice parameters

The sensitivity one gets, in the limit of a BEC initially localized in only one site, from counting the atoms in each sites during evolution is [76]

$$\Delta \mathrm{a} = \frac{\mathrm{a}}{2\sqrt{2\mathrm{N}}}\frac{1}{\mathrm{J}}\frac{\hbar}{\mathrm{t}} = \frac{\mathrm{a}}{2\sqrt{2\mathrm{N}}}\frac{1}{\mathrm{F}(\mathrm{dJ}/\delta)}\frac{\hbar}{\mathrm{t}} \tag{3.6}$$

with t multiple integer of Bloch periods τ_B, where N is the number of atoms. The second equality in Eq. 3.6 is just to point out some characteristic of this sensitivity. The quantity

(dJ/δ) is the size of the Wannier Stark states (d, lattice sites separations, times localization length J/δ).
A spatial Mach-Zehnder atom interferometer (SMZI), where two modes are separated by a distance $\tilde{d}$ in presence of an external force F, accumulates a phase difference $\phi = Ftd/\hbar$, detected with a shot noise limit $1/\sqrt{N}$. As a consequence, the sensitivity will be

$$\Delta a_{SMZI} = \frac{\delta\phi}{\phi} a = \frac{a}{\sqrt{N}} \frac{1}{F\tilde{d}} \frac{\hbar}{t} \tag{3.7}$$

As one can see, the sensitivity of a spatial Bloch oscillation interferometer in Eq. 3.6 is equal to the one of a SMZI where the separation between the two modes is of the order of the maximum spatial spread of the atomic wave function over the lattice during the dynamics. As matter of fact, large separation between the spatial modes is crucial to have a sensitive trapped atom interferometer. This can be easily fulfilled in an SBOI by simply increasing the tunnelling energy or reducing the strength of the external force.

3.5.2 Practical constraints

Next question can be how to choose the d and F in an experiments (realistic environment) to reach the best sensitivity.
Eq. 3.6 doesn't seems to depend on d, however a too small d (fraction of micron) is an evident limitation, since it makes impossible to load many atoms in a single lattice site due to high three body losses when atomic densities are large. This, in the end, limits the improvement from the shot-noise scaling, i.e., with the inverse of $\sqrt{N}$. In addition, if the lattice spacing is too small, it is challenging to precisely count the atoms in each site. As a consequence larger lattice spacing naturally improves the sensitivity of a SBOI.
This choice highlights other aspects: larger d means reduce the tunnelling term J between the sites. But the amplitude of Bloch oscillations is $\propto J/\delta$, so to observe them we need $J \geq \delta = m_a ad$. A solution is reduce the external force F, but we have to consider that in real experiments the interrogation time t is finite, due to decoherence induced by residual interactions or experimental noise, we cannot work with arbitrarily small forces but keep $\tau_B = h/(m_a ad) < t$. So, using the maximal value of J as a function of d, i.e. when the width of the first band is of the order of the recoil energy $J \approx E_R/4 = \hbar^2\pi^2/8m_a d^2$, we obtain an upper bound for d by the condition $J \geq \delta = m_a ad$

$$d_{max} = \left(\frac{\hbar^2\pi^2}{8m_a a}\right)^{1/3} \tag{3.8}$$

which, exploiting $\tau_B = h/(m_a ad) < t$, lead a minimum value for a

$$a_{min} = \sqrt{\frac{\hbar\pi}{m_a}} \frac{8}{t^{2/3}} \tag{3.9}$$

Note, Eq. 3.8 can be also rewrite as a function of the coherence time t $d_{max} = \frac{1}{4}\sqrt{\frac{\hbar\pi t}{m_a}}$.
To consider a realistic example of a SBOI like the one we perform in our experiment, let's take a coherence time t$\sim$1 s and N$\sim 10^4$ atoms. From Eq. 3.8 we get the smallest measurable acceleration $\approx 5\times10^{-5}$g and an optimum lattice spacing $d_{min} \approx 17\mu$m. From Eq. 3.6 if we neglect fluctuations of the tunnelling energy, the relative uncertainty is 4×10^{-4} and a single shot sensitivity is of the order of 10^{-8}g. This results proves the importance of implementing large spacing lattices, using for example BNSL.

3.6 Conclusions

In conclusion, we reported the realization of an innovative superlattice based on the beat-note between two retroreflected laser beams with commensurate wavelengths. Our studies prove that the resulting potential is equivalent to a large-spacing single-wavelength optical lattice in the limit of small depths, i.e $V_0 < E_{R_+}$. For larger values of V_0, in chap1.3 we saw that BNSLs can be used to create arrays of atomic ensembles with negligible tunnelling between the sites.
The high stability of a BNSL is demonstrated observing a coherent tunnelling between neighbouring sites of the BNSL in presence of a small force of the order of 10^{-4} g with a spatial resolution of 10 μm.
To our knowledge, we managed to observe the longest ($\sim$ 1 sec) coherent evolution ever reported for a BEC trapped in spatial modes separated by tens of microns. That coherence time corresponds to a sensitivity of the order $5{\cdot}10^{-5}$. The main limitations to the coherence time and the precision of the measurements are related to the limited control we have in the way we tune the external force, i.e, optically.
Bloch oscillations using more homogeneous forces and experiments performed with variable atom numbers will allow to identify what is currently limiting the performance of our Bloch oscillations interferometer. We expect that BNSLs will strongly contribute to the improvement of the sensitivity of trapped atom interferometers, as studied in [76] , where using the metrological tool known as the quantum Fisher information, it was calculated the best-achievable sensitivity for matter-wave interferometer consisting of a BEC undergoing Bloch oscillations in an optical lattice oriented horizontally.
In addition, the demonstrated intrinsic stability of BNSLs makes them a valuable tool for the precise manipulation of atoms at large distances in several future quantum technologies [79, 80, 81].

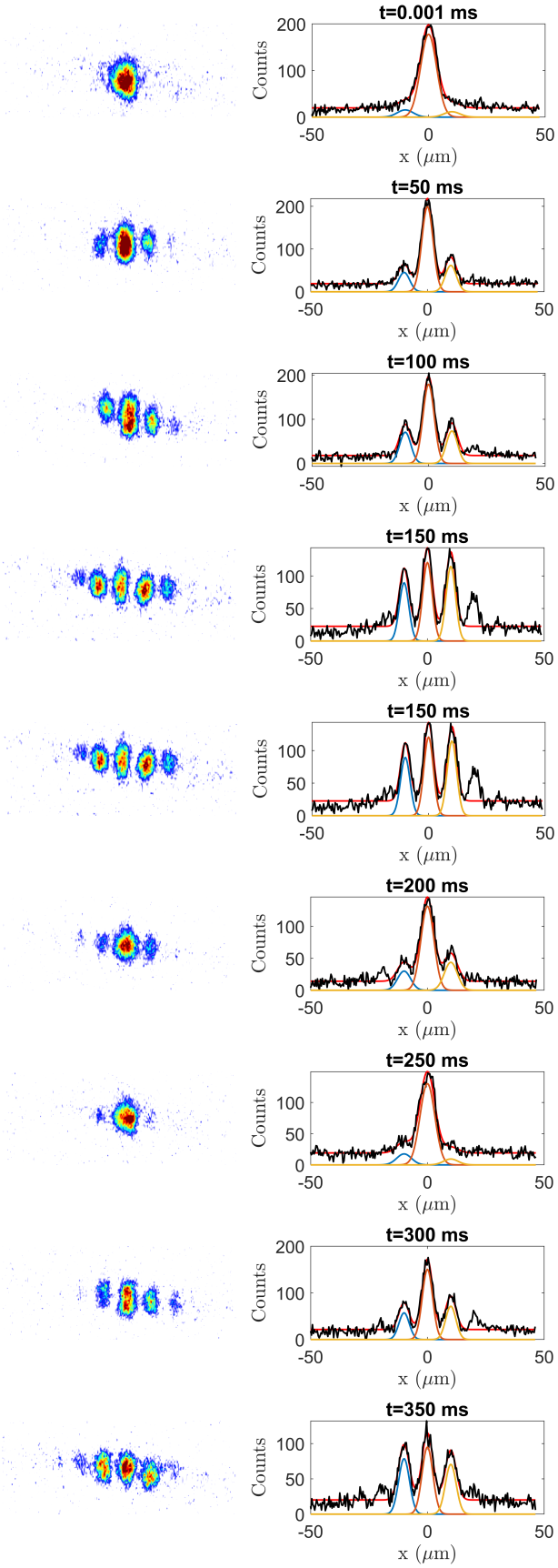

Figure 3.6: In-situ images and correspondent density profile during a Bloch oscillations together with the fit performed with a triple Gaussian function.

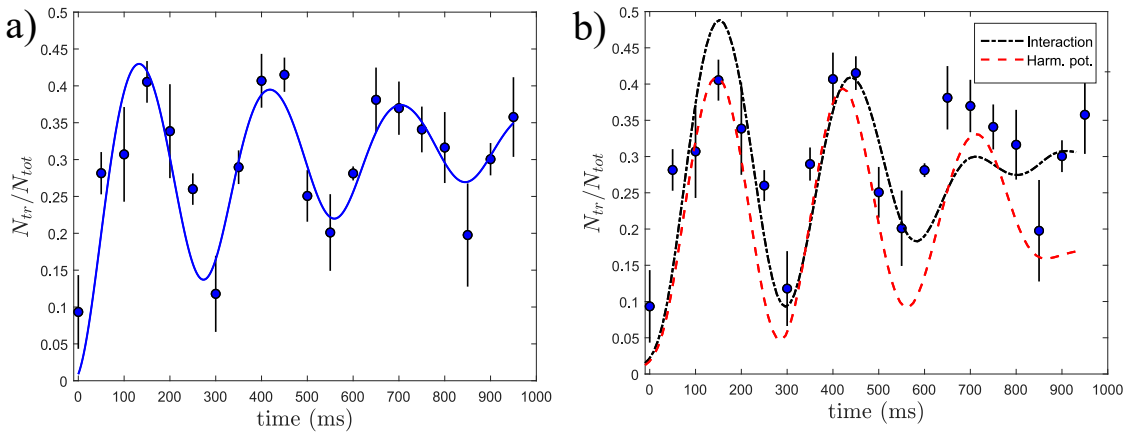

Figure 3.7: a) time evolution of fractional atom number in the starting site N_0 and the sum of the populations in the neighbouring sites N_{tr}. The solid line is a fit performed using Eq. (3) times an additional exponential decay of the amplitude. The error bars represent the statistical uncertainty and correspond to the standard deviation of the mean.
b) The black dash-dotted line and red dashed line correspond respectively to numerical results in presence of a residual interaction of 0.05 a_0 and an harmonic axial potential with a frequency of 1.3 Hz.

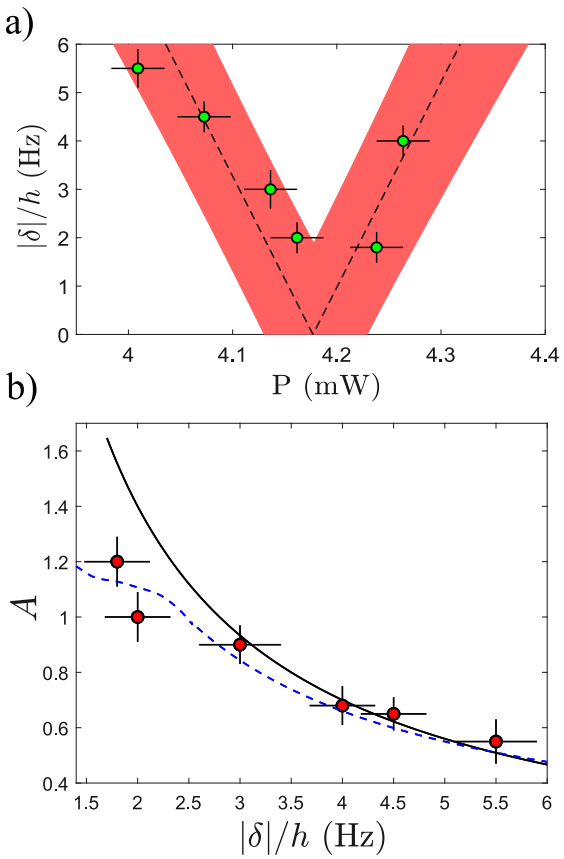

Figure 3.8:
a) Energy difference between lattice sites (dots) derived from the Bloch frequency measurements as a function of the optical power of the beam used to tune the external force. The horizontal error bars corresponds to the uncertainty on the optical power. The dotted line is the theoretical prediction for the best fit parameter provided by the calibration and the shaded area takes into account its indetermination.
b) Amplitude of the oscillation A as a function of the energy difference between lattice sites. The error bars correspond to the uncertainty of the amplitude and the frequency provided by the fit of the oscillations. At lower values of δ the effect of force inhomogeneities are more significant and both frequency and amplitude deviate from theory. The dashed line is the result of numerical simulations where a longitudinal harmonic potential of 1.5 Hz is included.

Chapter 4

Multimode trapped interferometer with noninteracting Bose-Einstein condensates

In this chapter I experimentally demonstrate a new interferometric method for trapped quantum gases based on a multimode configuration, with more than two interferometric paths closed by a harmonic potential. The coherent splitting and recombination of a BEC into multiple momentum components are realized by means of Kapitza-Dirac (KD) diffraction from a pulsed optical lattice. With this configuration, proposed theoretically for non-interacting systems by Li et al. [29], the harmonic potential has the same function of "mirror" light pulses to close the trajectories and prevents the spatial spread of wavepackets, instead occurring in free space. KD interferometers have been implemented experimentally either in the Mach-Zehnder two mode configuration in a waveguide [82], or in trap [83], still with only two interfering modes and with ^{87}Rb atoms for which the interpretation of the interference fringes is complicated by the interatomic interactions [84]. In our work we'll exploit a ^{39}K Bose-Einstein condensate (BEC) where the interatomic interaction can be cancelled exploiting Feshbach resonances.
More specifically, we realize a horizontal multi-mode trapped interferometer, where a BEC is KD diffracted by an optical lattice into components with momenta equal to multiples of the lattice wavevector k, i.e. with $p = m\hbar k$, with m integer.
A KD pulse initiates the oscillation of the different momentum orders which, after half an oscillation in the harmonic trap, return to the initial position with opposite momenta and are recombined using another KD pulse. If an external gradient is applied between the time of the two KD pulses, then it is possible to observe a clear dependence of the atomic populations in the different output momentum components on such force.
Importantly, all the momentum components spatially recombine at the trap minimum only if the potential is harmonic over their oscillation amplitude. This is easily the case for magnetic traps generated by macroscopic coils [83], but it represents a tight constraint for optical dipole traps, that are a mandatory choice for us since we have to control interactions through Feshbach resonances.
Here we use an optical trap and take advantage of a large-spacing ($\sim$5 μm) optical lattice, that reduces the recoil velocity, hence the oscillation amplitude, by a factor of 10, with respect to the common lattice spacing of 0.5 μm. In this way we are sure to remain in the harmonic region of our optical trap. We realize such periodic potential exploiting the Beat Note Superlattice idea (see chapters 1.3 and 3).
In the first part I explain the theory of Kapitza-Dirac interferometer, highlighting the difference between the half period (i.e. with only half oscillation in the harmonic trap) and full period interferometer. Then I describe the experimental setup and the characterization of

the harmonic potential, focusing on the effects of the anharmonicity of confinement potential on the interferometer output. Thanks to the full period sequence I show how I can optimize the timing between the two pulses looking at the output density distribution. Full period sequence is also a way to investigate relative frequency stability of the two KD pulses.
Finally in the last paragraph I show the measurements of the output atomic momentum distribution for a half period interferometer as function of applied magnetic gradient in the lattice direction.

4.1 Trapped Kapitza-Dirac interferometer

The effect of atoms diffracted by Beat-Note superlattice has been partly addressed in par.1.4. Now I'll resume the operation of the trapped Kapitza-Dirac interferometer with standard lattice pulses as in [29].
For simplicity, and to have direct connection with the experimental results, let's take into account only three momentum component undergoing the whole sequence, and try to give an intuitive picture.
We start with a wavepacket $\Psi_0(x)$ in the ground state of the harmonic oscillator with average position $\langle x \rangle' = x_0$. So, the first KD pulse (a lattice $V_0 \cos^2(kx)$ turned on for a time Δt) generates three momentum components m=0,±1; after this pulse, the half oscillation in the trap reverses the momentum of all these components, they overlap at the bottom of the trap, and finally the second KD pulse further splits each of them. Each momentum component in the output atomic distribution is the result of the interference of different starting momentum component. For instance, consider the output momentum component with m=+1. It emerges after the second KD pulse through two distinct paths, as illustrated in Fig. 4.1a

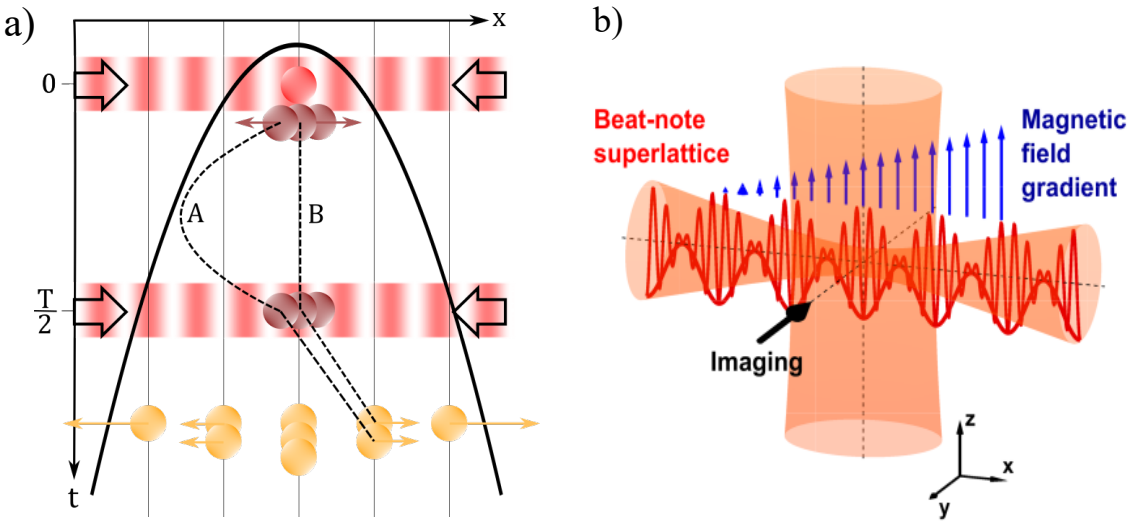

Figure 4.1: a) Sketch of the working of our trapped Kapitza-Dirac interferometer. Starting from a single BEC (red), two KD pulses at t = 0 and T/2 create and recombine the momentum components that oscillate in the trap (purple) and are finally detected after a free expansion (yellow). Colored arrows, indicating the momentum vectors, are not shown at t = T/2 for clarity. We highlight the two different paths A and B as identified in the text, from which the m = +1 component emerges at the output of the interferometer.
b)Sketch of the optical and magnetic potentials applied on the atoms

Path A: the m=-1 component is generated by the first KD pulse, its momentum is reversed into m=+1 by the half-period evolution, and then it is left unperturbed by the second KD

pulse;
Path B: the m = 0 component emerging from the first KD pulse is scattered into m = +1 by the second pulse.
As it happens in any light-pulse interferometer[85], the interferometric phase accumulated on each path is obtained as the sum of the terms originated during the light-atom interaction and terms due to the evolution between the light pulses. The latter are given by the Action along the classical trajectory [86], which vanishes whenever the time separation between the two light pulses equals an integer multiple of the harmonic half period, independently of the initial momentum.
So, on path A the only phase factor $\mathrm{e}^{-i2\mathrm{kx}_0}$ is imprinted by the first KD pulse, while on path B the second KD pulse imprint a phase factor $\mathrm{e}^{+i2\mathrm{k}x_0}$, and their sum produces interference on the population of the m=+1 momentum at the interferometer output $\propto \cos(2\mathrm{kx}_0)$.
Now, consider an external acceleration a applied on the atoms during the time between the two pulses. The effect of a on the system is to induce a displacement of the trap minimum, d=a/ω^2, measured with respect to the wave front of the applied optical lattice, where ω is the trap frequency of the harmonic potential. The displacement d is then encoded in the phase factor $\mathrm{e}^{+i(2\mathrm{k}x_0+2\mathrm{kd})}$ imprinted by the second KD pulse on path B. This time by the interference we have that the m=+1 population at the output of the interferometer is proportional to $\cos((2\mathrm{k}x_0 + \mathrm{kd}))$, so it depends on d (i.e. from acceleration a). So, looking at total momentum distribution at the output of the interferometer and counting the fraction of atoms in each momentum component I can get information about a.
A more rigorous discussion can be found in [29], where the wave function at the interferometer output is exactly calculated. The wavefunction at the interferometer output after half oscillation in the harmonic potential is [28]

$$\Psi_{\mathrm{half}} = \Psi_0 \sum_{\mathrm{m}=-inf}^{\mathrm{m}=+inf} i^{\mathrm{m}} \mathcal{J}_{\mathrm{m}}\left(2\beta \sin(\phi)\right) \times \ \times e^{(+i\mathrm{mkx})} e^{(-i\mathrm{m}\delta)} \tag{4.1}$$

where $\beta = \mathrm{V}_0\Delta\mathrm{t}/\hbar$, $\mathcal{J}_{\mathrm{m}}$ are Bessel functions, ϕ is the interferometric phase which include kd, and δ is a phase which has only information about to the relative displacement of the two KD pulses (example, due to frequency fluctuations of laser source). The amplitudes $\mathcal{J}_{\mathrm{m}}$ hold the information about the external acceleration, so we need an observable constructed by the population of the m-th momentum component, which is

$$\mathrm{N}_{\mathrm{m}} = \left|\mathcal{J}_{\mathrm{m}}(2\beta \sin(\phi)\right|^2 \tag{4.2}$$

From the population we can easily find average and variance of the momentum

$$\begin{aligned} \langle \mathrm{m} \rangle &= \sum_{\mathrm{m}} \mathrm{m}\mathrm{N}_{\mathrm{m}} = 0 \\ \langle \mathrm{m}^2 \rangle &= \sum_{\mathrm{m}} \mathrm{m}^2 \mathrm{N}_{\mathrm{m}} = \sum_{\mathrm{m}} \mathrm{m}^2 \left|\mathcal{J}_{\mathrm{m}}(2\beta \sin(\phi))\right|^2 = 2\beta^2 \sin^2(\phi) \end{aligned} \tag{4.3}$$

We expect then a symmetric distribution with a rms momentum of $\mathrm{p}_{rms} = \sqrt{2}\beta|\sin(\phi)|$.
From those results a good observable (the one I'll focus on from now on) can be the fraction of atoms remaining in the initial m = 0 component, N_0/N: varying d this observable is expected to display a peak according to 4.2 that narrows as the number of interfering components increases. Indeed, the half-width at half-maximum (HWHM) phase, corresponding to $\mathcal{J}_0(2\beta \sin(\phi_{HWHM})) = 1/2$, is $\phi_{HWHM} = 0.56/\beta$, so the resolution of the KD interferometer increases with β at the expense of its dynamic range [29].
More specifically, the maximum resolution of the measured acceleration a is

$$\delta\mathrm{a} = \left|\frac{\mathrm{d}(\mathrm{N}_0/\mathrm{N})}{\mathrm{d}a}\right|^{-1} \Delta(\mathrm{N}_0/\mathrm{N}) \tag{4.4}$$

where $\Delta(N_0/N)$ is the experimental uncertainty associated with the observable. The resolution is maximum, i.e., δa is minimum, when the lattice position is such that the phase in 4.2 is close to an integer multiple of π. In this case for $\beta > 1$ we have

$$\delta a \approx \frac{\omega^2}{k\beta}\Delta(N_0/N) \tag{4.5}$$

Therefore, the resolution increases with β, that is proportional to the number of momentum components significantly populated, showing the benefit of multimode interference. This is consistent with the analysis based on the Fisher information and the Cramér-Rao bound [29, 87].
Everything said so far refer to an KD interferometric scheme with only half oscillation period of momenta components in the harmonic oscillator. It is worth to also look at the output wavefunction in the case of a full-oscillation KD interferometer, since it will be useful in the following:

$$\Psi(x)_{full} = \Psi_0(x) \sum_{m=-inf}^{m=+inf} i^m \mathcal{J}_m\left(2\beta \sin(\delta)\right) \times \times e^{(-imkx)} e^{(-im\phi)} \tag{4.6}$$

Eq. 4.6 shows that the populations of the momentum components in this full-period interferometer are sensitive only to the relative displacement of the two KD pulses δ. This means it is insensitive to the relative displacement between the trap and the lattice (and thus to external forces). I will exploit this property to calibrate the displacement of the lattice and investigate its stability.

4.2 Experimental setup

In order to realize the interferometer, we use a Bose-Einstein condensate of 10^4 ^{39}K atoms in the $|F = 1, M_F = 1\rangle$ state. Setting the magnetic field to B= 350.5(0.5) G I can effectively cancels the interatomic interactions via a broad Feshbach resonance, since the corresponding s-wave scattering length is $|a| < 0.05a_0$, a_0 being the Bohr radius.
The setup is slightly different from the one used in chap.3. The BEC is prepared in a crossed dipole trap created by two red-detuned laser beams, as sketched in Fig. 4.1(b): with a waist of 17 μm, the radial beam provides a tight radial confinement, along y and z, of $\omega_R \sim 2\pi \times$ 200 Hz, while the vertical beam provides the longitudinal harmonic potential, along x, with $\omega = 2\pi \times$ (31.7 $\pm$ 0.8) Hz. The large waist of the vertical beam ($\sim$100μm) ensures that the deviation from the harmonicity of the potential is below 1% at a distance of $\sim$10 μm from the center.
The beat-note superlattice potential along x is generated by overlapping two standing waves $V_1 \cos^2(k_1 x + \phi_1) + V_2 \cos^2(k_2 x + \phi_2)$ with $k_1 = 2\pi/1.013$ μm^{-1} and $k_2 = 2\pi/1.120$ μm^{-1}, and $V_{1,2}$ lattice depths. For $V_1 = V_2 = V_0 \leq E_{R_{1,2}}$, with $E_{R_{1,2}}$ energy recoil of the two lattices, the BEC experience the effective potential $V_{eff} = -\frac{V_0^2}{8E_{R_+}} \cos^2(k_- x + \phi_{1,2})$ as in Eq. 1.52, where now the spatial period is $\pi/(k1 - k2) \approx 5.32$ μm, and the phase $\phi_{1,2} = \phi_1 - \phi_2$ depends on the relative phase between the two combined lattices.
Both lasers are frequency locked to the same optical reference cavity via sideband-locking technique (see par.2.5.2) that allows us to tune $\phi_{1,2}$ dynamically by adjusting the radio frequency of one sideband.
Additionally, to investigate the effect of an external force along the x direction we apply a magnetic field gradient. Since ^{39}K atoms feature a magnetic moment approximately equal to 0.95 μB (μB being the Bohr magneton) around 350 G, we can impart a force along the direction of the lattice by applying an external magnetic field gradient. Note, this gradient has been implemented to overcame the problem about the large residual gradient that add

an uncontrollable potential along lattices direction, which has been analysed in chap.2 and that for the experiment described in chap.3 was compensated optically. Indeed, it is very difficult to stabilize the optical intensity of a laser beam very well. In our case we estimated a relative uncertainty of 5×10^{-3}, that is equal to our current optimal sensitivity. For this reason, to achieve a better stability, I exploit the combination of the magnetic field produced by coils in anti-Helmholtz configuration, that provides a field along the axis (see Fig. 4.1) that scales linearly as a function of the distance from the centre of coil [88].
The resulting uniform force induces a displacement of the harmonic trap proportional to the coil current, which affects the momentum populations at the interferometer output, as explained in par.4.1. The displacement-versus-current conversion has been separately calibrated to be $\eta = (1.08 \pm 0.13)$ μm/A via the in situ position of atoms trapped in the vertical beam (see Fig. 4.2)

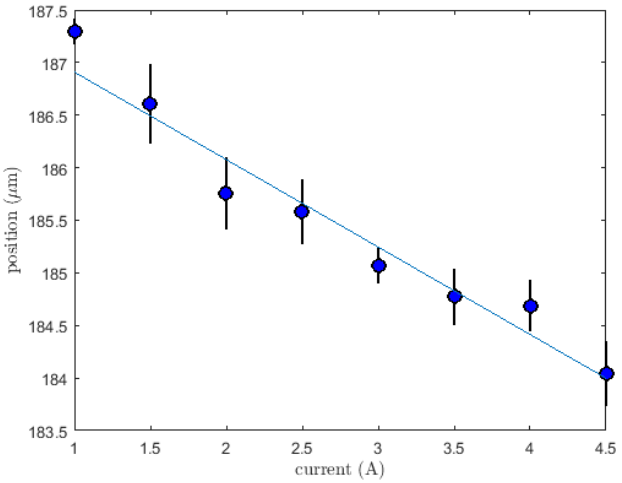

Figure 4.2: displacement of the minimum of optical dipole trap felt by the atoms as function of the current exploited to generate the magnetic gradient

In order to measure the longitudinal frequency given by the vertical beam and confirm that the potential is harmonic, at t = 0 we shine a pulse of the optical lattice with an effective depth of $V_{0\text{eff}} \simeq 30$ $E_{R\_}$ for $\Delta t = 120\mu$s, where $E_{R_} = k_B \times 8.7$nK. The pulse is long enough to completely deplete the m = 0 component. The images of the two components m $=\pm1$ are taken via absorption imaging (line of sight along the y direction in Fig. 4.1) and their position are reported as a function of time in Fig. 4.3. Both components display clear sinusoidal oscillations with an amplitude of 8.6(0.6) μm, in reasonable agreement with the expected value $\hbar k_{-}/m_a\omega = 9.2(0.2)$ μm.

4.3 Anharmonicity of confinement potential

The next step is understand how many momenta components I can generate diffracting my atoms with the BNSL. This is important since, from the theory of multimode interferometry [89], the sensitivity scales linearly with the number of modes which have been significantly populated after the first Kapitza-Dirac. $\beta = V_0\Delta t/\hbar$ is what parametrize the strength of the Kapitza-Dirac pulse, and increasing β means increase the number of momenta components generated by the diffraction pulse.
However, as I pointed out in par.1.4, beyond the effective potential approximation, the KD

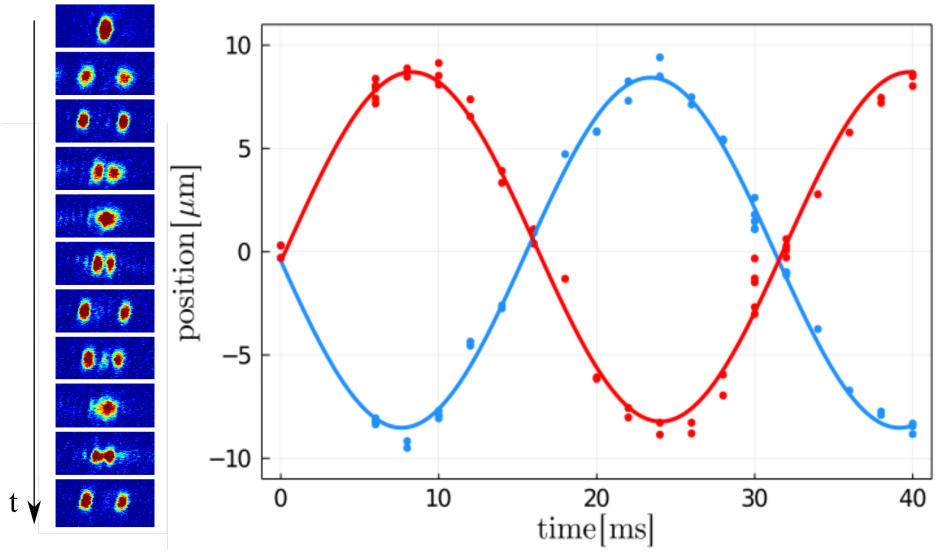

Figure 4.3: (left) In situ absorption images of the diffracted orders m =±1 during a complete oscillation; (right) corresponding positions as a function of time. Plot data are the outcome of individual measurements; we observe two sinusoidal oscillations with average frequency of $\omega = 2\pi\times31.7(0.8)$Hz and amplitude 8.6(0.6) μm obtained from the fit in the picture

pulses made with BNSL diffract atoms also at momentum components associated with the two fundamental optical lattices, i.e. at integer multiples of $2\hbar k_{1,2}$. The atoms of these components are effectively lost for the purpose of the interferometer: due to their large momenta, they are driven in the anharmonic region of the optical dipole trap (if not outside). So for BNSL increasing β means also reduces the total number of atoms contributing to the interferometer signal. In par.1.4 I considered as lost components with p$\geq 4\hbar k_{-}$. Anyway, now we have to consider also how far in the harmonic potential each component can travel before reaching anharmonic region.

Besides for the atoms in the "lost" large momentum components, the anharmonicity is a problems also for the "small" ones. The most obvious effect of the anharmonic trapping potential is that the oscillation period gets to depend on the energy, thus the spatial recombination after the half (or full) oscillation is imperfect, causing a decrease of the interference signal. In addition, the anharmonicity changes substantially the momentum distribution obtained at the interferometer output, as observed in numerical simulations where the trapping harmonic potential is deformed by a quartic anharmonic term [90]. Indeed, as mentioned in par.4.1, for a perfectly harmonic potential the phase gained by a wavepacket during multiple of half oscillation is zero. This is no longer the case for an anharmonic potential, where the phase acquired by each wavepacket during half oscillation is not zero and is not the same for all wavepackets.

In particular the confinement of the vertical beam (a focused Gaussian beam) can be considered harmonic around its minimum only for displacements much smaller than the beam size. To quantify this, as in [90], we have run numerical simulations to compare the outcome of the interferometer in a harmonic potential and in a Gaussian potential, approximately corresponding to the intensity profile of the laser beam $V_{\mathrm{Gauss}}(x) = -V_g \exp(-2x^2/w)$ where w=100μm is the waist and the potential depth V_g is adjusted to match the measured frequency of the small-amplitude oscillations. We calculate the overlap between the $0th$ and the nth diffraction orders after half oscillation, i.e. after half-period of the small amplitude oscillations.

Fig. 4.4 shows that, for the above Gaussian potential, the overlap drops for components with p>3$\hbar k_{-}$. Conversely, the overlap is nearly perfect when the atoms populate only p<2$\hbar k_{-}$

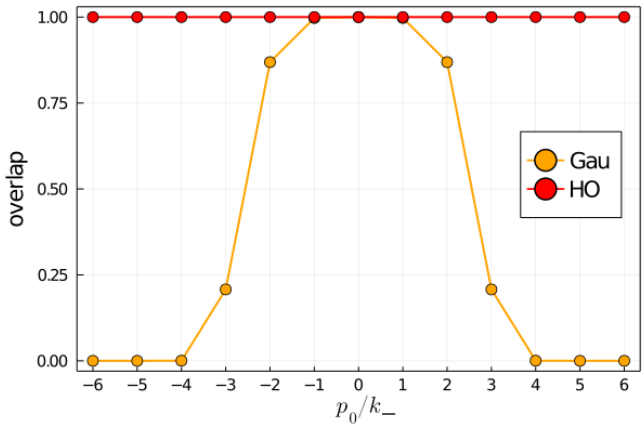

Figure 4.4: Overlap $|\langle\Psi_0(T/2)|\Psi_n(T/2)\rangle|$ of the wavepackets with initial momentum 0 and $n\hbar k_-$, at time t = T /2, i.e. after half period of small-amplitude oscillations: we compare the case of the harmonic oscillator with the Gaussian potential.

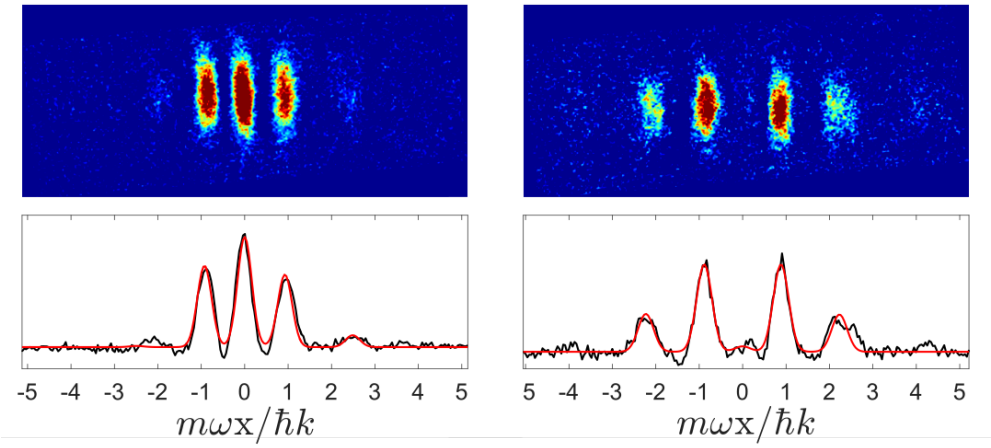

Figure 4.5: Absorption image (top) of the momentum distribution and corresponding integrated density profile together with the multi Gaussian fit (bottom) after the first KD pulse (left) and after the second KD pulse (right) for a time interval between the two pulses equal to half period, i.e., approximately 16 ms. In both cases a quarter period of in-trap evolution occurs between the last KD pulse and imaging

diffraction orders, like in our experiment, and it is unity at all orders for the harmonic potential, as expected. For this reason, and for the fact that we have to perform two KD pulses to close the interferometer, which means to double the losses, we work with components with $<2\hbar$k. Then, we set the KD pulse duration to 80μs in order to transfer almost 50% of the atoms in the m = ±1 orders and we shine the second KD pulse after a half (or full) period to complete the interferometric sequence.
We then image the different momentum orders after allowing an additional quarter oscillation in the trap to maximize their spatial separation. We get the atom number in each components, N_q, fitting the profiles with a multi-Gaussian function

$$f(\mathrm{k}) = \sum_{\mathrm{m}=-2}^{\mathrm{m}=+2} \mathrm{p}_0 \mathcal{J}_{\mathrm{m}}^2(\mathrm{p}_1) \exp\Big(-(\mathrm{k}_- - \mathrm{m})^2/2\mathrm{p}_2\Big) \tag{4.7}$$

with p_i, with i=0,1,2 being free parameters of the fit. The result is shown in Fig. 4.5

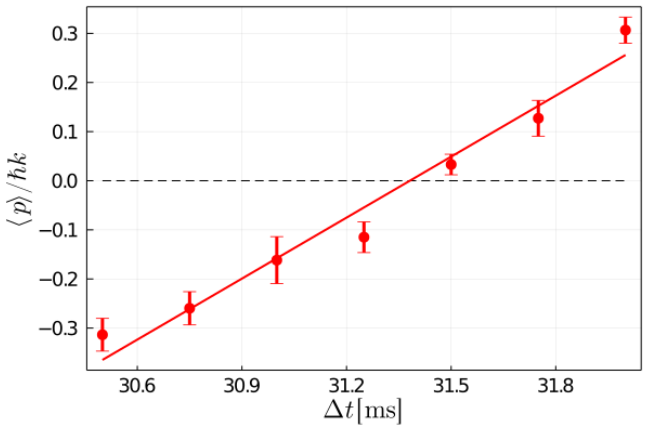

Figure 4.6: Average momentum at the output of the full-period interferometer as a function of the time separation between the two KD pulses, Δt. The fit parameter is the harmonic period, identified as the zero-crossing time: T = (31.38 ± 0.03) ms. The error bars indicate the standard error on the mean of repeated measurements (N∼5).

4.4 Calibration of the Interferometer

Fig. 4.5 is in agreement with Eq. 4.3, the final momentum distribution is an even function of q, independently of the phases for both the half- and the full-period interferometer, so the average of momentum $\langle p \rangle$ =0. This symmetry breaks if the time separation of the two KD pulses is not exactly half period, i.e., Δt = (1/2 + ϵ)T. In this case, the m-th momentum component acquires an extra phase, $\exp(i2\pi \mathrm{m} 2\mathrm{E}_{\mathrm{R}\_}/\hbar\omega)$, given by the classical action in the time interval between the KD pulses. It is possible to exploit this sensitivity to precisely determine the oscillation period, using the full-period interferometer that, as shown in par.4.1, it is insensitive to the relative displacement between the trap and the lattice (and thus to external forces). Then, the proper time separation Δt is that which yields a symmetric momentum distribution.
Fig. 4.6 shows that measuring the average momentum $\langle$p$\rangle$ as a function of Δt allows us to find the oscillation period with a precision of 10^{-4}. Then this value is used to set the time separation equal to T/2, in the half-period interferometer which is sensitive to external forces.
Another aspect that can be investigated thanks to full-period interferometer is the relative frequency stability of the two kD pulses. Indeed, Eq. 4.6 shows that, at the output of the full-period interferometer, the fraction of population at zero momentum equals $|\mathcal{J}_{\mathrm{m}}(2\beta \sin(\delta))|^2$. I can verify this relation by frequency shifting one of the two lattice before the second pulse, of a quantity $\delta \mathrm{f}_2 = \mathrm{c}\delta \mathrm{k}_2/2\pi$, which then modifies its phase ϕ_2 of $\delta\phi_2 = 2\mathrm{D}\delta \mathrm{k}_2$, where D is the distance of the atoms from the retroreflecting mirror. This in the end displaces the beat-note superlattice by $\delta \mathrm{x} = \delta\phi_2/(\mathrm{k}_1 - \mathrm{k}_2)$. By mean of in situ imaging I can calibrate the position of atoms trapped in the lattice minima as function of $\delta \mathrm{f}_2$, Fig. 4.7, and from the fit it results that $\delta x/\delta \mathrm{f}_2 = (10 \pm 1)\mathrm{nm/MHz}$.
So, I change the frequency of the second pulse and then counting the relative population of the p=0 moment component N_0/N, where N is the total number of atoms, at the output of the full-period interferometer.
As shown in Fig. 4.8 data are well in agreement with the predicted behavior.

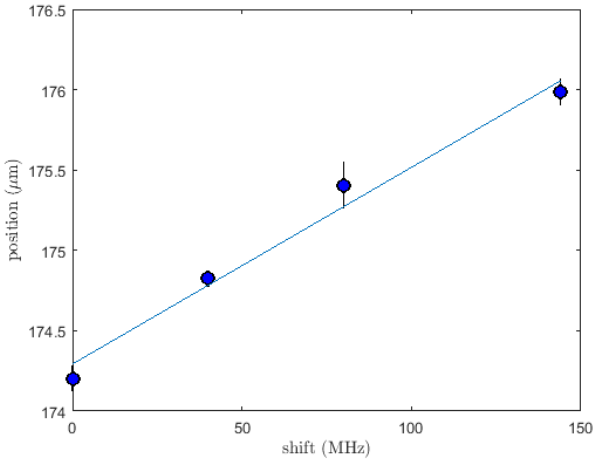

Figure 4.7: Calibration of the displacement δx of the BNSL minima as function of frequency shift δf_2

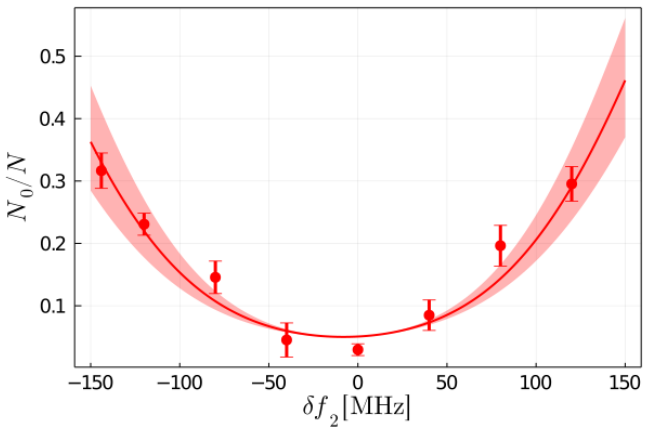

Figure 4.8: Fraction of atoms in m = 0 momentum component, N_0/N, at the output of the full-period interferometer as a function of the frequency shift of k_2 standing wave during the second KD pulse. The shaded band is the uncertainty due to the calibration of the beat-note superlattice displacement versus the frequency shift, i.e., (10±1) nm/MHz; the error bars indicate the standard error on the mean.

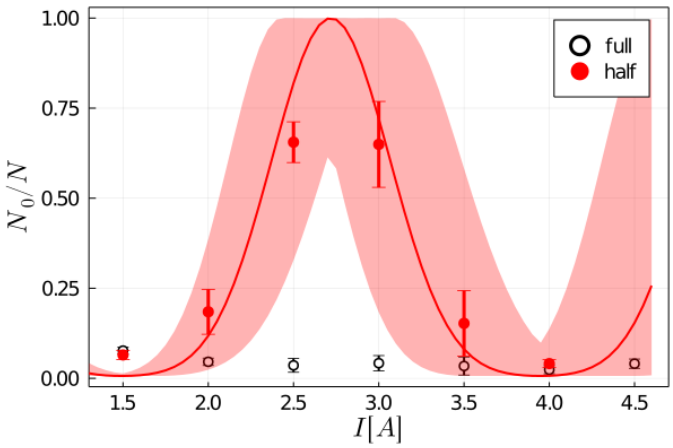

Figure 4.9: Fraction of atoms in p = 0 momentum component at the interferometer output as a function of the magnetic-gradient current, with a trap frequency $\omega = 2\pi\times31.7$ Hz for the half-period (red, solid points) and full-period (black, open) interferometer. The red line shows the theoretical prediction from Eq. 4.1, with $\beta = 1.12$ and an offset phase as fit parameters; the shaded band is the uncertainty of the displacement-versus-current calibration; the error bars represent the standard error on the mean.

4.5 Measurement of applied force

In Fig. 4.9 is reported the measure about of the relative population of the p=0 moment component N_0/N, where N is the total number of atoms, as a function of the coil current (full red points), with error bars corresponding to the statistical standard deviation for typically 5 repetitions of each data point. The peak identifying the configuration of zero force is not located at I = 0 due to the presence in our setup of a spurious magnetic field gradient that is cancelled by the gradient applied with a current I = 2.8 A.
Note, in Fig. 4.9 are also reported measurements with the full-period interferometer (black open points), showing that the N_0/N is constant within 0.017 (standard deviation).
The error bar at the maximum slope of the fit curve, yields a resolution for the half-period interferometer of ΔI=0.05 A. Being $a/\omega^2 = d = \eta I$, then it means a resolution of $\delta a = (2.19\pm0.26)\ 10^{-4}$g, where g is the gravity acceleration and the uncertainty is dominated by the error on the calibration factor η.
It is also possible to derive information about the interferometric phase (argument "arg" of cosine in $\mathcal{J}_0(2\beta\cos(\arg))$ in Eq. 4.1) from a fit of the populations of all momentum components, for each value of the applied force. According to Eq. 4.1 this phase is expected to depend linearly on the force, hence on the current (see Fig. 4.10).
The average error bar of these data is $\Delta\phi_m = 0.06\pi$, which mean an acceleration sensitivity of $\delta a = (\omega^2/k_-)\Delta\phi_m = 2.2 \times 10^{-4}$g, consistent with the one above. Comparing Δa with the sensitivity derived in [29] as the Cramer-Rao bound $\Delta a_{CR} = (\omega^2/\beta k)/\sqrt{8rN}$, with r number of repeated measurements and N total number of atoms, we can see how our resolution is close to the standard quantum limit. In our experiments $N\simeq5\cdot10^3$ and r is typically 4, which corresponds to $\Delta a_{CR} = 4\cdot10^{-6}$, a factor$\sim$40 smaller than our experimental δa.
A possible reason for this discrepancy is the pointing instability of the optical dipole trap beam which provides the harmonic confinement (th vertical beam). Indeed, any technical displacement of the trap minimum is indistinguishable from those induced by external accelerations; the interferometric sequence lasts only 16 ms but the sample preparation (dead time) takes approximately half a minute, and slow drifts of the ODT beams occur over this timescale.
The above discussion shows that lowering the harmonic frequency improves the resolution.

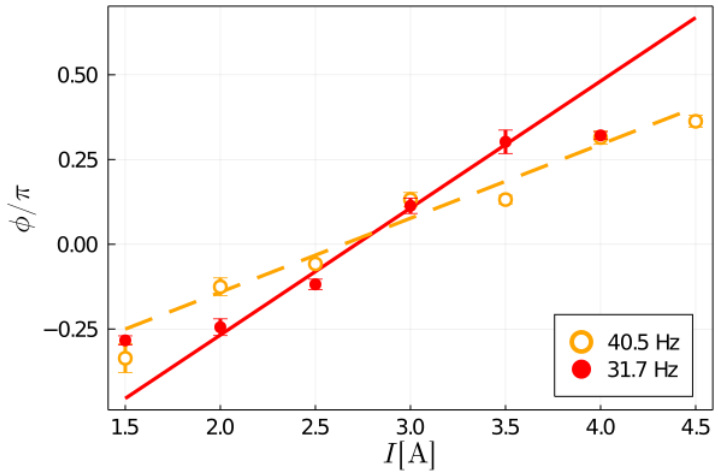

Figure 4.10: Interferometric phase ϕ derived from fitting the momentum fractional populations of momentum components with $\mathcal{J}_q^2(2\beta\cos(\phi))$, for harmonic frequencies equal to 31.7 Hz (red, solid points) and 40.5 Hz (orange, open); lines are linear fits with slopes (1.18 ± 0.09) rad/A (red, solid, excluding extreme points) and (0.68 ± 0.08) rad/A (orange, dashed). The error bars represent the standard error on the mean.

However, in our setup we can only marginally increase—and not decrease—the trapping frequency, to keep under control the anharmonicity of the potential. Thus, we repeated the measurement with $\omega = 2\pi\times(40.5 \pm 0.5)$ Hz and, as expected, the measured interferometric phase is less sensitive to the applied force (see Fig. 4.10).

4.6 Conclusions

We have performed a proof-of-principle demonstration of a multimode interferometer in a harmonic trap based on KD diffraction pulses. We have shown that external accelerations are detected from the displacement induced on the harmonic trap with respect to the KD lattice. With a relatively low number of atoms N=$5{\cdot}10^3$ and a harmonic frequency of approximately 32 Hz, we showed a sensitivity δa $\sim 2 \times 10^{-4}$g, a factor 40 away from the Cramér-Rao bound. Anyway, this work potentially represents an easy method to enhance the sensitivity of a trapped atom interferometer by enlarging the spatial separation between the modes involved. In particular this is done by reducing the harmonic trapping frequency, and increasing the number of momentum components with KD pulses of enhanced intensity and/or duration. But this can not be the case for an harmonic potential made by an optical trap like ours. In there, the oscillations of the largest momentum components are harmonic only if their amplitude A is much smaller than the beam's waist w, i.e. A= $q_{max}\hbar k_-/(m_a\omega) < w$, with $q_{max} \propto \beta$. This condition then constraints the achievable sensitivity.
The performance of this sensor could be enhanced using a harmonic magnetic confinement along the direction of the lattice, that is more stable in position than the ODT and features a harmonic region much larger. For example, using 10^5 atoms in a magnetic trap with frequency $\approx$1 Hz and with oscillation amplitudes of $\approx$1 mm, we expect an improvement of the sensitivity by several orders of magnitude, up to $\sim 10^{-8}$g. To avoid the problem of changes in interatomic interaction due to the presence of inhomogeneous magnetic field, a suitable option could be use spin-polarized fermionic atoms that, at low temperature, are naturally non-interacting, provided that the KD lattice spacing is chosen smaller than the coherence length of the atomic sample [91].

Chapter 5

Trapped Atom Mach-Zehnder Interferometer

In this chapter I will describe the realization of a linear Mach-Zehnder interferometer (MZI) with Bose Einstein condensates optically trapped in an array of double well potentials. I realize such array with the Beat Note Super Lattice (BNSL) technique described in par. 1.3.3. In Fig. 5.1 I show a complete MZI interferometric sequence for a single double well potential with modes spatially separated by a distance d.

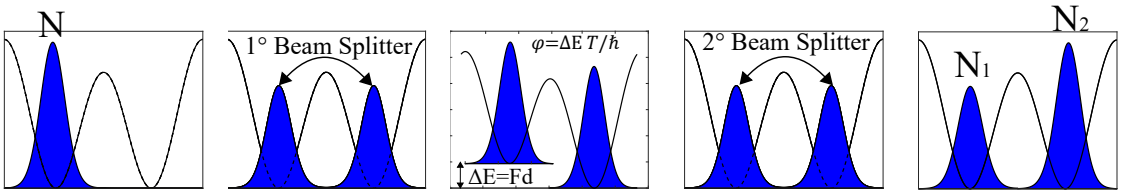

Figure 5.1: Mach-Zehnder interferometric sequence with a BEC in a double-well.

A state is prepared in a single mode, that for our double well potential correspond to one of the two localized spatial modes. A 50:50 beam-splitter is provided by lowering the barrier and letting the state evolve under the non interacting term in the Bose-Hubbard Hamiltonian Eq. 1.43 for a given amount of time, to have a coherent population of both modes with the same probability. In a similar way, one can also start with all the atoms at the bottom of the trap, and raising up the barrier to split the cloud in two.
Then, after the tunnelling between the two modes is cancelled, a phase difference ϕ is accumulated during the interrogation time T applying an energy imbalance ΔE between the two modes. A second beam splitter remaps the information about the relative phase into the atom number difference $z = \frac{N_1 - N_2}{N}$, that is an observable of our system.
Note, another way to give an accurate determination of the phase is to release the trapped separated clouds, letting them overlap and studying the interference fringes [92]. However, the goal of this work is to realize two or more identical double wells and make them working simultaneously as independent and correlated MZI. Having more than one correlated atomic sensor is useful, since it allows to perform a differential analysis to subtract the common noise acting on the system, which otherwise would increase the uncertainty of the measurement. This is basically how an atom gradiometer works, like the gravity-gradiometer employed for the determination of the Newtonian gravitational constant G [93] or for Quantum tests of the equivalence principle [94].
For all these reasons we can't turn off the trapping potential, because it would require us to retrieve the phase difference from the interference pattern of four or more condensates, which is actually too difficult, if even possible.

For each double well, we rather count the atom number difference at the end of the second beam splitter, which is an observable we can measure thanks to our high resolution imaging system.
In the first part of this chapter I analyse aspects of the BNSL double well array such its dependence on the frequencies of the three lattices that compose it. I explain how experimentally can find the right phase relation between the three lattices to get the BNSL double well array, and how the system responds when the commensurability condition which characterize the BNSL is not perfectly fulfilled.
To get knowledge about the energy scale that characterizes the system and to verify that the dynamic in the three double wells is the same, I show examples of Rabi oscillations between the modes of each double well.
Once convinced that the three double wells are identical, I perform a complete MZI. Preliminary results show some degree of correlation between the outputs of the three sensors, which tell us we are on track for the realization of an operative trapped atom gradiometer.
On such data I also show an example of differential analysis. Finally in the last paragraph I present some data about noise reduction in the state preparation exploiting repulsive interactions.

5.1 Double Wells Array characterization

In par.1.3.3 I show that the direct sum of three optical lattices $V_B^{1,2,3} = \sum_i V_i \sin(k_i x + \phi_i)^2$, with commensurate wavelengths $(n+1)\lambda_1 = n\lambda_2$ and $(n-1)\lambda_3 = (n+1)\lambda_1$, with $n \gg 1$ is equivalent, for low depths, to an effective double well array potential $V_{\text{eff}}^{1,2,3}(x)$. To get this latter, the choice of the lattices phases ϕ_i is important, in particular we need $\phi_1 = \phi_2$ and $\phi_3 = \phi_2 + \pi/2$.
The three wavelengths are $\lambda_1 = 1013,751$nm, $\lambda_2 = 1064,439$nm and $\lambda_3 = 1120,462$nm, with n=20.
From the experimental point of view to check the condition on the phase, what I did is to load the BEC in two different 10μm spacing BNSLs, $V_B^{1,2}$ and $V_B^{2,3}$ (see Eq. 1.48), and register on the camera the different in-situ positions of the atomic clouds (i.e. the minima of the potential). The proper phase relation is obtained when the relative distance between the minima of $V_B^{1,2}$ and $V_B^{2,3}$ is 5μm, i.e. when they are in counter-phase. To find such condition I change the frequency of the λ_1 laser in a range of about 300 MHz to shift the position of the minima as much as I need, in agreement to what I said in par.2.5.

5.1.1 Frequency dependence of a balanced double well array

Once we get the double well configuration, the first issue is how well we have to satisfy the commensurability conditions. Knowing the effect of a deviation of the wavelengths from the commensurate condition is mandatory to understand the requirements on the laser frequency accuracy and stability.
In our working condition $d_- \sim 10.64$ μm, and for the numerical calculation shown in Fig. 5.2, I take $V_1 = V_2 = 1.6E_{R_2}$, $V_3 = 0.9E_{R_2}$ and a deviation of k_3 by the commensurability condition of $\epsilon \sim 10^{-5}k_3$ (i.e. a discrepancy on the wavelength λ_3 of 0.01 nm).
In Fig. 5.2a,b and Fig. 5.2c,d I show how the system responds in a different way to the sign of ϵ: while the central double well is centred, the neighbouring ones feel an anti-confining (a,b) or confining (c,d) potential when ϵ is positive or negative respectively. A energy mismatch δ between the minima of the neighboring double-well occurs, whose sign also depend on the sign of ϵ.
In Fig. 5.2e an in-situ image of the BEC loaded in a non perfectly commensurate BNSL array of double well is reported. An anti-confining behaviour far from the balanced central well is observed.
Fig. 5.2f show exact numerical calculation of δ as function of double well position $x = l d_-$, with l integer. The fact that δ is linear with l tells us that such imbalance can be described by an harmonic potential of frequency $\omega = \sqrt{\frac{2h\delta}{m_a d_-^2}}$, where m_a is the atomic mass.
Since all those effects can be described thanks to the shift a single parameter, it means that we can compensate them by accordingly changing it. Thus, what I do experimentally is measure the population imbalance (relative atom number difference) in the three double wells $z_i = \frac{N_{Li} - N_{Ri}}{N_i^{tot}}$ (i=1,2,3) as function of k_3, where $N_i^{tot} = N_{Li} + N_{Ri}$ is the total number of atoms of i-th double well and N_{Li}, N_{Ri} are the number of atoms in its left and right mode respectively.
I start loading the BEC in the 10μm spacing BNSl made by the k_1 and k_2 lasers with no interaction. $V_1 \sim 400$nK and $V_2 \sim 350$nK, so the trapping frequency inside a BNSL site is around 200 Hz. Then, I turn on the third laser k_3 with a slow linear ramp (∼200 ms) to be more adiabatic as possible, up to a value $V_3 \sim 200$nK. In this way, ending closer to a ground state with little tunnelling energy J, I am more sensitive to the presence of an energy imbalance δ between the left/right modes, cause for the ground state it will be more favourably populated the mode with lower energy.

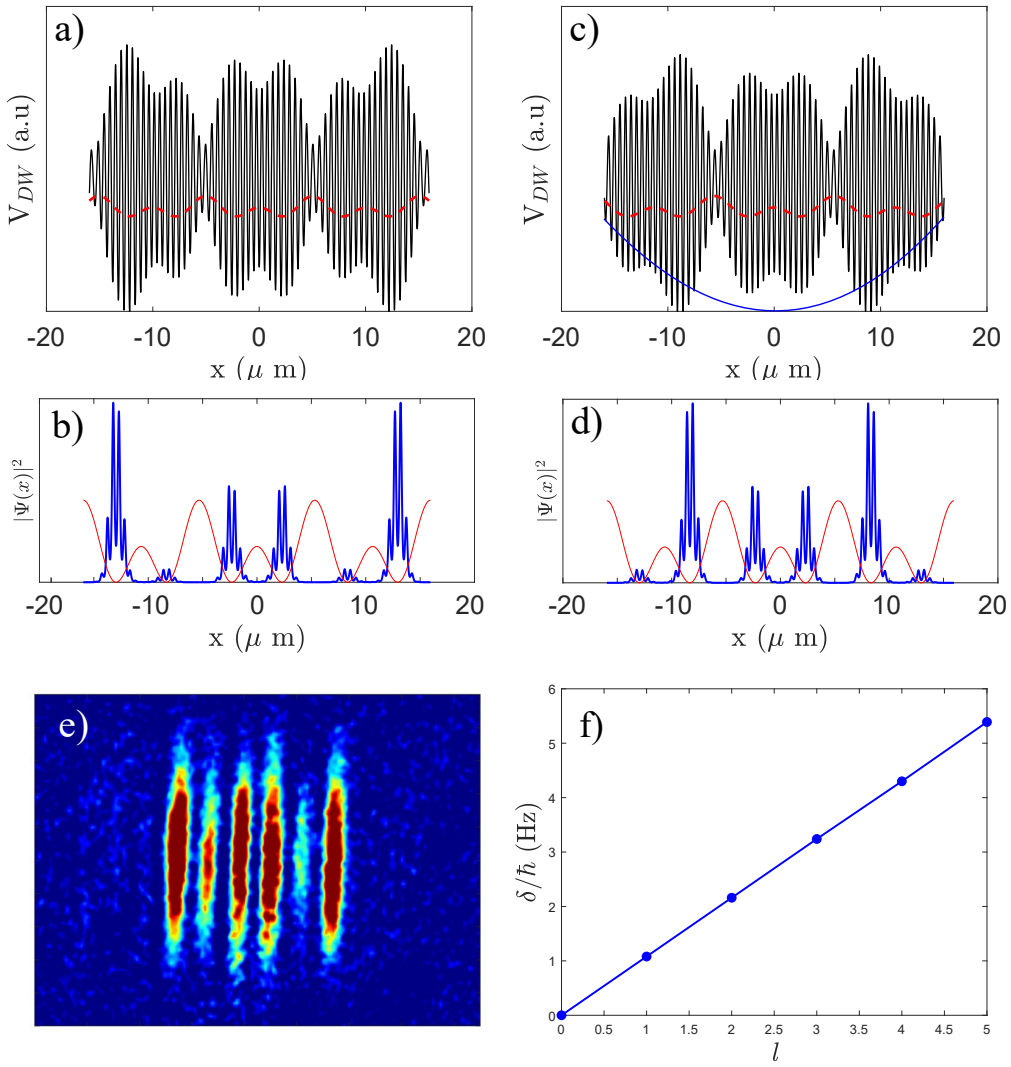

Figure 5.2: 1D numerical simulation for three BNSL double wells with $V_1 = V_2 = 1.6E_{R_2}$ and $V_3 = 0.9E_{R_2}$, with a) $\epsilon \sim 10^{-5}k_3$ and b) relative probability density distribution. The red-dashed line in a) represents the effective double well potential $V_{eff}^{1,2,3}(x)$, while the solid blue line depicts the presence of an anti-confining harmonic potential on the system.
In c) and d) I calculate the case with $\epsilon \sim -10^{-5}$k3, which on the contrary shows the presence of a confining harmonic potential.
In e) is reported an in-situ image of the BEC loaded in a non perfectly commensurate BNSL array of double well, which shows, in analogy with b), an anti-confining behaviour far from the central well. The atoms are let expand without radial confinement for about 8 ms, which is why the spatial modes assume a cigar shape.
In f) I plot some numerical calculation of δ as function of the double well site l.

The two TA-pro Toptica lasers (the ones we use to generate k_1 and k_3 lattices), are tunable over a range of few nm, so we can exploit them to change the wavelength of order of 0.01 nm. Needless to say that, after every shift in the wavelength we need to re-lock our laser to the reference cavity (par.2.5.2)and find again the condition where the central double well is balanced. Only after this we can check if the shift we made was sufficient or not.
In Fig. 5.3a) some traces of imbalances z_i at different values of the shift in λ_3 are reported, in particular from above to below the total reduction in λ_3 is about 0.06 nm. As one can see, at the beginning only the mean value of the imbalance of the central well is around z_2=0

(balanced double well), while for the two neighbouring ones the mean values of the imbalances $z_{1,3}$ are far from the zero and opposite in sign, as expected looking at Fig. 5.2e). As the λ_3 decreases, the three mean values get closer and closer, until the three of them oscillate around z=0. In Fig. 5.3c) it is shown an in-situ image of the BEC loaded in the BNSL array of double wells when the effect of the non commensurability is almost cancelled.
Note that in the last picture of Fig. 5.3a) the three traces of the imbalances are almost completely coincident, meaning that not only we managed to compensate the effect of the fictional harmonic potential, but also that shot to shot the three double wells feel the same noise on z_i. This clear correlation in the imbalance fluctuation of the three double wells is the feature we need to start to build our Mach Zehnder gradiometer.
However the population noise in Fig. 5.3a) is remarkably large, something we should work on in the nearly feature (beyond the work of this thesis). In particular, main sources of noise in our system are the fluctuations of the frequency (so the phase) of the lattices and the vibration of the retroreflecting mirror. Both of them are sources of common noise and, fortunately, something we can work on with techniques already known in the field of interferometry. Other sources more difficult to identify and study can be spurious magnetic gradient, instability in the magnetic field and defects of the intensity profile of the laser beams.
About the fluctuation of the phase, it depends on the performance of the frequency-lock system. Regarding the latter, it is worth spending a few words about how a drift of the optical cavity implemented in the lock (see par.2.5.2) affects the balancing of the three double wells.
Suppose we respect the commensurability condition completely, i.e the three wavelength are $\lambda_1 = \frac{n}{n+1}\lambda_2$, λ_2 and $\lambda_3 = \frac{n}{n-1}\lambda_2$. If the three λ_i are locked to the same reference cavity then $\lambda_i q_i = 2L$, with i=1,2,3 and where q_i represents a distinct fundamental cavity mode.
As discussed in chap.2.5, if the cavity changes its length L then the wavelength λ_i of the laser will change accordingly, i.e. $\Delta\lambda_i/\lambda_i = \Delta L/L$. Then it's easy to show that

$$\begin{aligned}
\tilde{\lambda}_2 &= \lambda_2\left(1+\frac{\Delta L}{L}\right)\\
\tilde{\lambda}_1 &= \frac{n+1}{1}\lambda_2\left(1+\frac{\Delta L}{L}\right)\\
\tilde{\lambda}_3 &= \frac{n}{n-1}\lambda_2\left(1+\frac{\Delta L}{L}\right)
\end{aligned} \tag{5.1}$$

So, the new frequency $\tilde{\lambda}_i$ still fulfil the commensurability condition we need to get our array of double well. Now we need to be sure that also the conditions on the phases ϕ_i of the three lattice are still satisfied.
In par.1.3.3 I showed, that I need $\phi_1 = \phi_2$ and $\phi_3 = \phi_2 + \pi/2$ to get a balanced double well array. This is a particular case which help to handle the analytic description of the BNSL. More in general, always referring to Eq. 1.58, we could say that we need

$$\begin{aligned}
\phi_1 - \phi_2 &= \alpha\\
\phi_2 - \phi_3 &= \alpha - \pi/2\\
\phi_1 - \phi_3 &= 2\alpha - \pi/2
\end{aligned} \tag{5.2}$$

If D is the distance of the atoms from the mirror, then $\Delta\lambda_i$ lead to $\Delta\phi_i = 2D\Delta k_i = 2D\frac{\Delta L}{L}k_i$. So from Eq. 5.2 we get

$$\begin{aligned}
\Delta(\phi_1 - \phi_2) &= 2D\frac{\Delta L}{L}(k_1 - k_2) = 2D\frac{\Delta L}{L}\frac{k_2}{n} = \beta\\
\Delta(\phi_2 - \phi_3) &= 2D\frac{\Delta L}{L}(k_2 - k_3) = 2D\frac{\Delta L}{L}\frac{k_2}{n} = \beta\\
\Delta(\phi_1 - \phi_3) &= 2D\frac{\Delta L}{L}(k_1 - k_3) = 2D\frac{\Delta L}{L}2\frac{k_2}{n} = 2\beta
\end{aligned} \tag{5.3}$$

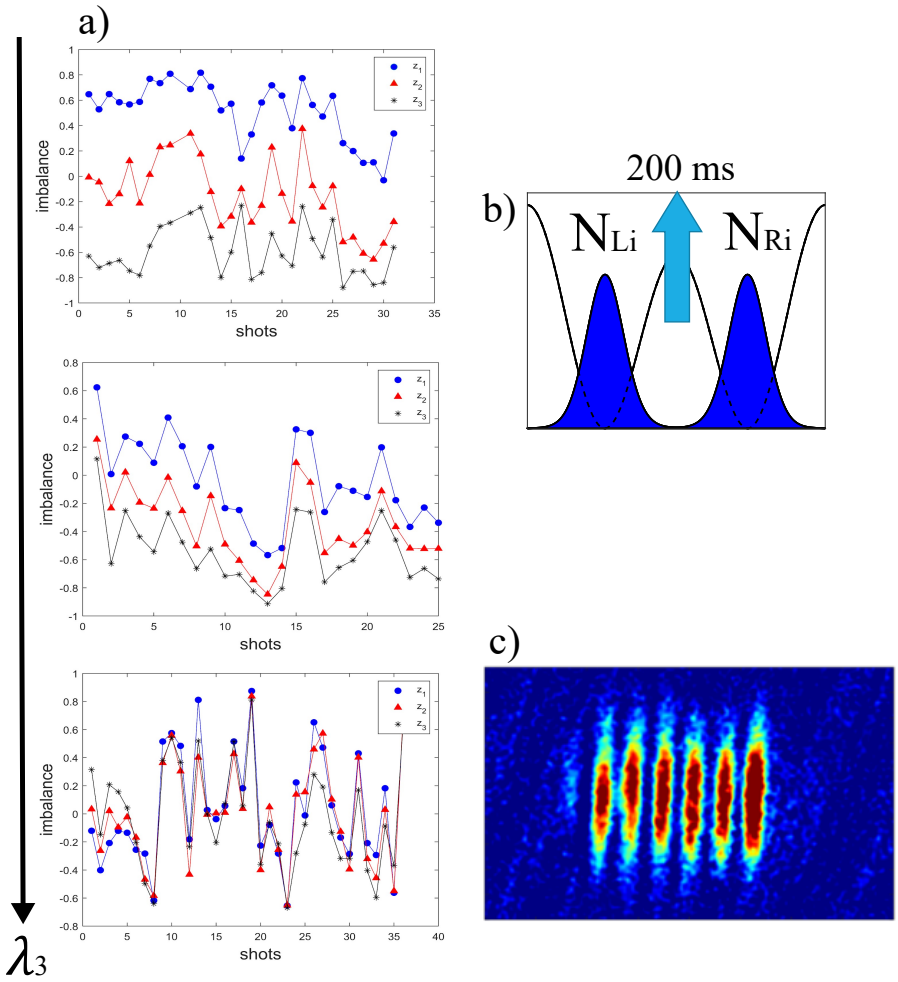

Figure 5.3: a) traces of the three imbalances z_i as function of experimental repetitions (shots) of the splitting procedure in figure b). From above to below a) shows how the mean values of the three imbalances get closer as λ_3 decrease, up to the point that we can observe correlation in the imbalance fluctuation z_i.
In c) is shown an in-situ imaging (the atoms are only released in radial direction for about 8 ms) of the BEC loaded in the BNSL array of double wells when the effect of the non commensurability is almost cancelled.
Here "shot" stands for the a single output after a whole experimental procedure, which start with realization of the BEC and end with the absorption imaging.

So, it seems that a drift of the locking cavity only changes the value of α in Eq. 5.2. So if the phases initially provide balanced double wells, they still do it after a change in L.
For all those reasons we can conclude that our configuration seems to be insensitive to any cavity drift.

5.1.2 Rabi Frequency

Consider the Bose-Hubbard Hamiltonian in Eq. 1.43, $H = \frac{E_c}{2}N^2\frac{z^2}{4} - E_J\sqrt{1-z^2}\cos(\phi)$, where the coefficients refers to the Eqs. 1.36. For small interactions, we can simplify the tunnelling term $E_J = JN/2$, where J is energy difference between the two lowest symmetric and antisymmetric states. Then Bose-Hubbard hamiltonian reads

$$H = \frac{E_c}{2}N\frac{z^2}{2} - J\sqrt{1-z^2}\cos(\phi) \tag{5.4}$$

where we have rescaled by a factor N/2 the whole Hamiltonian. From the equations of motion $\frac{dz}{dt} = \frac{dH}{d\phi}$ and $\frac{d\phi}{dt} = -\frac{dH}{dz}$ for non interacting atoms ($E_c = 0$) we get a couple of equations in z(t) and ϕ(t) which describe sinusoidal oscillations of the parameters with a Rabi frequency $\Omega_{Rabi} = J/\hbar$, and average value of the imbalance $\langle z(t) \rangle = 0$. So, exploiting these oscillations we can get directly knowledge about the tunnelling energy of the system, which is fundamental to realize the linear beam splitter steps in the Mach-Zehnder interferometer.
In Fig. 5.4 two examples of Rabi oscillation of a non interacting BEC loaded in the three double wells are reported .

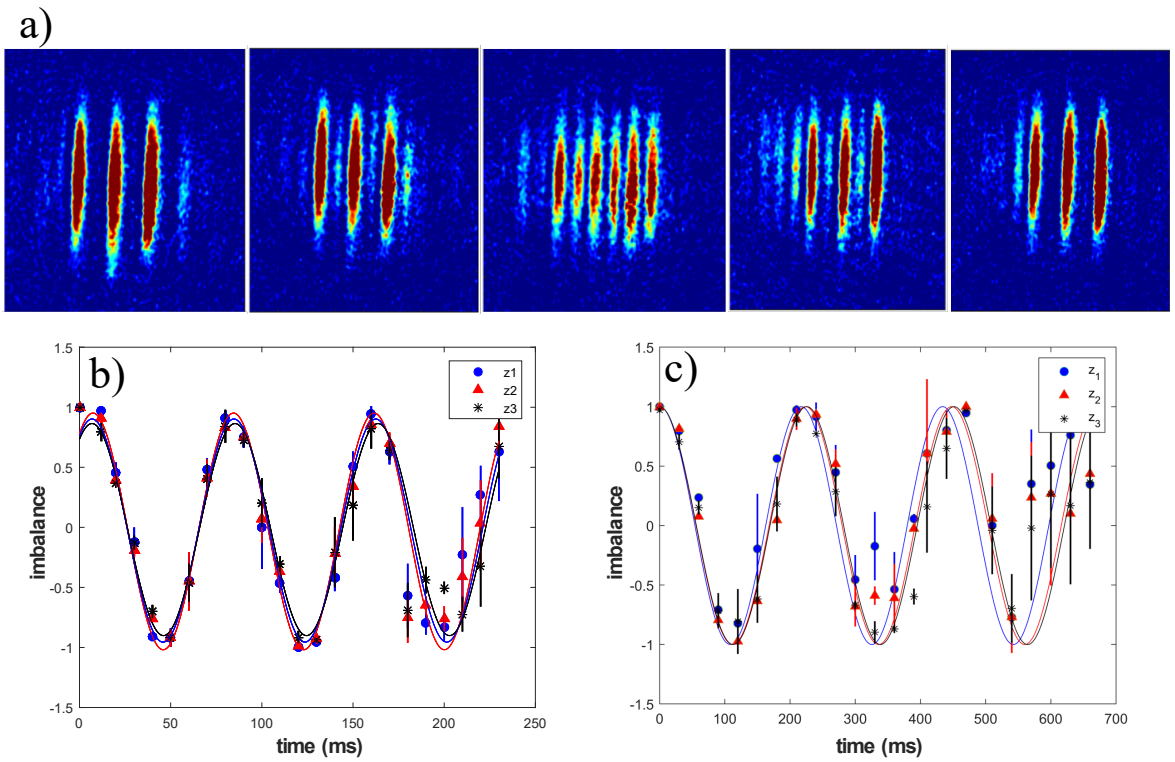

Figure 5.4: a)In-situ imaging (atoms are only released in radial direction for about 8 ms) of BECs loaded in three double well undergoing Rabi oscillation. From left, in each double well atoms start from the left mode (z=1) and tunnel through the barrier ending in the right mode. Below are reported two oscillation at a) ∼13 Hz and b) ∼4.3 Hz.

The method used to drive oscillations of the population between the two modes of the three double wells is the following.
After the evaporation we set the scattering length to zero ensuring a non-interacting BEC; then we load the atoms in three sites of the 10μm spacing BNSL made by lasers k_1 and k_2 (to do this we have optimized the shutdown of the IPG laser, which gives the confinement in the BNSL direction). After that, we increase the depth V_3 of laser k_3 with a phase shift in order to create an energy mismatch between the two modes and a population difference of about $z = 1$ in each double well; finally to drive the oscillations of z_i we set V_3 to a value with finite tunnelling and suddenly balance the three double-wells.
Population imbalance z in each double well is derived by fitting the density distribution of images in Fig. 5.4a with two Gaussian functions having the same width and different amplitudes P_L and P_R. Then $z=(P_L - P_R)/(P_L + P_R)$. In this way it is possible to reconstruct the oscillation of the imbalance and extract the tunnelling frequency fitting it with a sinusoidal function, Fig. 5.4b,c. We manage to observe synchronous oscillations of three imbalances for two different frequencies, meaning that the coherent dynamic in the three double well is pretty much the same.

Note that, for interacting particles the energy scale of the system is settled by the plasma frequency in Eq. 1.38, which defines also the oscillation frequency of z and ϕ. The frequency increases for a positive value of the scattering length and has a critical decreasing for attractive interactions, due to the presence of a quantum phase transition characterized by parity symmetry breaking [95, 54]. Also, in contrast to the non-interacting case, the oscillation frequency depends on the initial value of the population imbalance z_0. When $|z_0|$ is larger than a critical imbalance [17], then the initial interaction energy $\frac{E_c}{2}N\frac{z^2}{2}$ in the Hamiltonian Eq. 5.4 becomes larger then the tunnelling energy J, and the system cannot reach the balanced z=0 configuration due to energy conservation, showing the occurrence of the so called Macroscopic quantum self-trapping. So, the fact in that we are able to see a complete inversion of population even for small tunnelling energy in Fig. 5.4c, with roughly $\sim 4 * 10^3$ atoms in each double well, is proving that interactions in our system are almost cancelled.

5.2 Complete Mach-Zehnder sequence

We start loading the non interacting BEC in three sites of the 10μm spacing BNSL made by lasers k_1 and k_2, as explained in the previous paragraph, with depths $V_1 = 350 \pm 10$nK and $V_2 = 400 \pm 10$nK respectively, i.e. a trapping frequency within the single site of about 212 ± 3Hz. Those values follow from the calibration of the BNSL depth via in sito center of mass oscillations, as explained in chap.3.

First beam splitter

We perform the first beam splitter step of the Mach-Zehnder sequence increasing the power of the third laser k_3 (the barrier) with a phase which assure a balanced (z=0) configuration and up to a value that provide negligible tunneling.
Note that, unlike from Fig. 5.1, in our first beam splitter we don't start with z=1 and don't equally populate the left and right mode lowering the barrier for a time T_s, exploiting Rabi oscillations. The reason behind this choice is that directly splitting the condensate raising up the barrier as fast as possible help to be more insensitive to the external noise.
Indeed, external noise introduce energy imbalance δ between the left and right mode of each double well. To parametrize it we can add an extra term in the Bose-Hubbard Hamiltonian with $\phi = 0$ (for now we take the non interacting case).

$$H = -J\frac{N}{2}\sqrt{1 - z^2} + N\delta z \tag{5.5}$$

The presence of an energy mismatch δ changes the ground state of the system, making more favourable for the atoms to populate only the spatial mode with lower energy, left or right depending on the sign of δ. This means that, if I ramp up the barrier adiabatically to end near a state with negligible tunnelling, I will have a final population imbalance near ± 1.
The idea is then to perform a splitting fast enough to broke the adiabaticity, so that we don't reach the ground state with $J \approx 0$ but we froze the population of the two modes to have z=0 as final configuration. Of course we are limited in the rapidity of this procedure by the excitation of the system, since the depth of the initial 10μm spaced BNSL set the energy separation of the two lowest states from the excited ones. According to simulations, we can't ramp faster than 10 ms.
In Fig. 5.5 imbalances fluctuations of three z_i after the splitting with a slow ramp (T_s = 200ms) and a faster one (T_s = 10ms) are reported. The fluctuations after 10 ms, as expected, are lower than that after 200 ms.
We can look now at the dynamical effect of this noisy term δ.

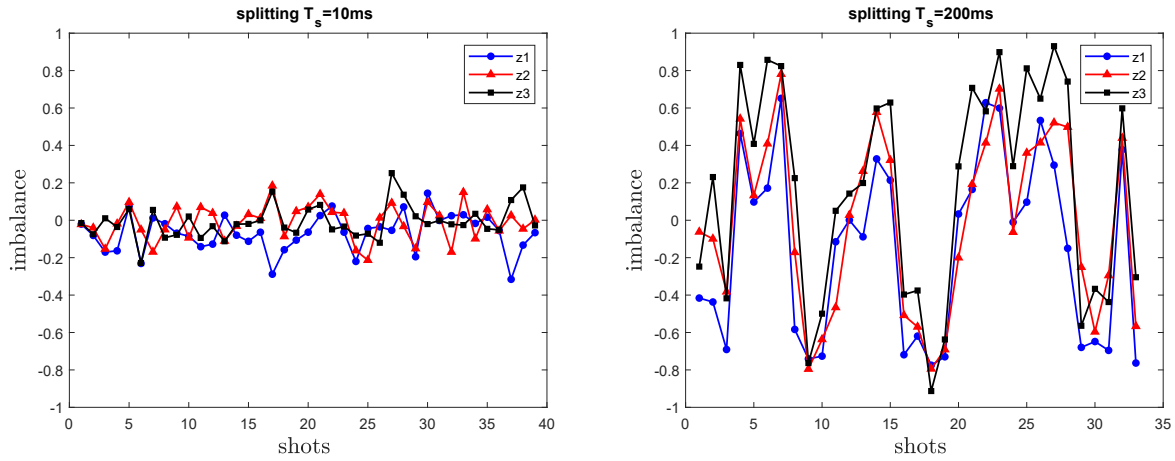

Figure 5.5: Comparison of fluctuations of three z_i after the splitting with a slow ramp (T_s = 200ms) and a faster one (T_s = 10ms).

After the first beam splitter, tunnelling is negligible, and the state can be described by a linear combination of Fock states $|n\rangle = |\frac{N}{2} - n\rangle_L |\frac{N}{2} + n\rangle_R$ [96], where the relation between n and z is always n=Nz/2:

$$|\Psi\rangle = \sum_{n=0}^{N} \mathcal{N} e^{-\frac{n^2}{2\Delta n^2}} |n\rangle \tag{5.6}$$

where $\mathcal{N}$ is a normalizing factor and $\Delta n = \sqrt{N}/2$ is the width of coefficients distribution centred at n=0 (this is the shot noise limit we met in par.1.2).
The only term left in the Bose-Hubbard is $2\delta n$, which is diagonal on the basis $|n\rangle$, so the evolution operator will be $U(t)=e^{i\delta nt/\hbar}$, where δ chances from experiment to experiment. Because of this, during the interrogation time the phase relations between the states $|n\rangle$ are lost (i.e. we have dephasing). In the end, because of the noise, interrogation time is limited by $T < \hbar/\delta$.

Second beam splitter

The second Beam splitter is realized exploiting the Rabi oscillation between the left and right modes of each double well. In Fig. 5.6 it is shown how the barrier depth is changed as a function of time to get a final imbalance of $z \approx 0$, starting with all the atoms loaded in the left mode (z=1).
Again, to avoid exciting the system, we don't change the barrier depth too fast but with two subsequent smooth ramps of about 10 ms each. During the first 10 ms I lower the barrier letting the tunnelling increases, and then I raise it up again with the same velocity. Experimentally, after setting the lower value of the barrier depth, I finely change the lowering/raising time T_{bs} looking at the output imbalance. In Fig. 5.7 are shown the imbalances z_i at the output of the procedure schematized in Fig. 5.6.
Once we optimize the T_{bs} we can implement this beam splitter to follow the first one after an interrogation time T and so complete the Mach-Zehnder interferometer. Note, our sequence has a minimum duration of 30 ms due to the finite time we need to perform the two beam splitter.

Read out

In Fig. 5.8 I report the latest measurements of the output of a complete Mach-Zehnder interferometer for a BEC loaded in three BNSL double wells. Each trace refers to a dif-

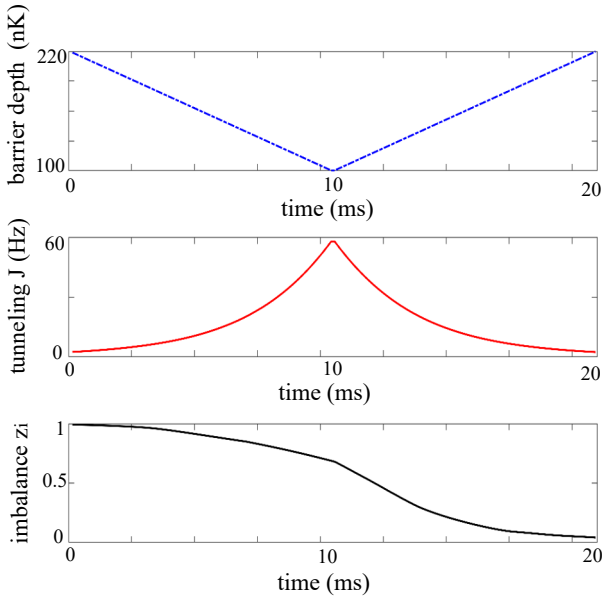

Figure 5.6: Numerical simulation of the Second Beam splitter. Barrier depth is changed as function of time, and the tunnelling change accordingly. Final imbalance is z=0.009.

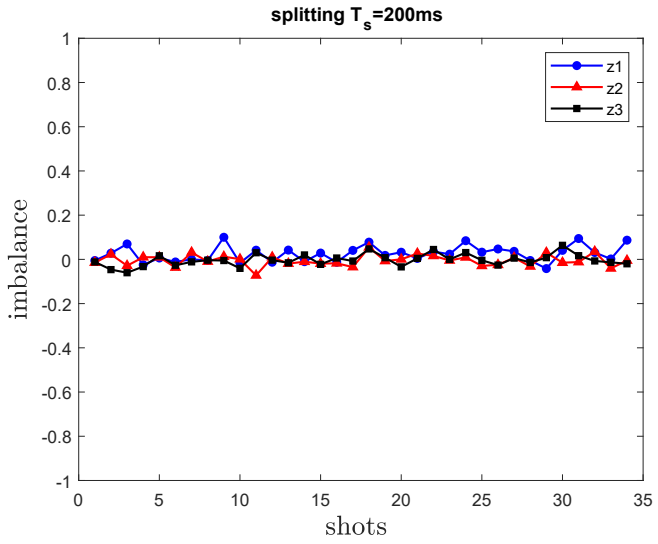

Figure 5.7: Fluctuations of three z_i after the Beam splitter of Fig. 5.6

ferent interrogation time T=0,20,50,100,200 ms which separate the two beam splitter steps. None external force F is applied during time T. The purpose of these preliminary measures is studying the coherence time of this sensor, and try to get information about entity of the noise acting on it.

First point to remember is that the fluctuations on the observables z_i at the output of the interferometer are due to phase fluctuations $\Delta\phi_i$. Ideally speaking, with no energy imbalance applied during the interrogation time T, i.e. no phase accumulation ϕ_i, the three imbalances $z_i = \sin\phi_i$ after the read out should be stay around z=0. Instead even for T=0, which means performing the two beam splitters with no delay in between, we can observe a large noise. This means that in 30 ms, which is the time we need to make the two beams splitter in a row, noise is sufficiently large to cause dephasing.

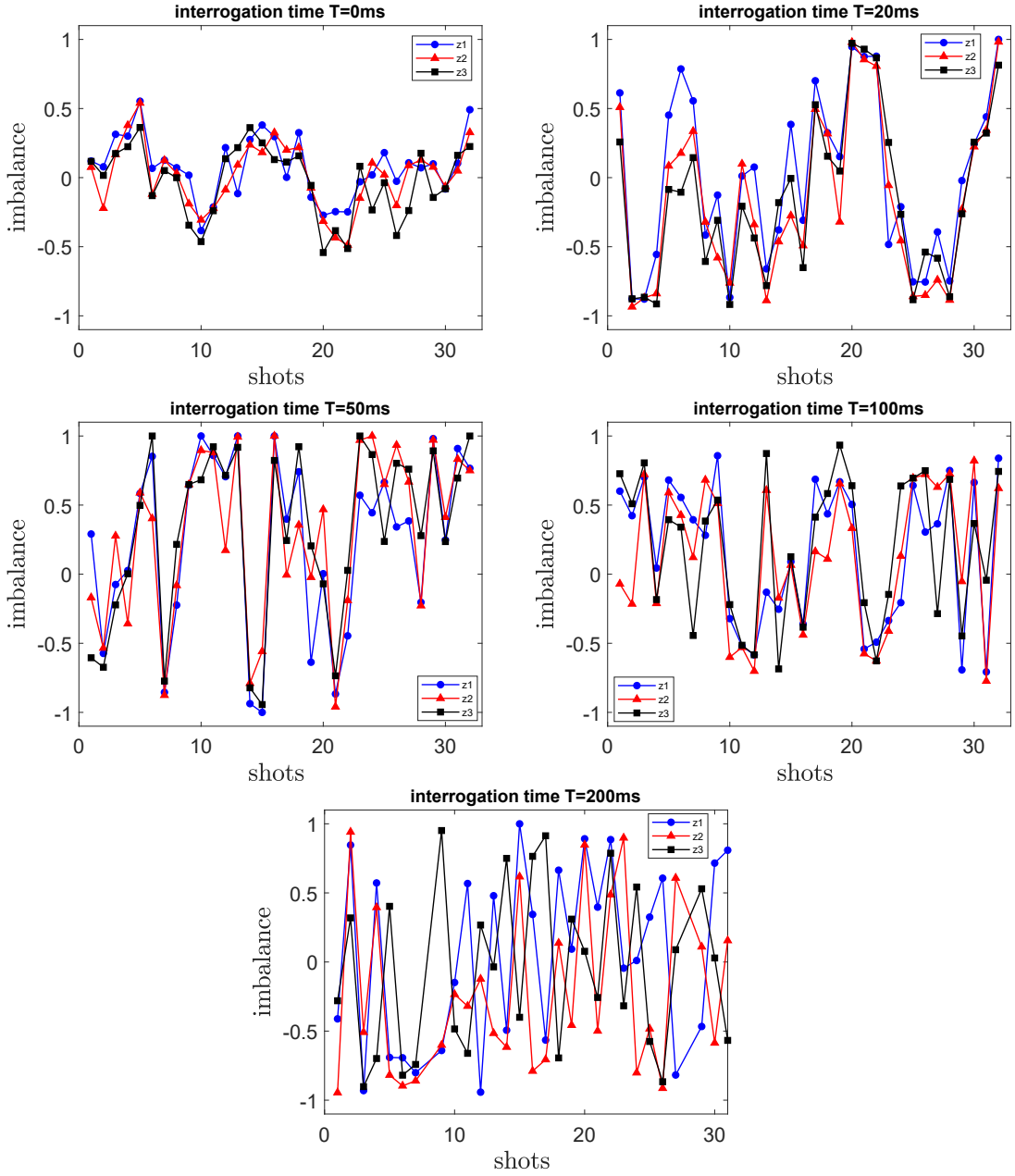

Figure 5.8: Fluctuations of three z_i after the the whole Mach-Zehnder sequence for different interrogation time T. We measure large phase noise even for short T, but we also observe some degree of correlation between the three independent z_i.

For T>0 phase noise is large enough to make the observables z_i assumes all values in [-1,1]. Good news is, that we observe correlations between the outputs of the three double wells, persisting for tens of ms of interrogation times. This means we can try to make the three sensor work simultaneously and perform differential analysis to subtract the common noise affecting them.

5.3 Differential Analysis

Let's focus on the outputs z_1 and z_2 of only two double wells after a Mach-Zehender interferometer sequence. Since in Fig. 5.8 interferometers output look correlated, we can describe the phase accumulated by each one of them as $\epsilon + \phi_i$. Here, ϵ is the phase term due to

common noise δ, while ϕ_i is the interferometric phase. Lets focus on only a couple of them, z_1 and z_2.

$$\begin{aligned} z_1 &= \sin(\epsilon) \\ z_2 &= \sin(\epsilon + \Delta\phi_{1,2}) \end{aligned} \tag{5.7}$$

For simplicity, I introduce in this description the phase difference $\Delta\phi_{1,2} = \phi_1 - \phi_2$. Eq. 5.7 are the parametric equations of an ellipse in the plane z_1 and z_2. In this picture, the role of ϵ is to place data points around the ellipse, whose ellipticity is instead a function of $\Delta\phi_{1,2}$.
The idea is then plot z_1 vs z_2 and, and to make an elliptic Fit to derive $\Delta\phi_{1,2}$. As said at the beginning of this chapter, in the MZ double well interferometer $\phi_i = \Delta E_i T/\hbar$, where ΔE_i is the energy difference between left and right mode of i-th double well (the physical quantity we want to measure) and T is the interrogation time. Then $\Delta\phi_{1,2} = (\Delta E_1 - \Delta E_2)T/\hbar$, so we expect that the ellipticity grows with time T.
In this description we don't take into account the uncorrelated sources of noise which, unlike ϵ, spread data point in whole z_1 z_2 plane, increasing the error on the fit we want to perform.
In Fig. 5.9 I show the output (red dot) z_1 (left double well) as function of z_2 (central double well) and z_3 (right double well) as function of z_2. Each trace refers to different interrogation times T=0,20,50,100,200 ms.
At T=0, $\Delta\phi_{1,2} = 0$ so we don't expect an ellipse, but a linear dependence of the two outputs. For T$>$ 0 data appear to be placed along ellipses whose ellipticity grows with time.
In Fig. 5.9 are also reported elliptic fits (blue solid curves). For the theory of elliptic fit I refers to appendix *A*. Our fit function is

$$c_{xx}x^2 + c_{yy}y^2 + c_{xy}xy + c_{xx} + c_{yy} - 1 = 0 \tag{5.8}$$

where x and y here stand for different z_i. Note, to be physically significant fit curves need to be entirely within the bounds $z_i \in$[-1 1] for both axis. The relation between the parameters in Eq. 5.8 and $\Delta\phi_{i,j}$ (where i$\neq$j, i,j=1,2,3) is

$$\Delta\phi_{i,j} = \mathrm{acos}\left(-\frac{c_{xy}}{2\sqrt{c_{xx}c_{yy}}}\right) \tag{5.9}$$

where x=z_i and y=z_j. From fit in Fig. 5.9 I derive $\Delta\phi_{1,2}$ and $\Delta\phi_{3,2}$ which are shown as a function of interrogation time T in Fig. 5.10.
$\Delta\phi_{1,2}$ and $\Delta\phi_{3,2}$ seems to grow both linearly with time T, as expected, and with the same velocity, so it means that the unknown ΔE_i are such that $|\Delta E_1 - \Delta E_2| \approx |\Delta E_3 - \Delta E_2|$. We can try to make some consideration to understand the origin of those unknown (and unwanted) ΔE_i.
A linear gradient F·x, where F is a constant Force and x is the position coordinate along double well array, would create an equal energy imbalance $\Delta E = Fd$ between the left and right mode of each double well, where d is their spatial separation. So, $\Delta\phi_{i,j}$ would be zero, and this it's not consistent with what we see.
Instead, let's assume the presence of a harmonic potential $V = \frac{1}{2}m_a\omega^2x^2$ We suppose our central double well centred respect to V ($\Delta E_2 = 0$). The energy mismatch of left and right modes (separated by distance d/2) of the double well at distance d from the bottom of V is $\Delta E_1 = \frac{1}{2}m_a\omega^2d^2$ (for us d=d$_-$ $= 10\mu$m). In the same way, the energy mismatch for the double well placed at distance -d will be $\Delta E_3 = -\frac{1}{2}m_a\omega^2d^2$.
Then, $\Delta\phi_{1,2} = \frac{1}{2}m_a\omega^2d^2T/\hbar$ and $\Delta\phi_{3,2} = -\frac{1}{2}m_a\omega^2d^2T/\hbar$, which show the linear dependence by T we observed in Fig. 5.10. Note, we can not retrieve information about the sign of the phase with our analysis, since we derive it from the ellipticity, which is a positive quantity. We can anyway obtain information about ω by a linear model fit of data in Fig. 5.10.
In future experiments I plan to apply a known and controllable harmonic potential on my

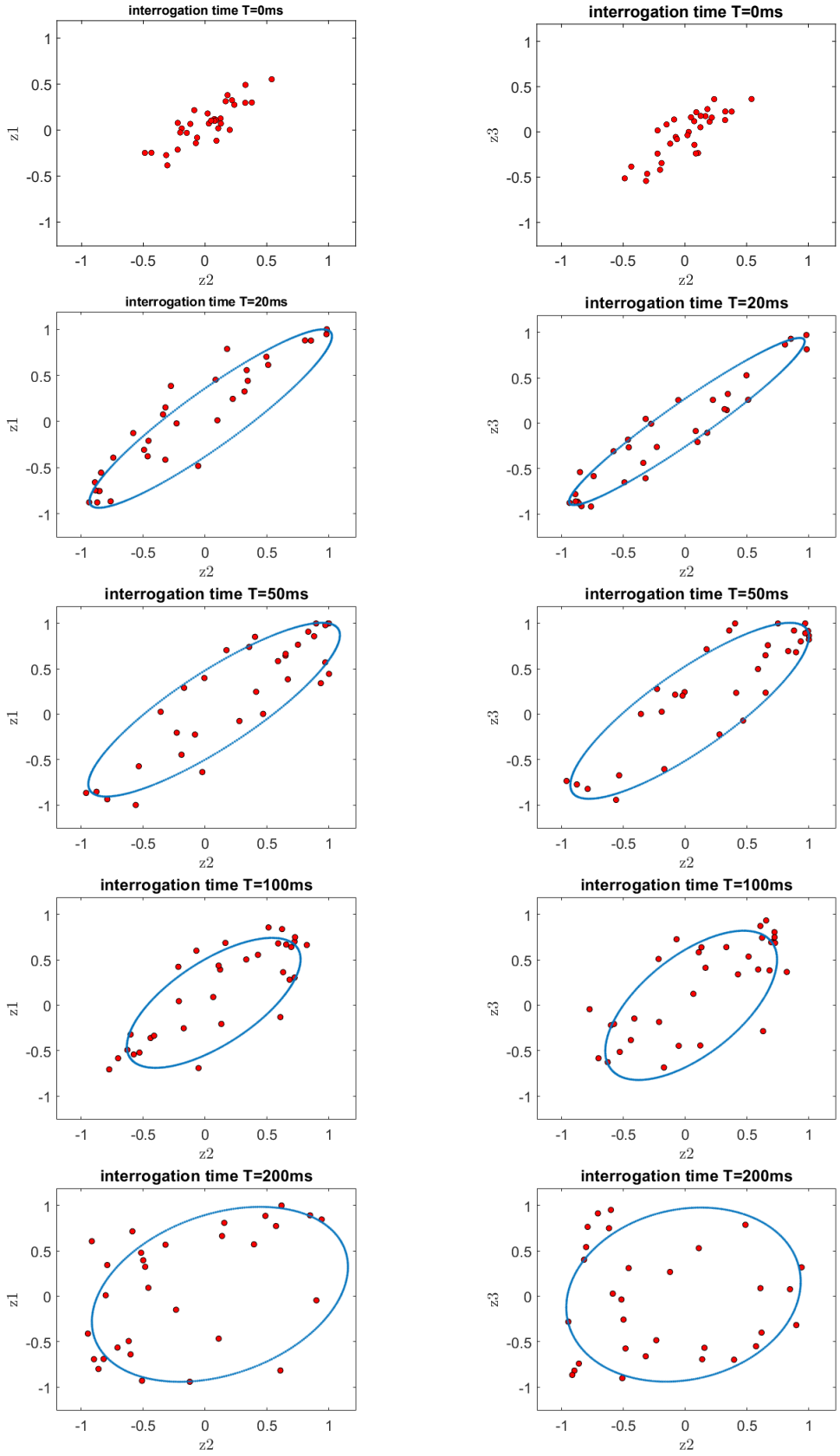

Figure 5.9: On the left, z_1 vs z_2 (red dots) for different interrogation time T=0,20,50,100,200 ms. On the right same plot for z_3 vs z_2. Blue solid line elliptic fit on such data.

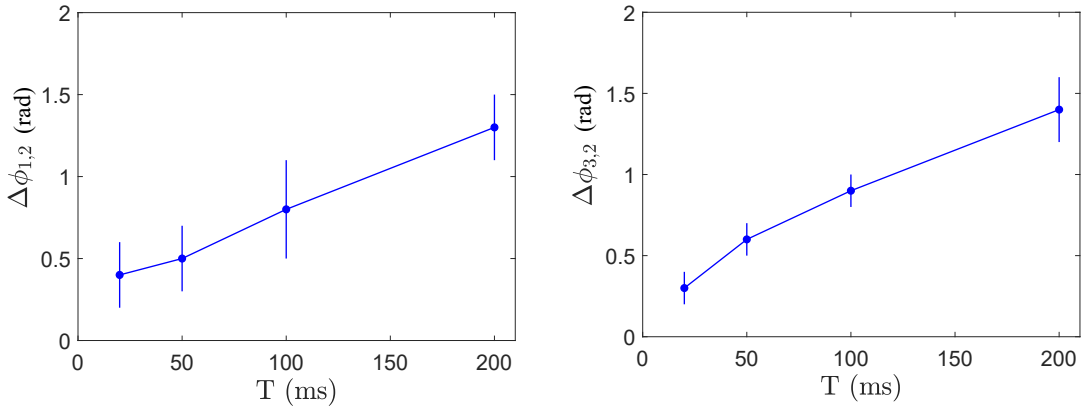

Figure 5.10: $\Delta\phi_{1,2}$ and $\Delta\phi_{3,2}$ obtained from fit of data in Fig. 5.9

system in order to change the phases $\Delta\phi_{1,2}$ and $\Delta\phi_{3,2}$, and so the ellipticity of my ellipses. If I manage to demonstrate such control, I will prove to have an operative trapped atom gradiometer.

5.4 Noise reduction by atom interactions

A second set of experiments performed with our array of double well potential concerns the possibility to introduce repulsive interaction to reduce fluctuations of population imbalances due to external noise, as mention in par.1.2 where it was shown that the variance of the atom number difference of the modes is $\frac{1}{2}\sqrt{\frac{\mathrm{E_J}}{\mathrm{E}_c+4\mathrm{E_J}/\mathrm{N}^2}}$.
With the same initial condition of the first beam splitter step, we now try to split a positive interacting BEC raising up the barrier with a slow ramp (200 ms). In Fig. 5.11 are reported imbalance fluctuations from experiment to experiment in presence of different values of two body scattering length $\mathrm{a}_s = 0, 0.35, 1.5, 3, 4.5\mathrm{a}_0$, where a_0 is the Bohr radius.
Unlike the case with no interaction we observe a clear reduction of imbalance fluctuation for increasing values of the scattering length. Intuitively, with reference to par.1.2, the response of the system to an energy mismatch of the two separated modes is to adapt the relative atomic population such that the chemical potential in the two modes is equal [97]. So even in presence of δ the configuration with large imbalances would be less favourable.

In Fig. 5.12 the standard deviation of imbalance fluctuation reported in Fig. 5.11 as function of scattering length a_s is shown. As one can see, σ_z decreases as interaction increase, as expected. Dashed black line represent the shot noise limit for an average atom number $\sim$4*10^3 in each double well. We are currently doing dynamical numerical simulations with the Bose-Hubbard to understand how far we are from the shot noise.
However, a first question is if the 200 ms ramp we use to raise up the barrier is slow enough to be adiabatic. Keeping this raising time τ fixed means that the energy scale of the system, defined by the plasma frequency ω_p in Eq. 1.38 in the interacting case, is set. We are adiabatic if

$$\tau > 1/\omega_p = 1 \Big/ \sqrt{\mathrm{E_J}\left(\mathrm{E}_c + \frac{4\mathrm{E}_J}{\mathrm{N}^2}\right)} \tag{5.10}$$

If τ is fixed and ω_p reduces with the tunnelling term E_j while raising up the barrier, then I need higher interaction term E_c to meet the condition in 5.9 (or I have to take larger time τ). Once the adiabaticity is broken, the state of the system remains in the state characterized by the value of E_j, reached at the moment of the adiabaticity breaking, and the variance of

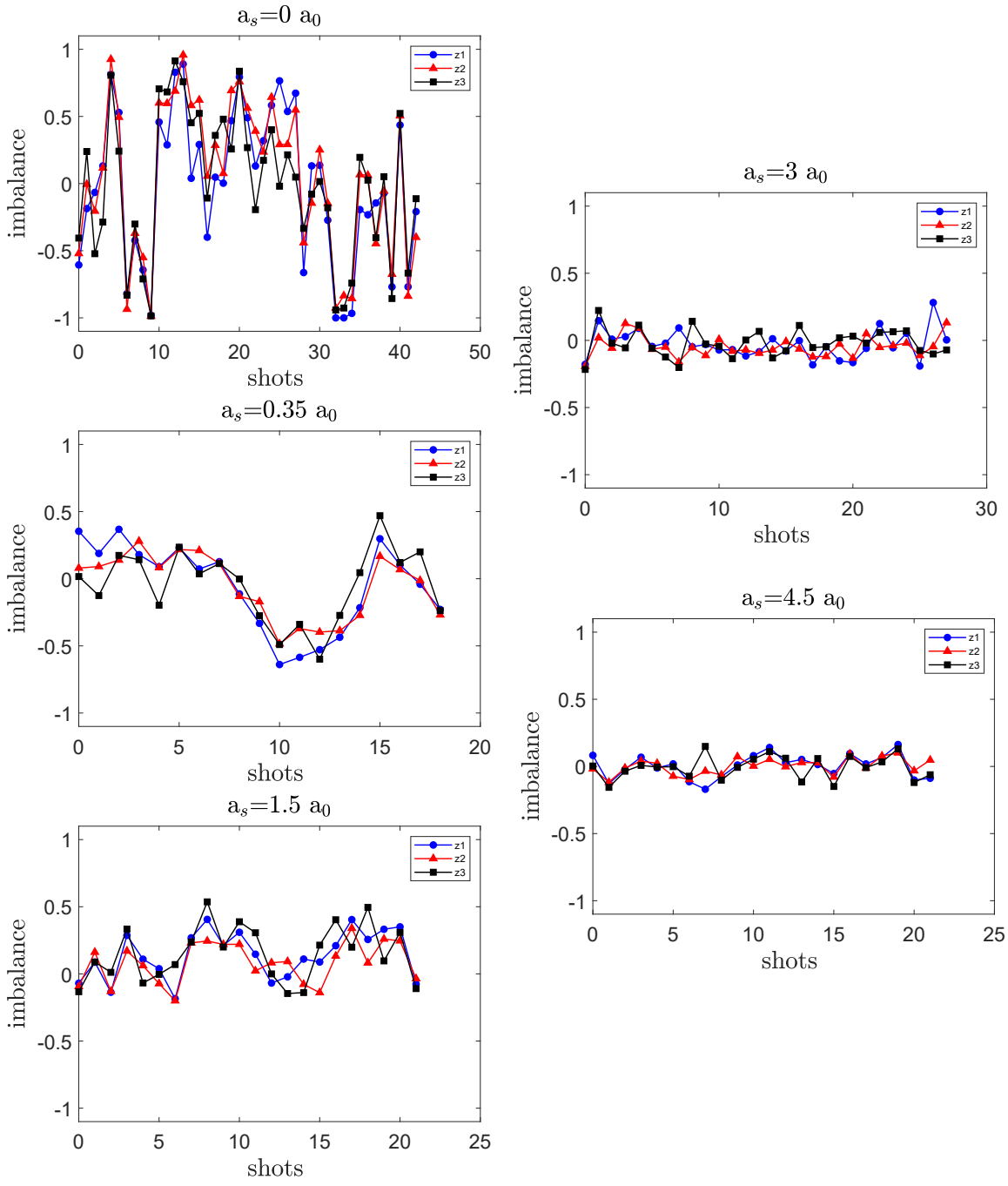

Figure 5.11: Plots show how the imbalance fluctuations z_i reduce for increasing values the scattering length of the condensate, setted before raising up the barrier in 200 ms to separate it.

atom number difference can't reach the shot noise unless increasing E_c.

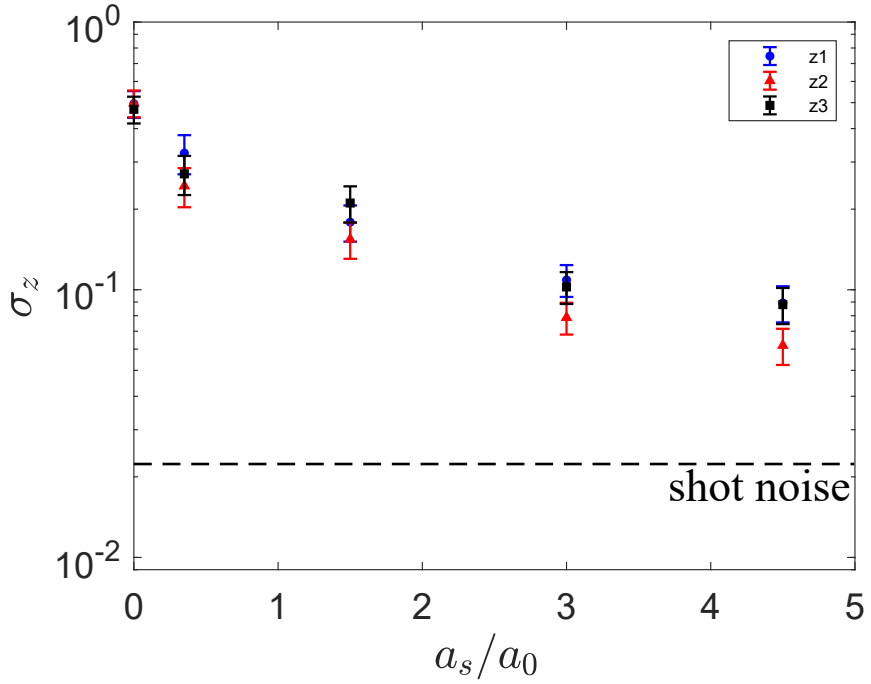

Figure 5.12: standard deviation of imbalance fluctuation reported in Fig. 5.11 as function of scattering length a_s. Dashed black line represent the shot noise limit for an average atom number $\sim 4*10^3$ in each double well

Chapter 6

Conclusions and Perspective

In conclusion, the core of this thesis is the realization of a novel superlattice based on the beat-note between two retroreflected laser beams with commensurate wavelengths, which I study both numerically and analytically.
I characterize the spectrum of such lattice exploiting the oscillation of the center of mass of a non interacting BEC loaded in a single effective site of the BNSL, showing that measurements match numerical predictions. I observed a non monotonic behaviour in the spectrum, which allow us to identify two regions: a range of depths for which the resulting potential is equivalent to a large-spacing single-wavelength optical lattice (small depth regime); outside that, BNSLs can't be described by an effective large spacing lattice, but can be potentially used to create arrays of atomic ensembles with negligible tunnelling between the sites. The passage between these two regimes occurs when the tunnelling between the sites of the two starting lattices become comparable with the energy gap of the effective lattice, then the wavefunction starts to localize inside the wells of the two starting lattices.
I implemented a 10μm BNSL in a horizontal Bloch oscillation interferometer, where I start with a non interacting BEC loaded in a single site of the effective potential. In presence of small external forces and finite tunnelling we manage to observe a coherent oscillation in the size of the condensate, i.e. in the population transferred in the neighbouring sites 10μm far from the starting one. The observed dynamics exhibits a coherence up to 1 s, which to my knowledge is one of the longest coherent evolutions ever reported for a BEC trapped in spatial modes separated by tens of microns. This proves the intrinsic stability of the BNSL, that make it a valuable tool for the precise manipulation of atoms at large distances, which is of interest for quantum simulation experiments and for improving sensitivity of trapped atom interferometers.
In a second experiment I exploit a 5μm BNSL to performed a proof-of-principle demonstration of a horizontal multimode interferometer in a harmonic trap based on Kapitza-Dirac diffraction pulses. Here, the harmonic potential has the function to close the trajectories and prevents the spatial spread of wavepackets. Importantly, all the momentum components generated by diffraction spatially recombine at the trap minimum only if the potential is harmonic over their oscillation amplitude. Here the purpose of using BNSL is take advantage of a large-spacing optical lattice, that reduces the recoil velocity, hence the oscillation amplitude, by a factor of 10, with respect to the commonplace lattice spacing of 0.5 μm. In this way we make sure we stay in the harmonic region of our optical trap. Anyway, even if in our system we reach a sensitivity a factor 40 away from the Cramér-Rao bound, mainly due to the instabilities of optical trap, in this scheme it is potentially easy to enhance the sensitivity by enlarging the spatial separation between the modes involved. Indeed, this can be done by reducing the harmonic trapping frequency, and increasing the number of momentum components with KD pulses of enhanced intensity and/or duration (of course provide that we still stay in a harmonic region of the trapping potential).

In the experiment I'm currently working on I realize a horizontal arrays of double wells potentials with two collinear BNSLs with a periodicity of one twice the other (10μm and 5μm), and to do this I need only three commensurate wavelengths. Changing the frequency of one of the three lasers I can match the relative phase condition I need between the three starting lattices to center the barrier. In my system I can count the in-situ atom number difference (z_i) between the two spatial modes of i-th double well, which tells me about the presence of an eventual energy difference between them. I studied and observed the effects on the array of non perfectly commensurate wavelengths, which introduce on the system confining/anti confining harmonic potentials, making eventually the z_i of the three double wells different one from the others. Luckily, this is something I can fix changing the frequency of one of the three lasers, and I can exploit it also to correct the presence of an external residual harmonic potential on the system.
Another control parameter is the depth of one of the three lattices, which allow us to set the height of the barrier, and so the tunnelling between the left and right mode in each double well.
To get information about the tunnelling energy I can study Rabi oscillations occurring in the atom number difference of the two spatial modes of each double well. Observing the same Rabi frequency (in a range of 60 HZ to 4 Hz) in the three double wells, with a complete inversion of the population of the two modes, assures us that the three double wells are identical, and that we manage to cancel the two body interaction on a good level. So, on this basis, we can perform three beam splitters simultaneously.
Each one of this double well then represents a sensor I can exploit to make a Mach-Zehnder interferometer. A preliminary set of measurements, with no external perturbation applied during the interrogation time, shows correlations between the outputs of each Mach-Zehnder, even in presence of large noise. Having more than one correlated interferometers is possible to perform differential analysis between the outputs to subtract common noise, and so realize an operative trapped atom gradiometer. A first trial of this differential analysis seems to reveal that a residual curvature on our system is present.
In this direction, the next step will be to apply a controlled external harmonic potential to induce a known interferometric phases on each sensor, and so test the sensitivity of the gradiometer. A last series of measures performed with our array of double well potential concerns the possibility to introduce repulsive interactions during a beam splitter to reduce fluctuations of z_i. About this, we observed a reduction of the variance of such fluctuation changing the two body scattering length a_s in a range of few Bohr radius (0-4.5 a_0), splitting our condensate raising up the barrier in 200 ms. We don't reach the shot noise limit, so dynamical numerical simulation with the Bose-Hubbard Hamiltonian are currently under study to justify this behaviour. Having a more clear understanding of our system in presence of inter-atomic interactions will, as a long term goal, allow us to realize non-classical states (number squeezed state), to enhance the sensitivity of the sensor beyond the standard quantum limit.

Appendix A

Elliptic Fit theory

A.0.1 Least squares model fit

Lets consider N independent data x_i, each normally distributed with the same mean μ but different variances σ_i^2. Since μ is unknown, we can define the following weighted sum

$$\chi^2 = \sum_{i=1}^{N} \frac{(x_i - \bar{\mu})^2}{\sigma_i^2} \tag{A.1}$$

where $\bar{\mu}$ is the best estimator of x_T. Least squares method [98] has the purpose to find $\bar{\mu}$ which minimize χ^2. The least squares estimator is thus given by

$$\bar{\mu} = \left(\frac{\partial \chi^2}{\partial \mu}\right)_{\mu=\bar{\mu}} = -2\sum_{i=1}^{N} \frac{(x_i - \bar{\mu})}{\sigma_i^2} = 0 \quad \longrightarrow \quad \bar{\mu} = \frac{\sum_i \frac{x_i}{\sigma_i^2}}{\sum_i \frac{1}{\sigma_i^2}} \tag{A.2}$$

χ^2 in Eq.A.1 has N-1 degree of freedom. Thus, if we were to repeat the identical experiment many times, the values of χ^2 obtained would be distributed as a Chi-squares distribution of (N-1), assuming that the probability density function of x_i was correct. If this is the case, then we can proceed estimating the variance of $\bar{\mu}$:

$$\mathrm{V}[\bar{\mu}] = \sum \left(\frac{\partial \bar{\mu}}{\partial x_i}\right)^2 \mathrm{Var}[x_i] = \frac{1}{\sum_i \frac{1}{\sigma_i^2}} \tag{A.3}$$

Above we had a number of measurements of a fixed quantity. Now let us suppose that we have a number of measurements y_i of a quantity y which depends on some other quantity x (i.e., a function). For each x_i, y is measured to be y_i with expected error σ_i. Assume, for now, that the values x_i are known exactly, and that we have a model for predict y as function of x :

$$y(x) = \theta_1 h_1(x) + \theta_2 h_2(x) ... + \theta_j h_j(x) \tag{A.4}$$

This is the curve which we fit to the data. y(x) is linear in the parameters, θ_i, that are to be estimated, while the single-valued and distinguishable functions $h_j(x)$ are known.
We want to determine the values of the θ_j for which the model Eq.A.4 best fits the measurements. We assume that any deviation of a point y_i from this curve is due to measurement error (something we don't have control over).
Thus, due to the error, we assume that the actual measurements are described by

$$y_i = y(x_i) = \theta_1 h_1(x_i) + \theta_2 h_2(x_i) ... + \theta_j h_j(x_i) + \epsilon_i \tag{A.5}$$

where ϵ_i are the error which introduce a certain distance between the point y_i and the hypothesized curve (residuals), which has zero mean and variance σ_i^2. Further, we assume for simplicity that each y_i is an independent measurement.
The problem now is to determinate the best value of parameters θ_j from N measurements (x_i,y_i). The meaning of least squares above is just that of minimizes the sum of the distances of data points from its expected values, here defined by ϵ_i, to obtain the estimate of θ_i. Therefore the χ^2 [1] to minimize will be

$$\chi^2 = \sum_{i=1}^{\mathrm{N}} \frac{\epsilon_i^2}{\sigma_i^2} = \sum_{i=1}^{\mathrm{N}} \frac{1}{\sigma_i^2} \left(y_i - \sum_j \theta_j h_j(x_i) \right)^2 \tag{A.6}$$

Imposing $\frac{\partial \chi^2}{\partial \theta_j} = 0$ we get a set of k (where k is the range of index j) linear equations in k unknowns, which is a problem way easier to solve in matrix form.
Lets call $\underline{y} = \mathrm{H}\underline{\theta} + \underline{\epsilon}$, where $\underline{y}$ and $\underline{\epsilon}$ are respectively the vectors of the N measurements y_i and N residuals ϵ_j, $\underline{\theta}$ the vector of k unknowns parameters and H a (N×k) matrix with elements $\mathrm{H}_{i,j} = h_{j=1\ldots\mathrm{k}}(x_{i=1\ldots\mathrm{N}})$. The errors σ_i^2 can also be incorporated in a N×N matrix, $\underline{\mathrm{V}}[\underline{y}]$ which is diagonal given our assumption of independent measurements with elements $\underline{\mathrm{V}}[\underline{y}]_{i,i} = \sigma_i^2$. Then the χ^2 becomes

$$\chi^2 = \left(\underline{y} - \mathrm{H}\underline{\theta}\right)^T \underline{\mathrm{V}}[\underline{y}] \left(\underline{y} - \mathrm{H}\underline{\theta}\right) \tag{A.7}$$

With this notations, the solution $\underline{\theta}$ which solve the system $\frac{\partial \chi^2}{\partial \theta_j} = 0$ is [98]

$$\underline{\hat{\theta}} = \left(\mathrm{H}^T \underline{\mathrm{V}}^{-1}[\underline{y}]\mathrm{H}\right)^{-1} \mathrm{H}^T \underline{\mathrm{V}}^{-1}[\underline{y}]\underline{y} \tag{A.8}$$

where the apex "T" means the transposed matrix.
It can be shown also that the covariance matrix of the estimators is given by

$$\underline{V}[\underline{\hat{\theta}}] = \mathrm{H}^T \underline{\mathrm{V}}[\underline{y}]\mathrm{H}. \tag{A.9}$$

If the covariance matrix $\underline{\mathrm{V}}[\underline{y}]$ is only known up to an overall constant, $\underline{\mathrm{V}}[\underline{y}] = \sigma^2\mathrm{W}$, with σ^2 unknown, then this latter can be estimated as [98]

$$\sigma^2 = \frac{\mathrm{Q}_{min}^2}{\mathrm{N} - \mathrm{k}} \tag{A.10}$$

where Q_{min} is the minimum value of χ^2 in Eq.A.7 in terms of W and with $\theta = \hat{\theta}$ and where N-k are the degree of freedom of χ^2.

A.0.2 Elliptic Fit

An ellipse is a multi-valued function which can be written in the form

$$\mathrm{F}(\vec{x}, \vec{c}) = c_{xx}x^2 + c_{yy}y^2 + c_{xy}xy + c_x x + c_y y - 1 \tag{A.11}$$

where we call $\vec{c} = (c_{xx}, c_{yy}, c_{xy}, c_x, c_y)$ the vector of the ellipse parameters, and
$\vec{x} = (x^2, y^2, xy, x, y)^T$ the vector of our observables. Before using this function to fit our data, we have to face the problem that this model is not linear in the parameters as Eq.A.4. So,

[1] this is a real χ^2, distributed with a chi-squares p.d.f, if the ϵ_i are normally distributed, but this is not mandatory

in order to apply the least squares method, I need first to define the distance between the points and our model (i.e. the residuals).
If I knew the vector of best parameters $\vec{\hat{c}}$ then the best choice would be the Euclidean distance, i.e. the perpendicular segment which connects a point to the ellipse. If this is not the case, then I'm valuing the residuals from a wrong ellipse. To find the right one, I should evaluate every residuals of every possible ellipse to find the one with the minimum distance.
A more suitable option is estimate the better parameters indirectly. This technique is called Parametric Least Squares (or adjustment of indirect observations [99]), which is a special case of the "Combined Least Squares" correction model [100].
Following [101], the idea is take $\vec{\hat{c}} = \vec{c} + \vec{\delta c}$ as the best estimators of parameters , such that $\mathrm{F}(\vec{\hat{x}}, \vec{\hat{c}})$=0 (here $\vec{\hat{x}}$ are the k points which I exploit to build the ellipse described by parameters $\vec{\hat{c}}$).
One can see $\vec{\delta c}$ as the vector of correction, which gives the distance between the vector of our initial parameter $\vec{c}$ and $\vec{\hat{c}}$. In the same way we can define $\vec{\hat{x}} = \vec{x} - \vec{r}$, where $\vec{r}$ is a vector of residuals.
Again, since we don't know the covariance matrix of $\vec{x}$ and $\vec{c}$ we can replace them with $\mathrm{V}_x = \sigma_x^2 \mathrm{W}_x$ and $\mathrm{V}_c = \sigma_c^2 \mathrm{W}_c$, where σ_x^2 and σ_c^2 are unknown. We then approximate each one of the k observation equations $\mathrm{F}(\vec{\hat{x}}, \vec{\hat{c}})$=0 around $\vec{x}$ and $\vec{c}$ with Taylor expansion, neglecting second order terms, obtaining

$$-\mathrm{F}(\vec{x}, \vec{c}) = \left(\frac{d\mathrm{F}}{d\vec{\hat{x}}}\right)_{\vec{x},\vec{c}} (\vec{\hat{x}} - \vec{x}) + \left(\frac{d\mathrm{F}}{d\vec{\hat{c}}}\right)_{\vec{x},\vec{c}} (\vec{\hat{c}} - \vec{c}) \quad \rightarrow \quad \mathbf{w} = \mathbf{B}\vec{r} + \mathbf{A}\vec{\delta c} \tag{A.12}$$

where:
A is a k×5 matrix whose i-th row corresponds to i-th set $\vec{x}_i = (x^2, y^2, xy, x, y)$
B is a k×n matrix, with n=2k, whose elements are in the form $\frac{\partial \mathrm{F}_i}{x_j}, \frac{\partial \mathrm{F}_i}{\partial y_j}$ with i,j=1...k.
The partial derivates reads:
$\frac{\partial \mathrm{F}_i}{\partial x_j} = \frac{\partial \mathrm{F}_i}{\partial y_j} = 0$ if i≠j, $\frac{\partial \mathrm{F}_i}{\partial x_i} = 2c_{xx}x_i + c_{xy}y_i + c_x$, $\frac{\partial \mathrm{F}_i}{\partial y_i} = 2c_{yy}y_i + c_{xy}x_i + c_y$.
w is a k×1 vector with elements $\mathrm{w}_i = -\mathrm{F}(\vec{x}_i, \vec{c}_i)$.
After many passages ([99]), one can find the least squares solution of Eq.A.12, i.e., the solution which makes the sums of the squares of the weighted residuals a minimum.

$$\begin{aligned} \vec{\delta c} &= \left(\mathbf{A}^T \left(\mathbf{B}\mathrm{W}_x^{-1}\mathbf{B}^T\right)\mathbf{A}\right)^{-1} \mathbf{A}^T \left(\mathbf{B}\mathrm{W}_x^{-1}\mathbf{B}^T\right)\mathbf{w} \\ \vec{r} &= \mathrm{W}_x^{-1}\mathbf{B}^T \left(\mathbf{B}W_x^{-1}\mathbf{B}^T\right)^{-1} (\mathbf{w} - \mathbf{A}\vec{\delta c}) \end{aligned} \tag{A.13}$$

So, in the beginning we said that the best parameters was $\vec{\hat{c}} = \vec{c} + \vec{\delta c}$. Imagine, at the beginning of the iterative process we want to build, that $\vec{\hat{c}}$ equals the a priori estimates $\vec{c}_1$ and a set of corrections $\vec{\delta c}_1$ is computed thanks to the method reported above. These then are added to $\vec{c}_1$ to give an updated set $\vec{c}_2$. **A** and **B** are recalculated and a new weight matrix W_x. The corrections are computed again, and the whole process cycles through until the corrections reach some predetermined value, which terminates the process.
In the end, we can estimate $\sigma_x^2 = \sigma_0^2 = \frac{\vec{r}^T \mathrm{W}^{-1} \vec{r}}{\mathrm{n-k}}$, where n-k are the degree off freedom. With σ_x^2 I can build the covariance matrix V_x and then the covariance matrix of the parameters as in Eq.A.9

$$\mathrm{V}_c = \sigma_0^2 \left[\mathbf{A}^T \left(\mathbf{B}W_x^{-1}\mathbf{B}^T\right) A\right]^{-1} \tag{A.14}$$

Note, changing the representation of the ellipse, for example choosing a different set of parameters as $\vec{s} = (t_x t_y a_x a_y \theta)^T$, doesn't change the results above, it simply requires a transformation of V_c to get the covariance matrix of parameters $\vec{s}$. In particular, $\mathrm{V}_s = J\mathrm{V}_c J^T$, where J is the Jacobian matrix of transformation, which only need to know how $\vec{s}$ depends on $\vec{s}$. This is useful if, for instance, one needs information about the centre of the ellipse (t_x, t_y), about the semi-axis a_x, a_y or its inclination θ.

Bibliography

[1] B Canuel, F Leduc, D Holleville, Alexandre Gauguet, J Fils, A Virdis, A Clairon, N Dimarcq, Ch J Bordé, A Landragin, et al. Six-axis inertial sensor using cold-atom interferometry. *Physical review letters*, 97(1):010402, 2006.

[2] Achim Peters, Keng Yeow Chung, and Steven Chu. Measurement of gravitational acceleration by dropping atoms. *Nature*, 400(6747):849–852, 1999.

[3] G Rosi, F Sorrentino, L Cacciapuoti, M Prevedelli, and GM Tino. Precision measurement of the newtonian gravitational constant using cold atoms. *Nature*, 510(7506):518–521, 2014.

[4] Richard H Parker, Chenghui Yu, Weicheng Zhong, Brian Estey, and Holger Müller. Measurement of the fine-structure constant as a test of the standard model. *Science*, 360(6385):191–195, 2018.

[5] Peter Asenbaum, Chris Overstreet, Minjeong Kim, Joseph Curti, and Mark A Kasevich. Atom-interferometric test of the equivalence principle at the 10- 12 level. *Physical Review Letters*, 125(19):191101, 2020.

[6] DN Aguilera, Holger Ahlers, Baptiste Battelier, Ahmad Bawamia, Andrea Bertoldi, R Bondarescu, Kai Bongs, Philippe Bouyer, Claus Braxmaier, Luigi Cacciapuoti, et al. Ste-quest—test of the universality of free fall using cold atom interferometry. *Classical and Quantum Gravity*, 31(11):115010, 2014.

[7] Naceur Gaaloul, H Ahlers, TA Schulze, Y Singh, ST Seidel, W Herr, W Ertmer, E Rasel, et al. Quantum tests of the equivalence principle with atom interferometry. *Acta Astronautica*, 67(9-10):1059–1062, 2010.

[8] Chris Overstreet, Peter Asenbaum, Tim Kovachy, Remy Notermans, Jason M Hogan, and Mark A Kasevich. Effective inertial frame in an atom interferometric test of the equivalence principle. *Physical review letters*, 120(18):183604, 2018.

[9] Jonas Hartwig, Sven Abend, Christian Schubert, Dennis Schlippert, Holger Ahlers, Katerine Posso-Trujillo, Naceur Gaaloul, Wolfgang Ertmer, and Ernst Maria Rasel. Testing the universality of free fall with rubidium and ytterbium in a very large baseline atom interferometer. *New Journal of Physics*, 17(3):035011, 2015.

[10] B Canuel, A Bertoldi, L Amand, E Pozzo di Borgo, T Chantrait, C Danquigny, Miguel Dovale Álvarez, B Fang, Andreas Freise, R Geiger, et al. Exploring gravity with the miga large scale atom interferometer. *Scientific Reports*, 8(1):1–23, 2018.

[11] Guglielmo M Tino, Fiodor Sorrentino, Deborah Aguilera, Baptiste Battelier, Andrea Bertoldi, Quentin Bodart, K Bongs, Philippe Bouyer, Claus Braxmaier, L Cacciapuoti, et al. Precision gravity tests with atom interferometry in space. *Nuclear Physics B-Proceedings Supplements*, 243:203–217, 2013.

[12] T Mazzoni, X Zhang, R Del Aguila, L Salvi, N Poli, and GM Tino. Large-momentum-transfer bragg interferometer with strontium atoms. *Physical Review A*, 92(5):053619, 2015.

[13] Holger Ahlers, Hauke Müntinga, Andre Wenzlawski, Markus Krutzik, Gunnar Tackmann, Sven Abend, Naceur Gaaloul, Enno Giese, Albert Roura, Rainer Kuhl, et al. Double bragg interferometry. *Physical review letters*, 116(17):173601, 2016.

[14] Tarik Berrada, Sandrine van Frank, Robert Bücker, Thorsten Schumm, J-F Schaff, and Jörg Schmiedmayer. Integrated mach–zehnder interferometer for bose–einstein condensates. *Nature communications*, 4(1):1–8, 2013.

[15] Mauro Antezza, Lev P Pitaevskii, Sandro Stringari, and Vitaly B Svetovoy. Casimir-lifshitz force out of thermal equilibrium and asymptotic nonadditivity. *Physical review letters*, 97(22):223203, 2006.

[16] Marco Fattori, B Deissler, C D'ERRICO, Mattia Jona-Lasinio, M Modugno, G Roati, L Santos, A Simoni, M Zaccanti, M Inguscio, et al. Atom interferometry with a weakly interacting bose-einstein condensate. In *Pushing The Frontiers Of Atomic Physics*, pages 251–262. World Scientific, 2009.

[17] G Spagnolli, G Semeghini, L Masi, G Ferioli, A Trenkwalder, S Coop, M Landini, L Pezzè, G Modugno, M Inguscio, et al. Crossing over from attractive to repulsive interactions in a tunneling bosonic josephson junction. *Physical review letters*, 118(23):230403, 2017.

[18] C Bodet, J Esteve, MK Oberthaler, and T Gasenzer. Two-mode bose gas: Beyond classical squeezing. *Physical Review A*, 81(6):063605, 2010.

[19] Sandrine van Frank, Antonio Negretti, Tarik Berrada, Robert Bücker, Simone Montangero, J-F Schaff, Thorsten Schumm, Tommaso Calarco, and Jörg Schmiedmayer. Interferometry with non-classical motional states of a bose–einstein condensate. *Nature communications*, 5(1):1–6, 2014.

[20] L Pezzé, LA Collins, A Smerzi, GP Berman, and AR Bishop. Sub-shot-noise phase sensitivity with a bose-einstein condensate mach-zehnder interferometer. *Physical Review A*, 72(4):043612, 2005.

[21] Luca Pezze, Augusto Smerzi, Markus K Oberthaler, Roman Schmied, and Philipp Treutlein. Quantum metrology with nonclassical states of atomic ensembles. *Reviews of Modern Physics*, 90(3):035005, 2018.

[22] Onur Hosten, Radha Krishnakumar, Nils J Engelsen, and Mark A Kasevich. Quantum phase magnification. *Science*, 352(6293):1552–1555, 2016.

[23] R Scheunemann, FS Cataliotti, TW Hänsch, and M Weitz. Resolving and addressing atoms in individual sites of a co 2-laser optical lattice. *Physical Review A*, 62(5):051801, 2000.

[24] Zoran Hadzibabic, Peter Krüger, Marc Cheneau, Baptiste Battelier, and Jean Dalibard. Berezinskii–kosterlitz–thouless crossover in a trapped atomic gas. *Nature*, 441(7097):1118–1121, 2006.

[25] L Masi, T Petrucciani, G Ferioli, G Semeghini, G Modugno, M Inguscio, and M Fattori. Spatial bloch oscillations of a quantum gas in a "beat-note" superlattice. *Physical Review Letters*, 127(2):020601, 2021.

[26] G Ferrari, N Poli, F Sorrentino, and GM Tino. Long-lived bloch oscillations with bosonic sr atoms and application to gravity measurement at the micrometer scale. *Physical Review Letters*, 97(6):060402, 2006.

[27] N Poli, F-Y Wang, MG Tarallo, A Alberti, M Prevedelli, and GM Tino. Precision measurement of gravity with cold atoms in an optical lattice and comparison with a classical gravimeter. *Physical review letters*, 106(3):038501, 2011.

[28] Leonardo Masi, Tommaso Petrucciani, Alessia Burchianti, Chiara Fort, Massimo Inguscio, Lorenzo Marconi, Giovanni Modugno, Niccolò Preti, Dimitrios Trypogeorgos, Marco Fattori, et al. Multimode trapped interferometer with noninteracting bose-einstein condensates. *Physical Review Research*, 3(4):043188, 2021.

[29] WeiDong Li, Tianchen He, and Augusto Smerzi. Multimode kapitza-dirac interferometry with trapped cold atoms. *Physical Review Letters*, 113(2):023003, 2014.

[30] Rudolf Grimm, Matthias Weidemüller, and Yurii B Ovchinnikov. Optical dipole traps for neutral atoms. In *Advances in atomic, molecular, and optical physics*, volume 42, pages 95–170. Elsevier, 2000.

[31] Neil W Ashcroft and N David Mermin. Solid state physics (saunders college, philadelphia, 1976). *Appendix N*, 166:87, 2010.

[32] Oliver Morsch and Markus Oberthaler. Dynamics of bose-einstein condensates in optical lattices. *Reviews of modern physics*, 78(1):179, 2006.

[33] Maxime Ben Dahan, Ekkehard Peik, Jakob Reichel, Yvan Castin, and Christophe Salomon. Bloch oscillations of atoms in an optical potential. *Physical Review Letters*, 76(24):4508, 1996.

[34] Zachary A Geiger, Kurt M Fujiwara, Kevin Singh, Ruwan Senaratne, Shankari V Rajagopal, Mikhail Lipatov, Toshihiko Shimasaki, Rodislav Driben, Vladimir V Konotop, Torsten Meier, et al. Observation and uses of position-space bloch oscillations in an ultracold gas. *Physical review letters*, 120(21):213201, 2018.

[35] Timo Hartmann, F Keck, HJ Korsch, and S Mossmann. Dynamics of bloch oscillations. *New Journal of Physics*, 6(1):2, 2004.

[36] Clarence Zener. Non-adiabatic crossing of energy levels. *Proceedings of the Royal Society of London. Series A, Containing Papers of a Mathematical and Physical Character*, 137(833):696–702, 1932.

[37] Andrey R Kolovsky and Hans Jürgen Korsch. Bloch oscillations of cold atoms in optical lattices. *International Journal of Modern Physics B*, 18(09):1235–1260, 2004.

[38] J Zapata, AM Guzmán, MG Moore, and P Meystre. Gravity-induced wannier-stark ladder in an optical lattice. *Physical Review A*, 63(2):023607, 2001.

[39] Peter J Martin, Bruce G Oldaker, Andrew H Miklich, and David E Pritchard. Bragg scattering of atoms from a standing light wave. *Physical review letters*, 60(6):515, 1988.

[40] Bryce Gadway, Daniel Pertot, René Reimann, Martin G Cohen, and Dominik Schneble. Analysis of kapitza-dirac diffraction patterns beyond the raman-nath regime. *Optics express*, 17(21):19173–19180, 2009.

[41] Phillip L Gould, George A Ruff, and David E Pritchard. Diffraction of atoms by light: The near-resonant kapitza-dirac effect. *Physical review letters*, 56(8):827, 1986.

[42] JH Huckans, IB Spielman, B Laburthe Tolra, WD Phillips, and JV Porto. Quantum and classical dynamics of a bose-einstein condensate in a large-period optical lattice. *Physical Review A*, 80(4):043609, 2009.

[43] Subhadeep Gupta, Aaron E Leanhardt, Alexander D Cronin, and David E Pritchard. Coherent manipulation of atoms with standing light waves. *Comptes Rendus de l'Académie des Sciences-Series IV-Physics*, 2(3):479–495, 2001.

[44] CD Herold, VD Vaidya, Xiao Li, SL Rolston, JV Porto, and MS Safronova. Precision measurement of transition matrix elements via light shift cancellation. *Physical review letters*, 109(24):243003, 2012.

[45] Lu Deng, Edward W Hagley, J Denschlag, JE Simsarian, Mark Edwards, Charles W Clark, Kristian Helmerson, SL Rolston, and William D Phillips. Temporal, matter-wave-dispersion talbot effect. *Physical Review Letters*, 83(26):5407, 1999.

[46] Benjamin T Beswick, Ifan G Hughes, and Simon A Gardiner. Lattice-depth measurement using multipulse atom diffraction in and beyond the weakly diffracting limit. *Physical Review A*, 99(1):013614, 2019.

[47] Jean Dalibard. Collisional dynamics of ultra-cold atomic gases. In *Bose-Einstein Condensation in Atomic Gases*, pages 321–349. IOS Press, 1999.

[48] Cheng Chin, Rudolf Grimm, Paul Julienne, and Eite Tiesinga. Feshbach resonances in ultracold gases. *Reviews of Modern Physics*, 82(2):1225, 2010.

[49] Christopher J Pethick and Henrik Smith. *Bose–Einstein condensation in dilute gases*. Cambridge university press, 2008.

[50] Rudolf Gati. *Bose-Einstein condensates in a single double well potential*. PhD thesis, 2007.

[51] David Ananikian and Thomas Bergeman. Gross-pitaevskii equation for bose particles in a double-well potential: Two-mode models and beyond. *Physical Review A*, 73(1):013604, 2006.

[52] L Pitaevskii and S Stringari. Thermal vs quantum decoherence in double well trapped bose-einstein condensates. *Physical Review Letters*, 87(18):180402, 2001.

[53] Viktor Novičenko, Julius Ruseckas, and Egidijus Anisimovas. Quantum dynamics in potentials with fast spatial oscillations. *Physical Review A*, 99(4):043608, 2019.

[54] A Trenkwalder, G Spagnolli, G Semeghini, S Coop, M Landini, P Castilho, L Pezze, G Modugno, M Inguscio, A Smerzi, et al. Quantum phase transitions with parity-symmetry breaking and hysteresis. *Nature physics*, 12(9):826–829, 2016.

[55] Loïc Henriet, Lucas Beguin, Adrien Signoles, Thierry Lahaye, Antoine Browaeys, Georges-Olivier Reymond, and Christophe Jurczak. Quantum computing with neutral atoms. *Quantum*, 4:327, 2020.

[56] Harry Levine, Alexander Keesling, Giulia Semeghini, Ahmed Omran, Tout T Wang, Sepehr Ebadi, Hannes Bernien, Markus Greiner, Vladan Vuletić, Hannes Pichler, et al. Parallel implementation of high-fidelity multiqubit gates with neutral atoms. *Physical review letters*, 123(17):170503, 2019.

[57] William G Tobias, Kyle Matsuda, Jun-Ru Li, Calder Miller, Annette N Carroll, Thomas Bilitewski, Ana Maria Rey, and Jun Ye. Reactions between layer-resolved molecules mediated by dipolar spin exchange. *Science*, 375(6586):1299–1303, 2022.

[58] David J Griffiths and Darrell F Schroeter. *Introduction to quantum mechanics*. Cambridge university press, 2018.

[59] Manuele Landini. *A tunable Bose-Einstein condensate for quantum interferometry*. PhD thesis, University of Trento, 2012.

[60] Massimo Inguscio and Giacomo Colzi. Interferometria atomica con un condensato di bose-einstein in un potenziale a doppia buca.

[61] Manuele Landini, Sanjukta Roy, Giacomo Roati, Andrea Simoni, Massimo Inguscio, Giovanni Modugno, and Marco Fattori. Direct evaporative cooling of 39 k atoms to bose-einstein condensation. *Physical Review A*, 86(3):033421, 2012.

[62] Giacomo Roati, Matteo Zaccanti, C d'Errico, Jacopo Catani, Michele Modugno, Andrea Simoni, Massimo Inguscio, and G Modugno. K 39 bose-einstein condensate with tunable interactions. *Physical review letters*, 99(1):010403, 2007.

[63] Chiara d'Errico, Matteo Zaccanti, Marco Fattori, Giacomo Roati, Massimo Inguscio, Giovanni Modugno, and Andrea Simoni. Feshbach resonances in ultracold 39k. *New Journal of physics*, 9(7):223, 2007.

[64] Anthony E Siegman. *Lasers*. University science books, 1986.

[65] Eric D Black. An introduction to pound–drever–hall laser frequency stabilization. *American journal of physics*, 69(1):79–87, 2001.

[66] RWP Drever, John L Hall, FV Kowalski, J_ Hough, GM Ford, AJ Munley, and H Ward. Laser phase and frequency stabilization using an optical resonator. *Applied Physics B*, 31(2):97–105, 1983.

[67] Edward A Whittaker, Manfred Gehrtz, and Gary C Bjorklund. Residual amplitude modulation in laser electro-optic phase modulation. *JOSA B*, 2(8):1320–1326, 1985.

[68] Gianmaria Milani, Benjamin Rauf, Piero Barbieri, Filippo Bregolin, Marco Pizzocaro, Pierre Thoumany, Filippo Levi, and Davide Calonico. Multiple wavelength stabilization on a single optical cavity using the offset sideband locking technique. *Optics letters*, 42(10):1970–1973, 2017.

[69] James I Thorpe, K Numata, and J Livas. Laser frequency stabilization and control through offset sideband locking to optical cavities. *Optics express*, 16(20):15980–15990, 2008.

[70] S Blatt, A Mazurenko, MF Parsons, CS Chiu, F Huber, and M Greiner. Low-noise optical lattices for ultracold li 6. *Physical Review A*, 92(2):021402, 2015.

[71] Jayadev Vijayan, Pimonpan Sompet, Guillaume Salomon, Joannis Koepsell, Sarah Hirthe, Annabelle Bohrdt, Fabian Grusdt, Immanuel Bloch, and Christian Gross. Time-resolved observation of spin-charge deconfinement in fermionic hubbard chains. *Science*, 367(6474):186–189, 2020.

[72] Timon A Hilker, Guillaume Salomon, Fabian Grusdt, Ahmed Omran, Martin Boll, Eugene Demler, Immanuel Bloch, and Christian Gross. Revealing hidden antiferromagnetic correlations in doped hubbard chains via string correlators. *Science*, 357(6350):484–487, 2017.

[73] Guillaume Salomon, Joannis Koepsell, Jayadev Vijayan, Timon A Hilker, Jacopo Nespolo, Lode Pollet, Immanuel Bloch, and Christian Gross. Direct observation of incommensurate magnetism in hubbard chains. *Nature*, 565(7737):56–60, 2019.

[74] Philipp M Preiss, Ruichao Ma, M Eric Tai, Alexander Lukin, Matthew Rispoli, Philip Zupancic, Yoav Lahini, Rajibul Islam, and Markus Greiner. Strongly correlated quantum walks in optical lattices. *Science*, 347(6227):1229–1233, 2015.

[75] Andrea Trombettoni and Augusto Smerzi. Discrete solitons and breathers with dilute bose-einstein condensates. *Physical Review Letters*, 86(11):2353, 2001.

[76] I Nałęcz, L Masi, G Ferioli, T Petrucciani, M Fattori, and J Chwedeńczuk. Sensitivity bounds of a spatial bloch-oscillation atom interferometer. *Physical Review A*, 102(3):033318, 2020.

[77] Luca Pezzé and Augusto Smerzi. Entanglement, nonlinear dynamics, and the heisenberg limit. *Physical review letters*, 102(10):100401, 2009.

[78] Samuel L Braunstein and Carlton M Caves. Statistical distance and the geometry of quantum states. *Physical Review Letters*, 72(22):3439, 1994.

[79] Onur Hosten, Nils J Engelsen, Rajiv Krishnakumar, and Mark A Kasevich. Measurement noise 100 times lower than the quantum-projection limit using entangled atoms. *Nature*, 529(7587):505–508, 2016.

[80] Antoine Browaeys and Thierry Lahaye. Many-body physics with individually controlled rydberg atoms. *Nature Physics*, 16(2):132–142, 2020.

[81] Joannis Koepsell, Jayadev Vijayan, Pimonpan Sompet, Fabian Grusdt, Timon A Hilker, Eugene Demler, Guillaume Salomon, Immanuel Bloch, and Christian Gross. Imaging magnetic polarons in the doped fermi–hubbard model. *Nature*, 572(7769):358–362, 2019.

[82] Ying-Ju Wang, Dana Z Anderson, Victor M Bright, Eric A Cornell, Quentin Diot, Tetsuo Kishimoto, Mara Prentiss, RA Saravanan, Stephen R Segal, and Saijun Wu. Atom michelson interferometer on a chip using a bose-einstein condensate. *Physical review letters*, 94(9):090405, 2005.

[83] RE Sapiro, R Zhang, and G Raithel. Atom interferometry using kapitza-dirac scattering in a magnetic trap. *Physical Review A*, 79(4):043630, 2009.

[84] Alessia Burchianti, Chiara D'Errico, Lorenzo Marconi, Francesco Minardi, Chiara Fort, and Michele Modugno. Effect of interactions in the interference pattern of bose-einstein condensates. *Physical Review A*, 102(4):043314, 2020.

[85] Jason M Hogan, David Johnson, and Mark A Kasevich. Light-pulse atom interferometry. *arXiv preprint arXiv:0806.3261*, 2008.

[86] Pippa Storey and Claude Cohen-Tannoudji. The feynman path integral approach to atomic interferometry. a tutorial. *Journal de Physique II*, 4(11):1999–2027, 1994.

[87] Ruolei Cheng, Tianchen He, Weidong Li, Augusto Smerzi, et al. Theory of a kaptiza-dirac interferometer with cold trapped atoms. *Journal of Modern Physics*, 7(15):2043, 2016.

[88] T Bergeman, Gidon Erez, and Harold J Metcalf. Magnetostatic trapping fields for neutral atoms. *Physical Review A*, 35(4):1535, 1987.

[89] J Chwedeńczuk, F Piazza, and A Smerzi. Multipath interferometer with ultracold atoms trapped in an optical lattice. *Physical Review A*, 87(3):033607, 2013.

[90] Tian-Chen He, Peng-Bin Niu, and Ji Li. Measurement of gravitational acceleration by cold atom multimode interference in the anharmonic potential. *Annals of Physics*, 419:168227, 2020.

[91] GDME Roati, E De Mirandes, F Ferlaino, H Ott, G Modugno, and M Inguscio. Atom interferometry with trapped fermi gases. *Physical review letters*, 92(23):230402, 2004.

[92] Y Shin, Michele Saba, TA Pasquini, W Ketterle, DE Pritchard, and AE Leanhardt. Atom interferometry with bose-einstein condensates in a double-well potential. *Physical review letters*, 92(5):050405, 2004.

[93] A Bertoldi, G Lamporesi, L Cacciapuoti, M De Angelis, M Fattori, T Petelski, A Peters, M Prevedelli, J Stuhler, and GM Tino. Atom interferometry gravity-gradiometer for the determination of the newtonian gravitational constant g. *The European Physical Journal D-Atomic, Molecular, Optical and Plasma Physics*, 40(2):271–279, 2006.

[94] G Rosi, G D'Amico, L Cacciapuoti, F Sorrentino, M Prevedelli, M Zych, Č Brukner, and GM Tino. Quantum test of the equivalence principle for atoms in coherent superposition of internal energy states. *Nature communications*, 8(1):1–6, 2017.

[95] Juan Ignacio Cirac, M Lewenstein, Klaus Mølmer, and Peter Zoller. Quantum superposition states of bose-einstein condensates. *Physical Review A*, 57(2):1208, 1998.

[96] K Eckert, P Hyllus, D Bruß, UV Poulsen, M Lewenstein, C Jentsch, T Müller, EM Rasel, and W Ertmer. Differential atom interferometry beyond the standard quantum limit. *Physical Review A*, 73(1):013814, 2006.

[97] Christian Gross. Spin squeezing, entanglement and quantum metrology with bose–einstein condensates. *Journal of Physics B: Atomic, Molecular and Optical Physics*, 45(10):103001, 2012.

[98] WJ Metzger. *Statistical methods in data analysis*. Fakulteit der Natuurwetenschappen, Katholieke Universiteit Nijmegen, 2000.

[99] Charles D Ghilani and RP Wolf. Adjustment computations: spatial data analysis. *New Jersey*, 2009.

[100] RE Deakin. Notes on least squares. *School of Mathematical and Geospatial Science. RMIT*, 2005.

[101] G Panou and A-M Agatza-Balodimou. Direct and indirect estimation of the variance–covariance matrix of the parameters of a fitted ellipse and a triaxial ellipsoid. *Journal of Surveying Engineering*, 147(1):04020026, 2021.